Innovative Polymers for Lithium-ion Batteries

Soline Vauthier

PhD Thesis 2023

Supervised by:

Dr. Nerea Casado (UPV/EHU)

Prof. David Mecerreyes (UPV/EHU)

Dr. Stéphane Cotte (Toyota Motor Europe)

eman ta zabal zazu

Universidad del País Vasco

Euskal Herriko Unibertsitatea

(cc)2023 SOLINE VAUTHIER (cc by-nc-nd 4.0)

Innovative Polymers for Lithium-ion Batteries

Soline Vauthier

PhD Thesis 2023

Supervised by:

Dr. Nerea Casado (UPV/EHU)

Prof. David Mecerreyes (UPV/EHU)

Dr. Stéphane Cotte (Toyota Motor Europe)

eman ta zabal zazu

Universidad del País Vasco

Euskal Herriko Unibertsitatea

POLYMAT

TOYOTA

POLYTE - EID

Innovative POLYmers for Lithium Battery TEchnologies

European Industrial Doctorate

Horizon 2020

Marie Skłodowska-Curie actions

Table of contents

Chapter 1. Introduction.....1

1.1. Context.....1

1.2. Electrochemical Energy Storage.....4

1.2.1. Battery history 4

1.2.2. Rechargeable battery technology 8

1.3. Polymers in batteries.....12

1.3.1. Polymer binders for cathodes 12

1.3.2. Solid polymer electrolytes 18

1.4. Motivation and objectives.....20

1.5. Outline of the thesis.....22

1.6. References.....24

Chapter 2. Pyrrolidinium-based poly(ionic liquid) binders with fluorinated and redox-active anions for Li-ion batteries 32

2.1. Introduction 32

2.2. Synthesis of functionalized PDADMA PILs.....36

2.2.1. Synthesis of fluorinated PDADMA PILs 36

2.2.2. Synthesis of redox-active PDADMA PILs 37

2.3. Physicochemical characterizations of PDADMA PILs 39

2.4. Electrochemical characterizations of redox-active PDADMA PILs.43

2.5. Application of PDADMA PILs as binder for high voltage NMC cathodes in Li-ion batteries 48

2.5.1. Electrode characterization and standardization protocols..... 49

2.5.2. Fluorinated PDADMA PILs 55

2.5.3. Redox-active PDADMA PILs 68

2.6. Conclusion 72

2.7. Experimental part.....74

2.7.1. Materials..... 74

2.7.2. Synthesis of fluorinated PDADMA-PILs 75

2.7.3. Synthesis of redox-active PDADMA PILs 78

2.7.4. Polymer characterizations 84

2.7.5. Electrochemical analysis of redox activity of PDADMA PILs 85

2.7.6. Preparation of the Li-ion batteries 86

2.7.7. Electrochemical characterizations in lithium-ion batteries 86

2.8. References.....90

Chapter 3. Single lithium-ion conducting polymers with high ionic conductivity based on borate pendant groups 98

3.1. Introduction 98

3.2. Polymer synthesis and characterizations 101

3.2.1. Synthesis of monomers and their polymerizations..... 101

3.2.2. Structure characterizations 104

3.2.3. Thermal analysis 109

3.3. Study of ionic conductivity.....110

3.3.1. Effect of the different pendant groups with one ethoxy unit: n_1 111

3.3.2. Effect of increasing the ethoxy unit (n_1, n_7, and n_9) 113

3.3.3. Effect of the different pendant groups with the ethoxy unit of n_7 115

3.3.4. Influence of the fluorine number 116

3.3.5. Other electrochemical characterizations for SLICPEs 118

3.4. Battery performances.....120

3.5. Conclusions 122

3.6. Experimental part.....123

3.6.1. Materials..... 123

3.6.2. Synthesis of the single lithium-ion monomers..... 123

3.6.3. Polymerization procedure 125

3.6.4. Polymer material characterizations 128

3.6.5. Preparation of SLICPEs..... 132

3.6.6. Electrochemical characterizations..... 133

3.7. References.....136

Chapter 4. Conclusion 142

Resumen.....145

List of acronyms 150

List of publications and patents, conference presentations, and collaborations 155

Acknowledgements

Firstly, I would like to thank my supervisors Dr. Nerea Casado, Prof. David Mecerreyes, and Dr. Stéphane Cotte for their support, advice, and discussions that have been able to advance this research project.

I thank the European Union's Horizon 2020 research and innovation program, which funded this European Industrial Doctorate (EID) project.

I would like to offer my special thanks to Laurent and Aurélie for all their help, and support during the thesis, also for their warm welcome at TME.

I thank my two colleagues from the POLYTE team, Marta and Marine, with whom I shared these years of thesis experience. I am deeply grateful to Marta, for all her help (scientific, administrative, Spanish, her bus card and others things…), for our discussions, for her support and good vibes.

I would like to thank all my colleagues at UPV/EHU, POLYMAT, as well as TME, and all the outsiders who participated directly or indirectly in my thesis, allowing me to progress. In particular, I thank Greg, Nico, Liliana, Rafa, and Jorge for their help in the laboratory with whom I liked working. I also thank Hannah, and Alexis, as well as the entire battery and fuel cell team at TME, and the colleagues with whom I shared discussions in the office or in the cafeteria.

Finally, I would like to extend my sincere thanks to my friends (Lucie, Marine, Mathieu, Juline, Eugénie, Justine, Camille, Pauline, Laurent, Eugénie and its Aloé Véra) and all my family (especially Diego, my parents, Amélie, and brothers, Anaïs, Mathilde, Martin, JB, and Camille); who have been indispensable support throughout this thesis.

Chapter 1. Introduction

1.1. Context

In our current society, the demand for energy is increasing every day, due to the ever-increasing world population. To cope with the energy demand, it was estimated that the rate of energy production, which was 130 000 TWh in 2010, will have to double by 2050 [1]. This increase must be achieved without increasing CO_2 emissions, by limiting fossil fuel resources and the environmental impact for reasons of global warming which threatens the planet and our future. Thus, the development of advanced renewable energy technologies is a global imperative.

In the European Union in 2019, 31% of final energy consumption was used for transport modes (**Figure 1.1a**). This makes transport one of the three dominant sectors requiring the most energy with industry and households. Among the energies used for the transport sector, about 72% relate to road transport (passenger and freight) (**Figure 1.1b**). Given the proportion of road transport in the global energy consumption for transport, proposing sustainable solutions to improve energy storage for land vehicles has a significant impact on CO_2 emissions on a global scale.

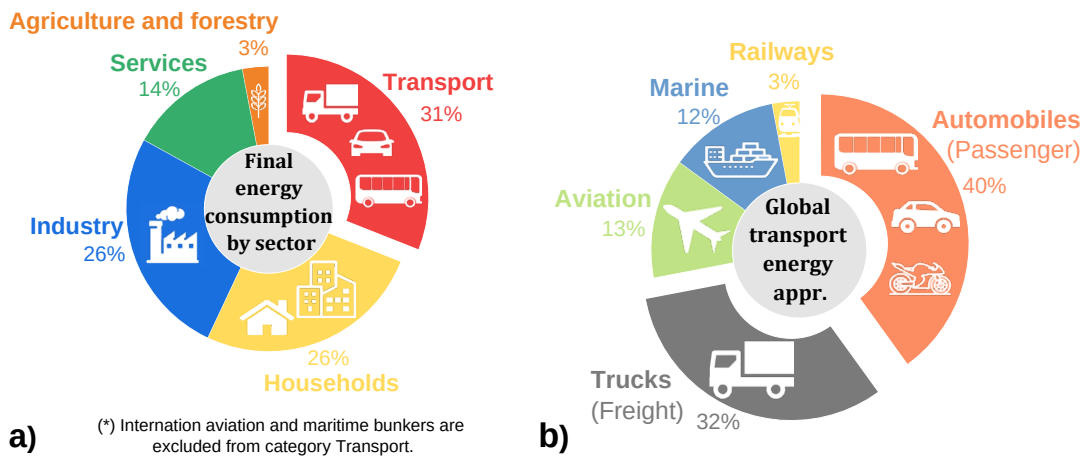

Figure 1.1. Energy consumption in European Union for 2019: a) Final energy consumption by sector (% of total, based in tons of oil equivalent); and b) Global energy consumption in the transport sector. *Sources*: Eurostat, European Environment Agency (EEA), International Energy Agency - World Energy Outlook (IEA-WEO)

Figure 1.2 shows the total CO_2 emissions ($g \cdot km^{-1}$) for internal combustion engine cars (on the left) and electric vehicles (EVs) (on the right) estimated by D. Larcher et al. [1] in with various electricity origins. The CO_2 emissions for the car production of internal combustion engine and EVs are the similar. According to the study, diesel and gasoline cars emit approximately 190 and 210 $g \cdot km^{-1}$ of CO_2 respectively, and mostly due to the fuel combustion. Regarding EVs, it is very important to note that the CO_2 benefit is highly dependent on the origin of the electricity. Indeed, the use of electricity produced 100% hydro estimates a CO_2 emission (of 60 $g \cdot km^{-1}$) approximately 70% less compared to cars with internal combustion engines, but conversely, the use of 100% coal-fired electricity would emit approximately 40% more of CO_2 (270 $g \cdot km^{-1}$). In general, with the electricity production program in Europe in 2012, it was estimated that EVs emitted on average 25% less CO_2 than thermal engine cars; and 60% less with the French electricity mix because 80% is from nuclear power.

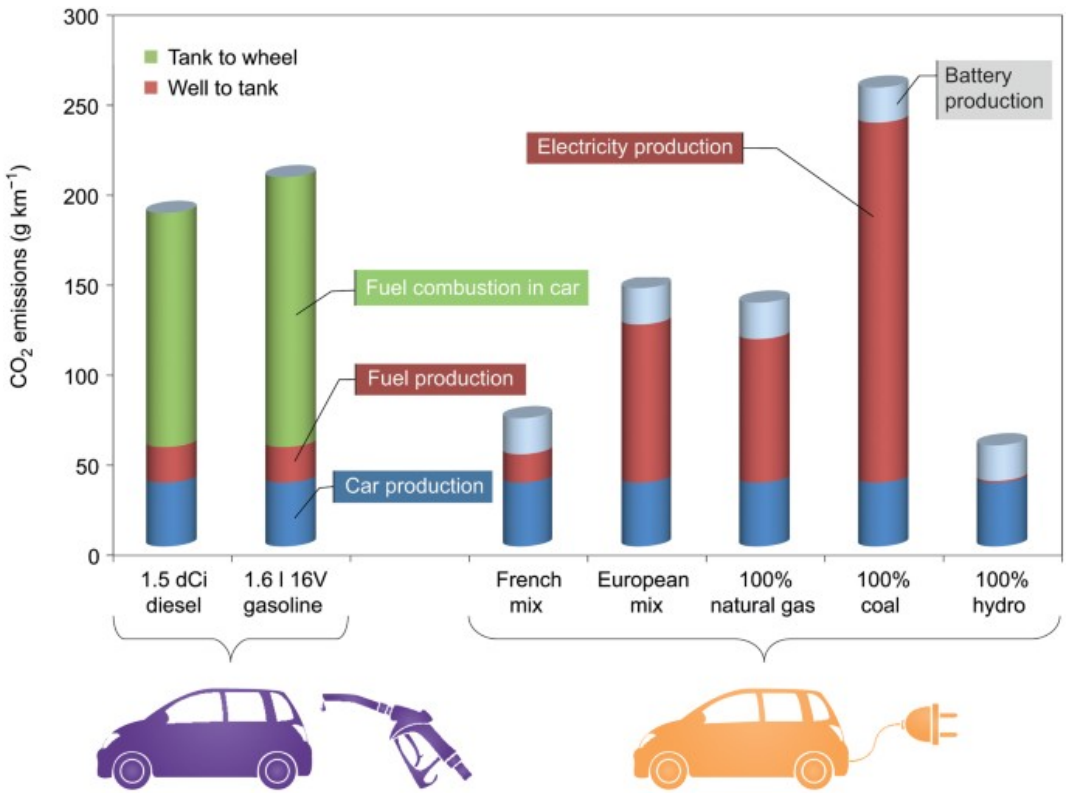

Figure 1.2. The CO_2 benefit of electric vehicles relies heavily on the origin of the electricity. Total CO_2 emissions (g.km^{-1}) for internal combustion engine cars (left) and for full electric vehicles (right) with various electricity origins. [1]

Fortunately, renewable energies are eventually developing to propose electrical energies with lower CO_2 emissions. The European Commission is committed to a desire in favor of the decarburization of transport and recently published a communication [2] to propose a low-emission mobility strategy by increasing the efficiency of the transport system, by deploying alternative energies with low emissions and moving towards low- and zero-emission vehicles [3]. In addition, in June 2022 the European Parliament voted in favor of banning, from 2035, the sale of new vehicles with combustion engines in Europe to promote the electrical cars. To complement efforts to seriously alter our energy patterns, it is essential to improve the electrical energy storage with electrochemical energy storage in batteries serving as key components of any plausible scenario [4,5].

1.2. Electrochemical Energy Storage

1.2.1. Battery history

The main goal of the battery industry is to obtain specific levels of battery performance for different applications (e.g. applied voltage and capacity) with low production costs. In this context, intensive research is being devoted to the development of rechargeable or secondary batteries. Hundreds of electrochemical couples were proposed during the nineteenth and early twentieth centuries, the most notable primary battery being zinc-manganese dioxide (Zn-MnO_2), lead-acid, and nickel-cadmium (Ni-Cd) being the most common [6]. **Figure 1.3** illustrates the evolution of batteries and shows their energy density. Increasing battery performance is associated with the use of novel materials and concepts leading to increasing loading capacity, cycle life, and safety. Unlike older battery technologies, the electrolyte in nickel-metal hydride (Ni-MH) and lithium-ion batteries are not consumed in the battery chemistry. One of the key elements of these two batteries is that the same ion (H^+ for Ni-MH and Li^+ for lithium-ion batteries) participates at both electrodes, being reversibly inserted and extracted from the electrode material, with the concomitant addition or removal of electrons [7].

The status of current commercial batteries and possible future chemistries are summarized in **Figure 1.4**, which depicts the energy performance characteristics of the major rechargeable battery types. There is large uncertainty in their respective position in the graph. The lead–acid battery is the first type of rechargeable battery with lead electrodes and sulfuric acid electrolytes invented in 1859 by French physicist Gaston Planté [8]. Compared to modern rechargeable batteries, lead–acid batteries have relatively low energy density. Despite this, their ability to supply high surge currents means that the

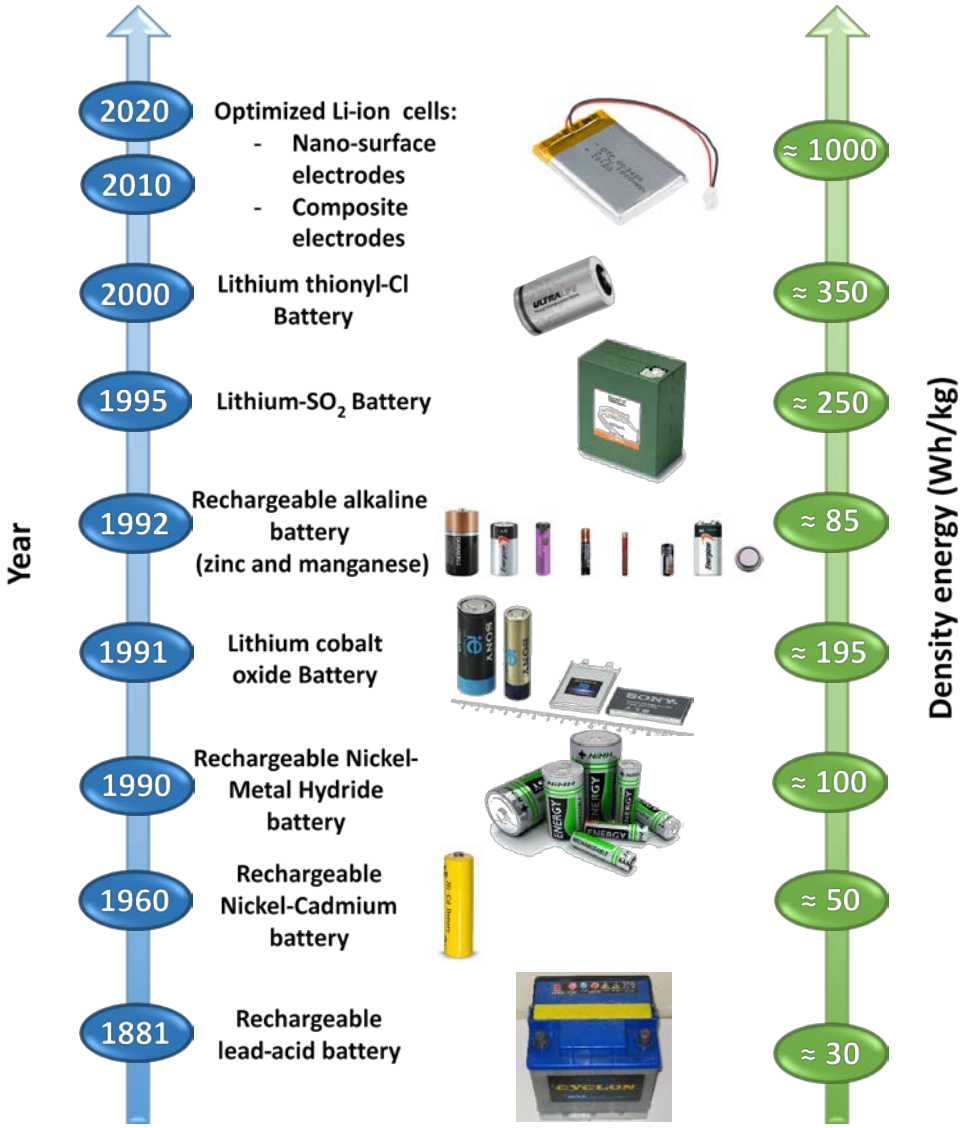

Figure 1.3. Battery evolution with respect to their energy density.

cells have a relatively large power-to-weight ratio. These features, along with their low cost, make them attractive for use in motor vehicles to provide the high current required by starter motors.

Ni-Cd and Ni-MH batteries are types of rechargeable batteries that use nickel oxide hydroxide at the positive electrode and an aqueous solution of KOH as electrolyte [9]. The negative electrode is metallic cadmium (Cd) for Ni-Cd battery whereas, for Ni-MH

battery, it is a hydrogen-absorbing alloy. For many years, Ni-Cd batteries were the most suitable for portable communications systems and computing equipment until the development of lithium-ion batteries. Ni-MH batteries can have two to three times the capacity of Ni-Cd batteries of the same size, with significantly higher energy density, although much less than lithium-ion batteries. Ni-MH batteries are used to power hybrid vehicles and cheaper electronics.

The lithium-ion battery [10–12] owes its name to the exchange of the Li^+ ion between the graphite (Li_xC_6) anode and a layered-oxide ($Li_{1-x}TMO_2$) cathode, with TM being a transition metal (usually cobalt but sometimes nickel or manganese). Lithium is the lightest of all metals, showing a large electrochemical potential and high energy density relative to its weight. The energy stored is five times higher than that with lead-acid batteries. Successive work by Stanley Whittingham in the early 1970s, by John Goodenough in 1980, and Akira Yoshino in 1985 on the lithium battery increased the interest in developing lithium-ion batteries, and in 1991, the Sony Corporation commercialized the first lithium-ion battery [13]. The Nobel Prize in Chemistry 2019 was awarded to the three researchers for their contributions to the development of the Li-ion battery [14]. Indeed, Li-ion batteries have brought a great benefit to humankind, as they have enabled the development of laptop computers, mobile phones, EVs, and the storage of energy generated by solar and wind power. Nowadays, Li-ion batteries are the most widely used and still show promising growth potential.

By comparing Li-ion and Ni-Cd batteries, the energy density of Li-ion batteries is approximately twice as large as the energy density of Ni-Cd batteries [6]. On the other hand, the charging cycle shows similar characteristics to Ni-Cd and Li-ion batteries. Li-ion

electrochemical cells show high voltages and in the case, for example, of an electrical apparatus requiring a voltage of 3.6 V, it requires just one cell instead of a package of three cells of 1.2 V for Ni-Cd batteries. Li-ion batteries show no memory effect in their charge and discharge cycles, which leads to an increased lifetime. Furthermore, their self-discharge effect is lower in comparison to Ni-Cd batteries. Despite the mentioned advantages, Li-ion batteries also show some disadvantages. For example, the temperature of Li-ion batteries should be controlled in order not to exceed 100 °C.

Alternative batteries such as organic batteries [15–18], lithium-sulfur (Li-S) batteries [19–21], and lithium-oxygen (Li-O_2) batteries [22,23], et al. are designed with high energy density to meet higher requirements for eco-friendly, sustainability, and abundant materials. However, these batteries have some challenges that still need to be improved to be used in practical applications, for example efficiency, lifespan, or poor rate capability.

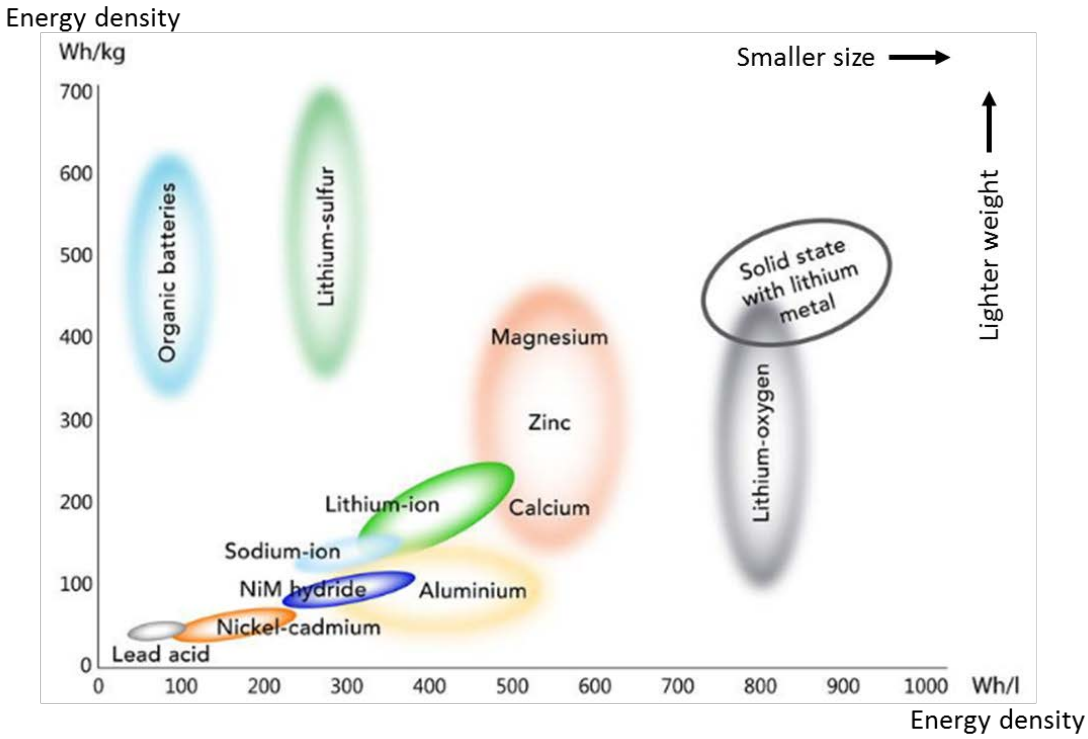

Figure 1.4. Comparison of the different battery technologies in terms of volumetric and gravimetric energy density [5].

In the automotive industry, there are many options for electric vehicle batteries, each system offering unique features with advantages and disadvantages. Currently, some of the most promising approaches are based on lithium-ion batteries, due to their high energy density [24,25].

1.2.2. Rechargeable battery technology

A battery consists of one or more electrochemical cells, connected in series or parallel, or both, depending on the desired output voltage and capacity. An electrochemical cell is a device designed to provide electric energy directly converted from chemical energy. The active materials store the chemical energy and convert it by electrochemical oxidation-reduction (redox) reaction. The system is rechargeable in the case of reversible redox reaction. It is worth noting that the term “battery” is often used while the appropriate term for the basic electrochemical unit is “cell”. However, for more simplicity, the term battery (when used) will refer to a reversible electrochemical cell.

The three main components of an electrochemical cell are [18,26]: anode, cathode, and electrolyte as represented in **Figure 1.5a**. The discharge processes of a secondary or rechargeable lithium battery are depicted in yellow in the schematic representation in **Figure 1.5a**, and in orange for the charge processes. During the discharge process, the anode is oxidized (negative electrode), and the electrons flow from the anode through the external circuit to the cathode (positive electrode), which is reduced to accepting the electrons. At the same time, cations of the electrolyte move to the cathode to ensure the charge balance, and anions towards the anode. The discharge is a spontaneous process, whereas a voltage in the opposite direction should be applied for the charge. During the

charge step, opposite redox reactions are taking place at each electrode. The current flow is reversed, cations move from the cathode to the anode and vice versa for anions. Therefore, anode and cathode are terms only valid during the discharge step of rechargeable batteries. However, in literature, negative electrodes are often referred as anodes and positive electrodes as cathodes.

The two electrodes are separated by an electrolyte, which can be solid or liquid with an insulating separator permeable. The electrolyte conducts ions between the electrodes to balance the charges; therefore, high ionic conductivity is desirable. Nevertheless, it has to be an electronic insulator to avoid the short-circuiting of the cell. Thus, the electrons generated during the chemical reactions flow through the external circuit where they provide electrical energy.

The cathode is composed of active material, conductive carbon additive, and binder, as shown in **Figure 1.5b**. The active material is the chemically active component for the reversible electrochemical redox reaction. The conductive additive is a carbon material, generally graphite, Super P, Carbon Black, or Acetylene Black. Its electronic conductor

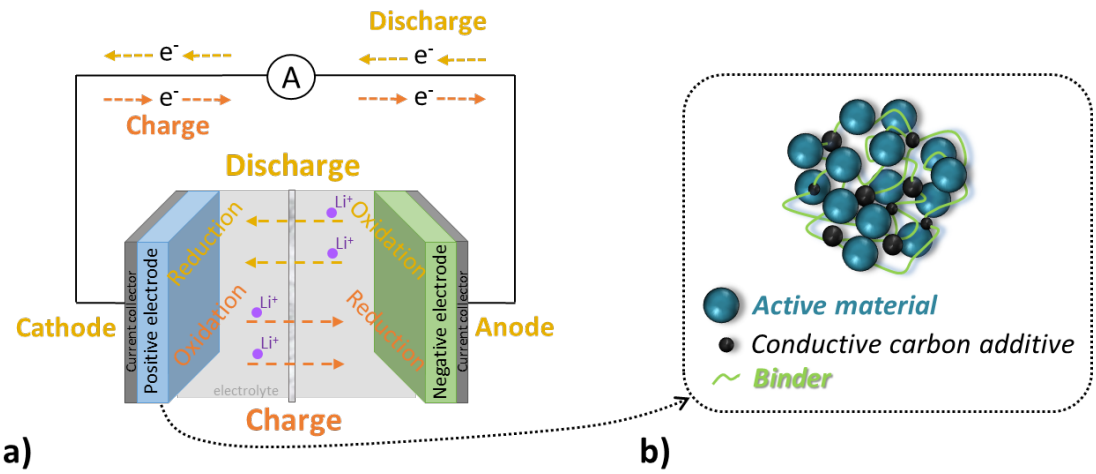

Figure 1.5. Schematic drawing representation a) for a typical lithium-ion battery (LIB); and b) for the cathode composition.

property allows for maintaining the cathode's electronic conductance. The binder is a viscous polymer that is capable of bonding the active material with the conductive additive on the current collector. The binder can provide other benefits to the cathode as explained later.

Batteries are described by specific terms [27,28], such as capacity ($mA.h.g^{-1}$), which is the amount of electrical charge that can be generated due to electrochemical reactions per unit mass in the cell. The discharge current is often expressed as a C-rate in order to normalize against battery capacity, which is often very different between batteries. A C-rate is the current needed to obtain a fully (dis)charge capacity in an established time. A 1C rate means that the discharge current will discharge the entire battery in 1 hour. The cell voltage (V) is the difference between the cathode potential and the anode potential. The energy density is the measure of how much energy a battery contains per mass ($Wh.kg^{-1}$) or volume ($Wh.L^{-1}$) and can deliver, it is the product of the cell's voltage and capacity. The power is another important parameter, which is related to the speed of access to the energy of the cell ($W.kg^{-1}$).

Cyclic voltammetry (CV) is a technique of electrochemical characterization used to study the redox properties of electrochemically active compounds [29]. This method allows the determination of redox potentials at which oxidation and reduction reactions take place. The potential of the working electrode is ramped linearly with time while measuring the current. In a cyclic voltammogram, the current is plotted versus the applied voltage. An example of a reversible redox reaction is depicted in **Figure 1.6a**. The current increases when oxidation reactions take place, and it decreases for reduction reactions. In

addition to potential values, cyclic voltammetry also provides important information about reversibility, stability, and kinetics.

The galvanostatic discharge-charge (GDC) [30] is an essential method of battery characterization where a constant current is applied (C-rate) and the cell voltage is measured. The capacity of the device is equal to the product of time and current. A pronounced plateau, as depicted in **Figure 1.6b**, indicates a lithium intercalation/deintercalation through a phase change mechanism in the system. The operating voltage of the device can be directly read from the plateau. The polarization and energy loss are indicated by the difference between the charge and discharge voltages for a complete process. Another information obtained from this experiment is the active mass utilization, which is the ratio between the experimental capacity delivered by the cell and the theoretical capacity. Coulombic efficiency is the ratio between discharge and charge capacities, and it is related to the energy that can be delivered in comparison with the energy required to charge the cell. Finally, the stability of the cell is determined by capacity retention, which is the ratio between the capacity at a specific cycle number and the initial capacity.

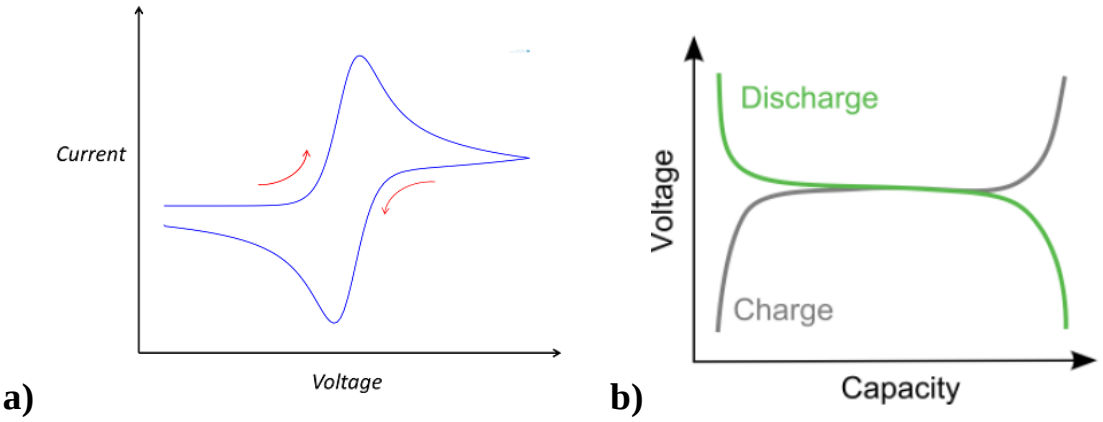

Figure 1.6. a) Cyclic voltammogram for a reversible redox process; and b) typical voltage profiles for charge (grey) and discharge (green).

1.3. Polymers in batteries

The application of polymer materials is ubiquitous in all battery components, whether in the anode, the cathode, the electrolyte, or in the separators. Depending on their role, polymers require specific properties, which can be redox active, conductive, or on the contrary insulating. Different polymers developed and tested in the literature for the binder of cathodes and solid electrolytes are detailed in the two parts below being the two research axes of this thesis.

1.3.1. Polymer binders for cathodes

Binders for cathodes [31–34] are supporting substances that have the capability of holding together the active component and conductive additive on the current collector forming integrated conductive pathways for repeatable battery operation. Even if they are added to a small portion of the electrode material (typically 2-5% of the mass in electrodes), they play multiple important roles in battery performance. The main properties of polymer binders are summarized in **Figure 1.7**. The binders should be soluble in the solvent used to make the slurry for a homogeneous distribution during the fabrication process. The presence of charges, the density, and the flexibility of the polymer chains are also helpful for good dispersive capabilities in the slurry. The adhesion to other components and to the current collector, as well as the stiffness, toughness, and hardness are important mechanical properties of the binders. Indeed, the electrode has to withstand the forces resulting from the expansion and contraction of the active materials during charge/discharge cycles. The binders are thermally, chemically, and electrochemically stable. From a thermal point of view, the binders must have a degradation temperature higher than the temperatures used for the operation of the final device as well as for the drying of the electrodes, which can reach high temperature.

Likewise, chemical and electrochemical stability are essential properties of binders to avoid degradation of the energy storage system by eventual reactions with other components or instability at high and low potentials. Ionic or electrical conduction capacities are not essential properties for binders but they are advantageous features for the energy storage device [35]. Indeed, electrical conductivity supports the need for a conductive additive for electrodes, while ionic conductivity plays a role in electrode performance. Electrical conductor functionality can be achieved in polymers via a conjugated network and free charge carriers. Whereas ionic conductivity is affected by the crystallinity and viscosity of the polymer, or can also be obtained by specific mechanisms from the presence of functional groups, such as Li ion hopping. The sustainable aspect is always important for issues of safety, ecological and renewable resources.

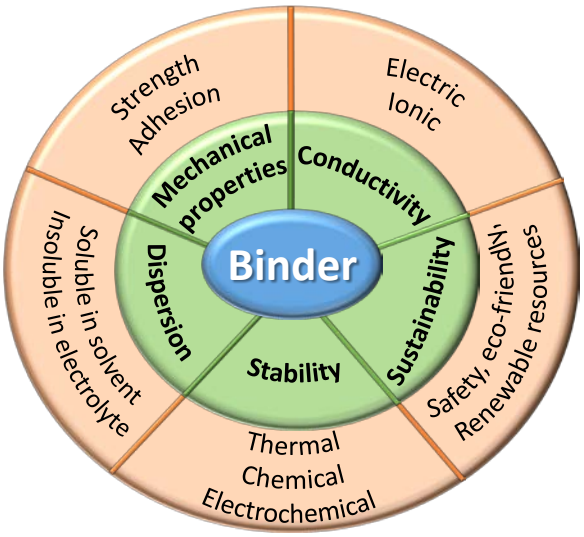

Figure 1.7. Properties of binders in energy storage devices.

Some examples of polymers used as binders or electroactive materials without other binder additives in cathode for Li-ion batteries are summarized in **Figure 1.8**, in which they are grouped into five categories according to their characteristics. The first category

concerns polymers with good mechanical properties allowing the adhesion strength between electrode laminates and current collectors. In this group, there is poly(vinylidene difluoride) (PVDF) [36], which is the most commonly used binder because of its excellent chemical and electrochemical stability. PVDF is typically taken as the reference binder and can achieve 140 mA.h.g^{-1} at 1C with a cathode composition of $LiNi_{0.33}Co_{0.33}Mn_{0.33}O_2$ (NMC) / carbon black / PVDF (90/5/5) against lithium metal. On the other hand, PVDF has disadvantages for which alternative polymers are sought. For instance, PVDF has a poor binding affinity to electrode components due to van der Waals forces, which are insufficient to hold the cell together and resist the resulting forces when changing volume during charge/discharge cycles [37]. In addition, PVDF requires conductive additives for proper electrode function because it is electrically insulating. PVDF also has issues in the manufacture of electrodes with the organic solvent N-methyl-2-pyrrolidone (NMP) which is toxic and has a high boiling point of around 203 ºC, therefore requiring more energy and higher temperatures for drying the electrodes. Although PVDF is used for its chemical stability to be inert with the electrolyte, it can swell or dissolve on exposure to electrolyte solvent, leading to capacity loss of the cell.

Among the investigations on alternative binders to PVDF, four categories of binders are discussed here. One of the categories of binders are sustainable polymers. They are beneficial for the environment, and generally, they show good mechanical properties due to their composition of several hydroxyl and carboxyl groups [38]. The three other categories are differentiated by the polymer property such as electronic or ionic conductivity, or redox activity, which provide contributions to the electrochemical energy storage system.

The carboxymethyl cellulose (CMC) and xanthan gum (XG) are proposed as binders for their mechanical and sustainable properties [39,40]. Indeed, they are no-toxic water-soluble polysaccharides from renewable resources. They are usually employed with $LiFePO_4$ (LFP) prepared with deionized water. The carboxylic and hydroxyl groups along the CMC or XG chains contribute to large numbers of possible active bonding sites between active material, conductive agent, and current collector facilitating electrical and ionic conducting, holding the electrode integrity, and ensuring good dispersion during the slurry production and electrode fabrication process. The capacities of 135 and 130 $mA.h.g^{-1}$ at 1C rate are reported for CMC and XG respectively, for LFP/carbon black/binder (90:5:5) against lithium metal. A version of CMC functionalized with Li (CMC-Li) is suggested as a cathode binder by Qiu et al. [41]. In addition to the benefits of CMC explained above, CMC-Li acts as an ion-conducting polymer to enhance the Li^+ ion flux during charge/discharge. A capacity of 140 $mA.h/g^{-1}$ at 1C rate is obtained with a cell configuration of Li || LFP / acethylene black / CMC-Li (80/10/10).

Other ionic conductive polymers such as imidazolium-based PILs are tested as binders in LFP cathodes in the work of Lee et al. [42]. In particular, the poly(1-(4-vinylbenzyl)-2,3-dimethylimidazolium TFSI) (P3 in **Figure 1.8**) showed cycling stability, and specific capacity improved due to the very effective Li^+ conducting pathways. A capacity of 137 $mA.h.g^{-1}$ at 1C rate is reached in cell Li || LFP / acetylene black / binder P3 (80/10/10).

A redox-active polyimide (PI) is tested as a binder in LFP cathode by Q. Zhang et al. [43]. They showed a larger capacity with 140 $mA.h.g^{-1}$ reached at 1C rate with cell configuration of Li || LFP / conductive carbon / binder (80/10/10) with a mix of binder

PVDF:PI (30:70). In addition, a better rate capability and great cycling stability are highlighted due to a superior binding ability compared to the LFP cathode with PVDF binder. Furthermore, redox-active polymers with catechol groups are tested as electroactive materials without other binder additives in cathode for Li-organic batteries by N. Patil et al. [44] and shown reversible redox activity, high theoretical capacity, and high redox potential. For example, the homopolymer Poly(4-vinyl catechol) (P($4VC_{100}$)) showed a capacity of 325 mA.h.g^{-1} at 1C for a configuration cell of Li || P($4VC_{100}$) / buckypaper (20/80). In addition, the performances have been improved with the incorporation of single-ion conducting functionalities to the catechol polymer by the design of the single-ion conducting redox-active copolymer, P($4VC_{86}$-*stat*-$LiSS_{14}$), that showed a capacity of 380 mA.h.g^{-1} at 1C. This copolymer showed a significant improvement in the electrochemical behavior and the kinetic limitations intrinsic to the electrodes benefiting from the hybridization of both the redox-active catechol and the ion-conducting anion pendants in the same polymer chain.

The last category of binders are polymers functionalized with electronic conductive properties. Polypyrrole, polyaniline (PANI), and polythiophene are well known examples of conducting polymers. The electronic conductive properties provide improvement in the capacity and the rate capability and are good functional binder candidates in Li batteries. For example, poly(3,4-ethylenedioxythiphene):polystyrene (PEDOT:PSS) used as binder in cell Li || LFP / PEDOT:PSS (92/8) achieved 105 mA.h.g^{-1} at 1C rate [45] and PANI used as binder in cell Li || LFP / acetylene black / PANI (85/9/6) reached 135 mA.h.g^{-1} at 1C rate [46].

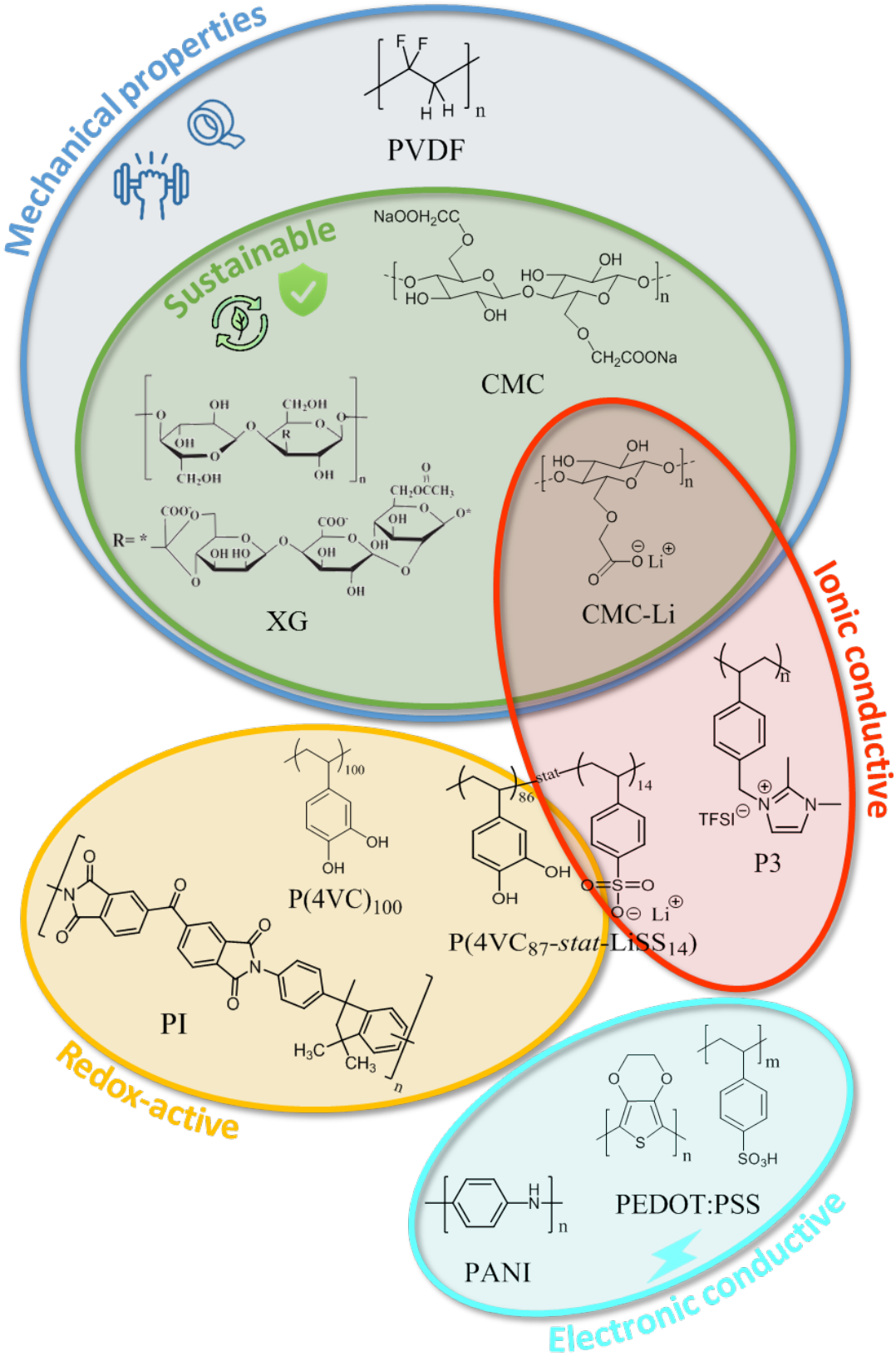

Figure 1.8. Examples of polymers for cathodes for Li-ion batteries grouped by properties.

1.3.2. Solid polymer electrolytes

As explained previously, the electrolyte plays an important role in ionic conduction between the electrodes during charging and discharging cycles. Electrolytes can be liquid or solid materials, which include a lithium salt. The electrolytes usually used in commercial Li-ion batteries are liquids because they have high ionic conductivity and excellent wettability on electrode surfaces. However, they have some drawbacks such as problems associated with safety due to the risk of solvent leakage, the use of volatile and flammable organic solvents, and electrochemical instabilities. Solid electrolytes can overcome the drawbacks of liquid electrolytes. Indeed, solid electrolytes have higher thermal stability and they are safer, without the risk of leakage or combustible reaction products. Nevertheless, the disadvantages of solid electrolytes are their low ionic conductivity that is lower than that of liquid ones, poor cycle performance, and poor interface with the electrode.

Among solid polymer electrolytes, the two categories are distinguished such as solid polymer electrolytes (SPEs) and gel polymer electrolytes (GPEs). GPEs are in fact an intermediate state between liquid and solid electrolyte. They have the advantage of possessing both the cohesive property of solids and the diffusive property of liquids [47]. SPEs are the complex between a polymer matrix swollen with a lithium salts, which are dissolved with the polymeric linkage. The main properties sought for SPEs are high ionic conductivity, good mechanical strength, appreciable transference number, thermal and electrochemical stabilities, and good compatibility with electrodes. One of the biggest challenges is to have high ionic conductivity for SPEs for good battery operation. Indeed,

in general, the ionic conductivity of SPEs is less than 10^{-5} S.cm^{-1} at 25ºC [48,49] and the needed value ranges between 10^{-4} and 10^{-3} S.cm^{-1}

Polyethers are the most studied polymers for SPEs due to their electrochemical stability and because they have a good ability to dissolve lithium salts by complexation of ions via bonding interactions between ether oxygens and ions [50]. In particular, poly(ethylene oxide) (PEO) is a very promising candidate [51]. Its structure of flexible segments of ethylene oxide and ether oxygen atoms allows it to have good mechanical properties and a very good complexing agent for lithium ions, as explained above. The price is another advantage of PEO use, as well as its commercial availability. However, the ionic conductivity of PEO is impacted by the semi-crystalline nature and reaches only 10^{-8} to 10^{-4} S.cm^{-1} at temperatures between 40 and 100 ºC. To increase the ionic conductivity of PEO, methods of copolymerization, blending, or introduction of branching or cross-linking are studied [52,53,54]. For example, PEO SPE with 20 wt. % of $LiPF_6$ reached 1.5 x 10^{-4} S.cm^{-1} at 25 ºC [55].

Furthermore, various host polymers for the preparation of polymeric electrolytes are used. Among them, the most studied ones in the literature are polyacrylonitrile (PAN), polymethylmethacrylate (PMMA), PVDF, or poly(vinylidene fluoride-hexafluoro propylene) (PVDF-HFP) [56]. As examples of ionic conductivity values at 30 ºC, 8 x 10^{-5} S.cm^{-1} was measured for PAN-based SPE containing LiTFSI salt [57], and 3 x 10^{-5} S.cm^{-1} for PMMA-based SPE with $LiClO_4$ salt [58].

Single-ion conducting polymer electrolytes (SICPEs) are a family of SPEs composed of an anionic polymer with lithium counter-cation. They have the advantage to have a

cationic transference number close to unity ($t_{Li^+} \approx 1$) and support the ionic conductivity [49]. For example, 10^{-5} S.cm^{-1} at 40 ºC was measured for lithium poly(4-styrenesulfonyl(trifluoromethylsulfonyl)imide) (PSTFSI) polyelectrolytes [59], and 6×10^{-6} S cm^{-1} at 25 ºC for lithium polyvinyl alcohol oxalate borate (LiPVAOB) [60]. J. Olmedo-Martínez et al. [61] suggested a mixture of PEO with poly(lithium 1-[3-(methacryloyloxy) propylsulfonyl]-1-(trifluoromethanesulfonyl) imide) (PLiMTFSI). After optimization of the blend proportion and molecular weight, an ionic conductivity of 2.1×10^{-4} S.cm^{-1} was obtained at 70 °C. Another example that can be cited, is the work of L. Meabe et al. [62] where copolymers with ethylene oxide units and lithium bis(fluorosulfonyl)imide salt (LiFSI) were synthesized and showed high ionic conductivity of 3.2×10^{-5} S.cm^{-1} at 25°C.

1.4. Motivation and objectives

In order to move away from fossil fuel emissions toward renewable energy sources, the development of more efficient, cheap, safe, and sustainable electrochemical energy storage technologies is essential. This topic concerns in particular the energy storage systems for EVs, which in the near future will largely replace petrol vehicles. The rechargeable battery is the core component of EVs, which requires high performance. Lithium-ion batteries are hugely used in EV applications due to their lucrative features such as lightweight, fast charging, high energy density, low self-discharge, and long lifespan. However, they still have some challenges due to their complex electrochemical reactions, stability, and performance degradation, as well as their cost and safety, especially for flammable liquid electrolytes.

In this context, two main axes of improvement for lithium-ion batteries are studied in this thesis. The first goal is the improvement of the battery performance through the development of functional polymers to be used as a binder in the cathode. The challenges of binder in the cathode are the sustainability, processing, and the inherent (ionic or electronic) conductivity or redox property to improve the performance (energy density) of the battery. The second axis of improvement in this work is the development of solid polymer electrolytes (SPEs) aimed at improving safety by solving the possibilities of risks of leaks of flammable toxic liquids and the problems related to dendrite growth. The challenges of the SPEs development are obtaining solid polymers with high ionic conductivity and lithium transference number and integrating them into a battery.

Within this scope, the specific objectives of this thesis concerning the development of functional binders for cathodes are:

- Synthesis and characterization of poly(diallyldimethylammonium) type poly(ionic liquid)s (PILs) functionalized with fluorinated and redox-active anions for Li-ion batteries.
- Study of structural and electrochemical properties of the synthesized PILs.
- Investigate the potential application of these PILs as binders in high voltage NMC cathodes in Li-ion batteries.

Finally, the specific objectives of this thesis for the development of solid polymer electrolytes are:

- Synthesis and characterization of single lithium-ion conducting polymer electrolytes (SLICPEs) based on borate group.

- Study of the ionic conductivity of the SLICPEs and the effects related to the different substituents of the boron atom in the polymers.
- Investigate the electrochemical properties of the SLICPEs for their application in the batteries.

1.5. Outline of the thesis

In chapter 1, a brief introduction to energy consumption in the European Union presents the importance related of batteries for vehicles. Then an overview of electrochemical energy storage with its important applications and their evolution are explained. The motivation and goals of this thesis are also presented in this chapter. The most advanced lithium-ion battery technologies are described and the needs and challenges for the development of polymer binders and solid polymer electrolyte materials.

In Chapter 2, two families of Poly(diallyldimethylammonium) PDADMA-based PILs are presented in two distinct parts. The first part presents a family of PDADMA-based PILs containing fluorine content in the counter anions and are ionic conductive polymers. The second part shows a PDADMA-based PIL family composed of counter-anions with redox-active functions. The synthesis and characterization of PILs functionalized with fluorinated and redox-active anions are presented. Afterward, the electrochemical activity of redox-active PILs is studied, and finally, the application of PDADMA-based PILs as binders for high voltage NMC-based cathodes for Li-ion batteries is presented with the comparison with the conventional PVDF binder.

In Chapter 3, the synthesis and characterization of new SLICPEs based on borate group with different functions are reported. An in-depth study of the ionic conductivity of SLICPEs and the effect of different substituents is presented. To end, the single-ion polymer electrolytes with optimized ionic conductivity are selected for electrochemical characterizations and tested as solid electrolytes in a battery.

In Chapter 4, the most relevant conclusions of this thesis are summarized.

1.6. References

(1) Larcher, D.; Tarascon, J. M. Towards Greener and More Sustainable Batteries for Electrical Energy Storage. *Nat. Chem.* **2015**, *7* (1), 19–29.

(2) European, C. COMMUNICATION FROM THE COMMISSION TO THE EUROPEAN PARLIAMENT, THE COUNCIL, THE EUROPEAN ECONOMIC AND SOCIAL COMMITTEE AND THE COMMITTEE OF THE REGIONS. *Mod. Healthc.* **1993**, *23* (31), 17.

(3) Krause, J.; Thiel, C.; Tsokolis, D.; Samaras, Z.; Rota, C.; Ward, A.; Prenninger, P.; Coosemans, T.; Neugebauer, S.; Verhoeve, W. EU Road Vehicle Energy Consumption and CO2 Emissions by 2050 – Expert-Based Scenarios. *Energy Policy* **2020**, *138* (December 2019), 111224.

(4) Rolison, D. R.; Nazar, L. F. Electrochemical Energy Storage to Power the 21st Century. *MRS Bull.* **2011**, *36* (7), 486–493.

(5) Dominko, R.; Fichtner, M.; Otuszewski, T.; Punckt, C.; Tarascon, J.; Vegge, T.; Dominko, R.; Edström, K.; Fichtner, M.; Punckt, C. BATTERY 2030+ Roadmap 1. **2020**.

(6) Miranda, D.; Costa, C. M.; Lanceros-Mendez, S. Lithium Ion Rechargeable Batteries: State of the Art and Future Needs of Microscopic Theoretical Models and Simulations. *J. Electroanal. Chem.* **2015**, *739*, 97–110.

(7) Armand, M.; J.-M. Tarascon. Building Better Batteries. *Sustain. Energy Fuels* **2019**, *3* (1), 280–291.

(8) Kurzweil, P. Gaston Planté and His Invention of the Lead-Acid Battery-The Genesis of the First Practical Rechargeable Battery. *J. Power Sources* **2010**, *195* (14), 4424–4434.

(9) Wang, L.; Wang, J.; Wang, L.; Zhang, M.; Wang, R.; Zhan, C. A Critical Review

on Nickel-Based Cathodes in Rechargeable Batteries. *Int. J. Miner. Metall. Mater.* **2022**, *29* (5), 925–941.

(10) J.M. Tarascon; Armand, M. Issues and Challenges Facing Rechargeable Lithium Batteries. **2001**, *414* (November), 359–367.

(11) Scrosati, B.; Garche, J. Lithium Batteries: Status, Prospects and Future. *J. Power Sources* **2010**, *195* (9), 2419–2430.

(12) Nitta, N.; Wu, F.; Lee, J. T.; Yushin, G. Li-Ion Battery Materials : Present and Future. *Biochem. Pharmacol.* **2015**, *18* (5), 252–264.

(13) Ogumi, Z.; Kostecki, R.; Guyomard, D.; Inaba, M. Lithium-Ion Batteries--The 25th Anniversary of Commercialization. *Interface Mag.* **2016**, *25* (3), 65–65.

(14) Batteries international. Whittingham, Goodenough and Yoshino: The Three Titans of the Lithium Ion Battery. 2019, pp 6–13.

(15) Shi, R.; Jiao, S.; Yue, Q.; Gu, G.; Zhang, K.; Zhao, Y. Challenges and Advances of Organic Electrode Materials for Sustainable Secondary Batteries. *Exploration* **2022**, *2* (4), 20220066.

(16) Poizot, P.; Gaubicher, J.; Renault, S.; Dubois, L.; Liang, Y.; Yao, Y. Opportunities and Challenges for Organic Electrodes in Electrochemical Energy Storage. *Chem. Rev.* **2020**, *120* (14), 6490–6557.

(17) Mauger, A.; Julien, C.; Paolella, A.; Armand, M.; Zaghib, K. Recent Progress on Organic Electrodes Materials for Rechargeable Batteries and Supercapacitors. *Materials (Basel).* **2019**, *12* (11), 1–57.

(18) Muench, S.; Wild, A.; Friebe, C.; Häupler, B.; Janoschka, T.; Schubert, U. S. Polymer-Based Organic Batteries. *Chemical Reviews*. 2016.

(19) Manthiram, A.; Fu, Y.; Chung, S. H.; Zu, C.; Su, Y. S. Rechargeable Lithium-Sulfur Batteries. *Chemical Reviews*. 2014.

(20) Zhang, Q.; Huang, Q.; Hao, S. M.; Deng, S.; He, Q.; Lin, Z.; Yang, Y. Polymers in Lithium–Sulfur Batteries. *Adv. Sci.* **2022**, *9* (2), 1–30.

(21) Xiang, J.; Zhao, Y.; Wang, L.; Zha, C. The Presolvation Strategy of Li2S Cathodes for Lithium-Sulfur Batteries: A Review. *J. Mater. Chem. A* **2022**, *10* (19), 10326–10341.

(22) Dang, C.; Mu, Q.; Xie, X.; Sun, X.; Yang, X.; Zhang, Y.; Maganti, S.; Huang, M.; Jiang, Q.; Seok, I.; Du, W.; Hou, C. Recent Progress in Cathode Catalyst for Nonaqueous Lithium Oxygen Batteries: A Review. *Adv. Compos. Hybrid Mater.* **2022**, *5* (2), 606–626.

(23) Dou, Y.; Xie, Z.; Wei, Y.; Peng, Z.; Zhou, Z. Redox Mediators for High-Performance Lithium-Oxygen Batteries. *Natl. Sci. Rev.* **2022**, *9* (4).

(24) Julien, C.; Mauger, A.; Vijh, A.; Zaghib, K. *Lithium Batteries: Science and Technology*; 2015.

(25) Hannan, M. A.; Lipu, M. S. H.; Hussain, A.; Mohamed, A. A Review of Lithium-Ion Battery State of Charge Estimation and Management System in Electric Vehicle Applications: Challenges and Recommendations. *Renew. Sustain. Energy Rev.* **2017**, *78* (August 2016), 834–854.

(26) Korthauer, R. *Lithium-Ion Batteries: Basics and Applications*; Korthauer, R., Ed.; Springer Berlin Heidelberg: Berlin, Heidelberg, 2018.

(27) Li, J.; Arbizzani, C.; Kjelstrup, S.; Xiao, J.; Xia, Y. yao; Yu, Y.; Yang, Y.; Belharouak, I.; Zawodzinski, T.; Myung, S. T.; Raccichini, R.; Passerini, S. Good Practice Guide for Papers on Batteries for the Journal of Power Sources. *J. Power Sources* **2020**, *452* (February), 227824.

(28) Piernas Muñoz, M. J.; Castillo Martínez, E. Introduction to Batteries. *SpringerBriefs Appl. Sci. Technol.* **2018**, No. December, 1–8.

(29) Elgrishi, N.; Rountree, K. J.; McCarthy, B. D.; Rountree, E. S.; Eisenhart, T. T.; Dempsey, J. L. A Practical Beginner's Guide to Cyclic Voltammetry. *J. Chem. Educ.* **2018**, *95* (2), 197–206.

(30) Bonnick, P.; Talaie, E.; Pang, Q.; Nazar, L. F.; Sun, X.; Liang, X. Methods and Protocols for Electrochemical Energy Storage Materials Research. *Chem. Mater.* **2016**, *29* (1), 90–105.

(31) Cholewinski, A.; Si, P.; Uceda, M.; Pope, M.; Zhao, B. Polymer Binders: Characterization and Development toward Aqueous Electrode Fabrication for Sustainability. *Polymers (Basel).* **2021**, *13* (4), 1–20.

(32) Chen, H.; Ling, M.; Hencz, L.; Ling, H. Y.; Li, G.; Lin, Z.; Liu, G.; Zhang, S. Exploring Chemical, Mechanical, and Electrical Functionalities of Binders for Advanced Energy-Storage Devices. *Chem. Rev.* **2018**, *118* (18), 8936–8982.

(33) Nguyen, V. A.; Kuss, C. Review—Conducting Polymer-Based Binders for Lithium-Ion Batteries and Beyond. *J. Electrochem. Soc.* **2020**, *167* (6), 065501.

(34) Yuan, H.; Huang, J.-Q.; Peng, H.-J.; Titirici, M.-M.; Xiang, R.; Chen, R.; Liu, Q.; Zhang, Q. A Review of Functional Binders in Lithium-Sulfur Batteries. *Adv. Energy Mater.* **2018**, *1802107*, 1802107.

(35) Lestriez, B. Functions of Polymers in Composite Electrodes of Lithium Ion Batteries. *Comptes Rendus Chim.* **2010**, *13* (11), 1341–1350.

(36) Wang, M.; Hu, J.; Wang, Y.; Cheng, Y.-T. The Influence of Polyvinylidene Fluoride (PVDF) Binder Properties on LiNi0.33Co0.33Mn0.33O2 (NMC) Electrodes Made by a Dry-Powder-Coating Process. *J. Electrochem. Soc.* **2019**, *166* (10), A2151–A2157.

(37) Y. Shi, X.Zhou, and G. Y. Material and Structural Design of Novel Binder Systems for High-Energy High-Power Lithium-Ion Batteries. 2017.

(38) Bresser, D.; Buchholz, D.; Moretti, A.; Varzi, A.; Passerini, S. Alternative Binders for Sustainable Electrochemical Energy Storage-the Transition to Aqueous Electrode Processing and Bio-Derived Polymers. *Energy Environ. Sci.* **2018**, *11* (11), 3096–3127.

(39) Li, J.; Klöpsch, R.; Nowak, S.; Kunze, M.; Winter, M.; Passerini, S. Investigations on Cellulose-Based High Voltage Composite Cathodes for Lithium Ion Batteries. *J. Power Sources* **2011**, *196* (18), 7687–7691.

(40) He, J.; Zhong, H.; Wang, J.; Zhang, L. Investigation on Xanthan Gum as Novel Water Soluble Binder for LiFePO 4 Cathode in Lithium-Ion Batteries. *J. Alloys Compd.* **2017**, *714*, 409–418.

(41) Qiu, L.; Shao, Z.; Wang, D.; Wang, W.; Wang, F.; Wang, J. Enhanced Electrochemical Properties of LiFePO4 (LFP) Cathode Using the Carboxymethyl Cellulose Lithium (CMC-Li) as Novel Binder in Lithium-Ion Battery. *Carbohydr. Polym.* **2014**, *111*, 588–591.

(42) Lee, J. S.; Sakaushi, K.; Antonietti, M.; Yuan, J. Poly(Ionic Liquid) Binders as Li+ Conducting Mediators for Enhanced Electrochemical Performance. *RSC Adv.* **2015**, *5* (104), 85517–85522.

(43) Zhang, Q.; Sha, Z.; Cui, X.; Qiu, S.; He, C.; Zhang, J.; Wang, X.; Yang, Y. Incorporation of Redox-Active Polyimide Binder into LiFePO4cathode for High-Rate Electrochemical Energy Storage. *Nanotechnol. Rev.* **2021**, *9* (1), 1350–1358.

(44) Patil, N.; Aqil, A.; Ouhib, F.; Admassie, S.; Inganäs, O.; Jérôme, C.; Detrembleur, C. Bioinspired Redox-Active Catechol-Bearing Polymers as Ultrarobust Organic Cathodes for Lithium Storage. *Adv. Mater.* **2017**.

(45) Das, P. R.; Komsiyska, L.; Osters, O.; Wittstock, G. PEDOT: PSS as a Functional Binder for Cathodes in Lithium Ion Batteries. *J. Electrochem. Soc.* **2015**, *162* (4),

A674–A678.

(46) Tamura, T.; Aoki, Y.; Ohsawa, T.; Dokko, K. Polyaniline as a Functional Binder for LiFePO4 Cathodes in Lithium Batteries. *Chem. Lett.* **2011**, *40* (8), 828–830.

(47) Manuel Stephan, A. Review on Gel Polymer Electrolytes for Lithium Batteries. *Eur. Polym. J.* **2006**, *42* (1), 21–42.

(48) Zhang, H.; Li, C.; Piszcz, M.; Coya, E.; Rojo, T.; Rodriguez-Martinez, L. M.; Armand, M.; Zhou, Z. Single Lithium-Ion Conducting Solid Polymer Electrolytes: Advances and Perspectives. *Chem. Soc. Rev.* **2017**, *46* (3), 797–815.

(49) Zhu, J.; Zhang, Z.; Zhao, S.; Westover, A. S.; Belharouak, I.; Cao, P. F. Single-Ion Conducting Polymer Electrolytes for Solid-State Lithium–Metal Batteries: Design, Performance, and Challenges. *Adv. Energy Mater.* **2021**, *11* (14), 1–18.

(50) Croce, F.; Appetecchi, G. B.; Persi, L.; Scrosati, B. Nanocomposite Polymer Electrolyte for Lithium Batteries. **1998**, *394* (July), 456–458.

(51) Mindemark, J.; Lacey, M. J.; Bowden, T.; Brandell, D. Beyond PEO—Alternative Host Materials for Li+-Conducting Solid Polymer Electrolytes. *Prog. Polym. Sci.* **2018**, *81*, 114–143.

(52) Bao, J.; Qu, X.; Qi, G.; Huang, Q.; Wu, S.; Tao, C.; Gao, M.; Chen, C. Solid Electrolyte Based on Waterborne Polyurethane and Poly(Ethylene Oxide) Blend Polymer for All-Solid-State Lithium Ion Batteries. *Solid State Ionics* **2018**, *320* (February), 55–63.

(53) Li, Y. J.; Fan, C. Y.; Zhang, J. P.; Wu, X. L. A Promising PMHS/PEO Blend Polymer Electrolyte for All-Solid-State Lithium Ion Batteries. *Dalt. Trans.* **2018**, *47* (42), 14932–14937.

(54) Jiang, Y.; Yan, X.; Ma, Z.; Mei, P.; Xiao, W.; You, Q.; Zhang, Y. Development of the PEO Based Solid Polymer Electrolytes for All-Solid State Lithium Ion

Batteries. **2018**, No. 4, 1–13.

(55) Nurul, S.; Mohd, A.; Tajuddin, N. A. A Review : Ionic Conductivity of Solid Polymer Electrolyte Based Polyethylene Oxide. **2021**, *16*, 1–15.

(56) Sashmitha, K.; Rani, M. U. A Comprehensive Review of Polymer Electrolyte for Lithium-Ion Battery. *Polym. Bull.* **2022**, No. 0123456789.

(57) Gao, H.; Grundish, N. S.; Zhao, Y.; Zhou, A.; Goodenough, J. B. Formation of Stable Interphase of Polymer-in-Salt Electrolyte in All-Solid-State Lithium Batteries. *Energy Mater. Adv.* **2021**, *2021*.

(58) Rajendran, S.; Mahendran, O.; Kannan, R. Ionic Conductivity Studies in Composite Solid Polymer Electrolytes Based on Methylmethacrylate. *J. Phys. Chem. Solids* **2002**, *63* (2), 303–307.

(59) Meziane, R.; Bonnet, J.; Courty, M.; Djellab, K.; Armand, M. Single-Ion Polymer Electrolytes Based on a Delocalized Polyanion for Lithium Batteries. *Electrochim. Acta* **2011**, *57*, 14–19.

(60) Zhu, Y. S.; Wang, X. J.; Hou, Y. Y.; Gao, X. W.; Liu, L. L.; Wu, Y. P.; Shimizu, M. A New Single-Ion Polymer Electrolyte Based on Polyvinyl Alcohol for Lithium Ion Batteries. **2013**, *87*, 113–118.

(61) Olmedo-Martínez, J. L.; Porcarelli, L.; Porcarelli, L.; Alegría, Á.; Alegría, Á.; Mecerreyes, D.; Mecerreyes, D.; Müller, A. J.; Müller, A. J. High Lithium Conductivity of Miscible Poly(Ethylene Oxide)/Methacrylic Sulfonamide Anionic Polyelectrolyte Polymer Blends. *Macromolecules* **2020**, *53* (11), 4442–4453.

(62) Meabe, L.; Goujon, N.; Li, C.; Armand, M.; Forsyth, M.; Mecerreyes, D. Single-Ion Conducting Poly(Ethylene Oxide Carbonate) as Solid Polymer Electrolyte for Lithium Batteries. *Batter. Supercaps* **2020**, *3* (1), 68–75.

Chapter 2. Pyrrolidinium-based poly(ionic liquid) binders with fluorinated and redox-active anions for Li-ion batteries

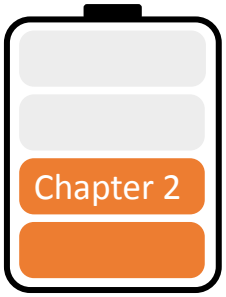

2.1. Introduction

Many studies on developing novel materials to improve the performance of Li-ion batteries (LIBs) have been reported, including redox-active materials [1] for positive and negative electrodes, or ionic conducting polymers for electrolyte and binder applications [2–4]. Although binders comprise only 2–5% of the mass in commercial electrode configuration, their role is very important to achieve high performance and long cycle lifes [5–7]. The binder is responsible for providing structural integrity to the electrode and ensures good contact between the redox-active material, the conductive additive and the current collector. Poly(vinylidene difluoride) (PVDF) and its copolymers are the standard choice for binder in lithium-ion batteries. The ionic conductivity in electrodes with PVDF binders occurs by the absorption of liquid electrolyte onto the electrode surface. The ionic transport from the electrolyte to the active material of the electrode is essential to facilitate its charge and discharge. Thus, developing innovative polymer binders with good adhesion and ion transport or redox active properties are important to achieve high-rate capability and cycling stability in next-generation lithium batteries. In this research field,

many polymers are being investigated including water processable polymers [8–10] and biopolymers such as carboxymethyl cellulose [11–14].

An alternative approach is the use of ionic conductive polymers such as poly(ionic liquid)s (PILs) or single-ion conducting polymers as electrode binders to improve the whole ionic conductivity through the cell, especially in solid-state batteries [15–17]. PILs are ionic polymers where typically cationic or anionic species of ILs are bonded to the polymer backbone and have the advantages of ionic conductivity, flexibility and wide electrochemical stability window [5,18–20]. Several works have proposed and identified the advantages on the use of imidazolium type PILs as binders in different battery electrodes, including lithium-sulfur (Li-S) [17] and lithium-ion batteries [5,19–21]. One of the most studied PILs is based on the pyrrolidinium type poly(diallyldimethylammonium) bis(trifluoro-methanesulfonyl)imide (PDADMA-TFSI), which has been applied in different areas ranging from polymer electrolytes for batteries to gas separation membranes or sensors [22,23]. As an example, Lee et al. studied imidazolium based PILs in $LiFePO_4$ (LFP) cathodes and showed that both the cycling stability and specific capacity improved, as a consequence of very effective Li^+ and electron conducting pathways when combined with carbon additive [24].

Others functionality such as redox-activity can be crucial to increase the charge kinetics of LIBs. Redox-active polymers have gained great interest as electroactive materials to replace inorganic ones in Li-organic batteries due to their high-rate performances [1,25,26]. Moreover, it has been shown that the use of redox polymers as binders can not only improve the charging kinetics of LIB, but also contribute to extra capacity due to the existence of reversible redox groups. For instance, K. Hatakeyama-

Sato et al. presented several non-conjugated redox-active polymers with electron/ion conductor properties used as binders in Li-ion batteries, such as radical-substituted polyether or thianthrene polymer which showed fast kinetic and facilitated charge/discharge reactions [27]. In the work of Q. Zhang et al., the redox-active polyimide was incorporated as a binder into the LFP cathode and showed larger capacity, better rate capability, and great cycling stability due to a superior binding ability compared to the LFP cathode with PVDF binder [28]. For Li-S batteries, S. Kim et al. have reported polymer binder system based on poly(acrylic acid) with a grafted redox-mediating function, which is benzo(ghi)perylene imide [29]. The results showed that the redox-mediating function assists in the sulfur utilization with the reduction of soluble lithium polysulfide to insoluble Li_2S at the sulfur cathode, it suppresses the shuttle effect and improves battery performance. Among the different types of redox polymers, polymers containing catechol groups are really encouraging as cathode materials in Li-organic batteries due to their reversible redox activity, high theoretical capacity and high redox potential [30,31,32].

In this work, two families of PDADMA based poly(ionic liquid)s are presented in two distinct parts, the ionic conductive polymers in the first part and redox-active polymers in the second part. In the first part, four variants of PDADMA based poly(ionic liquid)s are presented containing counter anions with highly delocalized charge density due to their fluorine content: bis(fluorolsulfonyl)imide (FSI), bis(trifluoromethylsulfonyl)imide (TFSI), bis(perfluoroethylsulfonyl)imide (BETI) and nonafluoro-1-butanesulfonate (CFSO). In the second part, four new PDADMA based poly(ionic liquid)s are proposed composed of counter-anions with redox-active functions due to catechol groups: 3,4-Dihydroxybenzoic acid (3,4DHB), 2,5-Dihydroxybenzoic

acid (2,5DHB), 3,4,5-Trihydroxybenzoic acid (3,4,5THB or Gallic acid), 2,3,4-Trihydroxybenzoic acid (2,3,4THB).

In each part, the chemical structure, thermal stability and solubility of the polymers were evaluated by NMR, FTIR and solubility tests in carbonate and N-Methyl-2-pyrrolidone (NMP) solvents to assess their potential application as battery binders. Afterward, the synthesized PDADMA polymers were tested as binders in high voltage NMC ($LiNiMnCoO_2$) based cathodes for Li-ion batteries and compared to the ones with the conventional binder PVDF.

2.2. Synthesis of functionalized PDADMA PILs

Two families of PILs have been synthesized from the PDADMA backbone and are differentiated by the types of counter-anions: fluorinated anions for the first category and benzoates with two or three hydroxyl groups for the second category. Generally, the syntheses of PDADMA PILs in this chapter use commercially available poly(diallyldimethylammonium chloride) (PDADMA-Cl) dissolved in a solvent (water or methanol) and through anion exchange reactions with the addition of salts or benzoates concerned, the desired polymers are obtained. The anion exchange reactions are different for the two types of synthesized PDADMA PILs with one-step of salt metathesis reaction for the family of fluorinated PDADMA PILs as reported in literature [33,34], whereas the benzoate PDADMA PILs were synthesized in two-steps anion exchange reactions with the first one using a column [34,35]. The reactions are explained in detail below and in both cases, the solvents were chosen to dissolve the reactants and precipitate the desired polymers therein, which facilitates obtaining the pure polymer.

2.2.1. Synthesis of fluorinated PDADMA PILs

Four pyrrolidinium-based poly(ionic liquid)s bearing different fluorinated contents in the counter anions, named PDADMA-FSI, PDADMA-TFSI, PDADMA-BETI and PDADMA-CFSO, were synthesized by a salt metathesis reaction between the water soluble PDADMA-Cl with the corresponding salt. As represented in **Figure 2.1**, one-step of anion exchange reaction occurs between a chloride anion and the negative ion of a commercially available monovalent salt (e.g. Z^+ = Na^+, Li^+, K^+) containing the Y^- of interest (e.g. Y^- = FSI^-, $TFSI^-$, $BETI^-$ and $C_4F_9SO_3^-$). After mixing, the poly(ionic liquid)s precipitated and were recovered quantitatively by filtration as white powders.

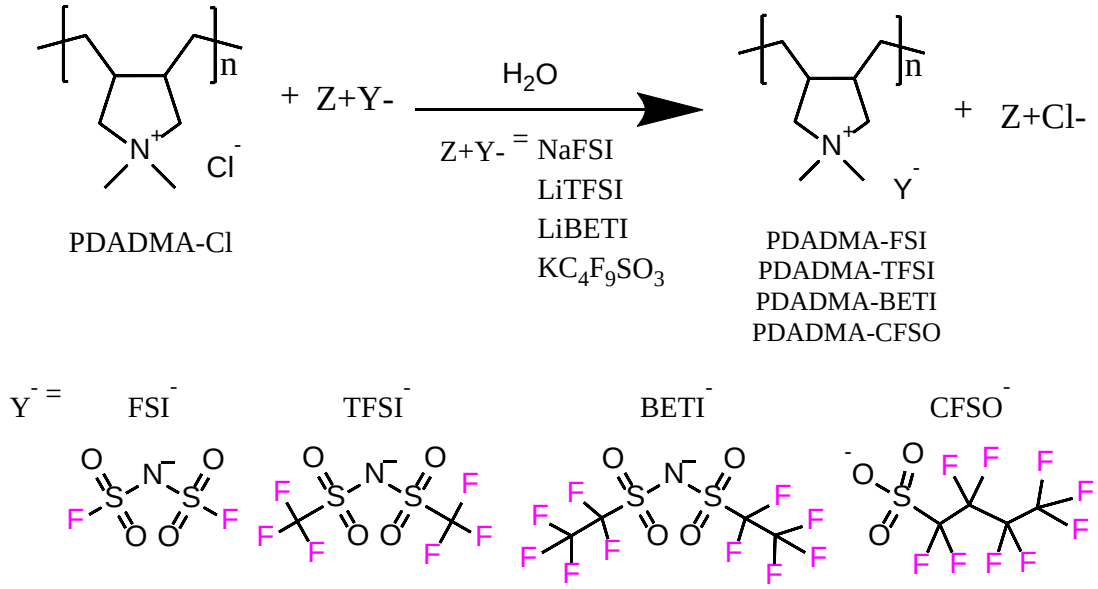

Figure 2.1. Anion exchange reaction for the synthesis of the fluorinated PDADMA PILs.

2.2.2. Synthesis of redox-active PDADMA PILs

Four new pyrrolidinium-based poly(ionic liquid)s ionicaly bonded to benzoate counter anion bearing two or three hydroxyl groups in different positions were synthesized by anion exchange reactions as shown in **Figure 2.2**. Among the four benzoate counter anions, two are distinguished by two hydroxyl groups (dihydroxybenzoate named DHB), in the *ortho* position for catechol form called 3,4DHB and in the *para* position for hydroxyquinone form called 2,5DHB corresponding to the polymers called PDADMA-3,4DHB and PDADMA-2,5DHB respectively. The other two benzoate counter anions are composed of three hydroxyl groups (trihydroxybenzoate named THB) called gallol form in different positions: 2,3,4THB and 3,4,5THB corresponding to the polymers called PDADMA-3,4,5THB and PDADMA-2,3,4THB respectively.

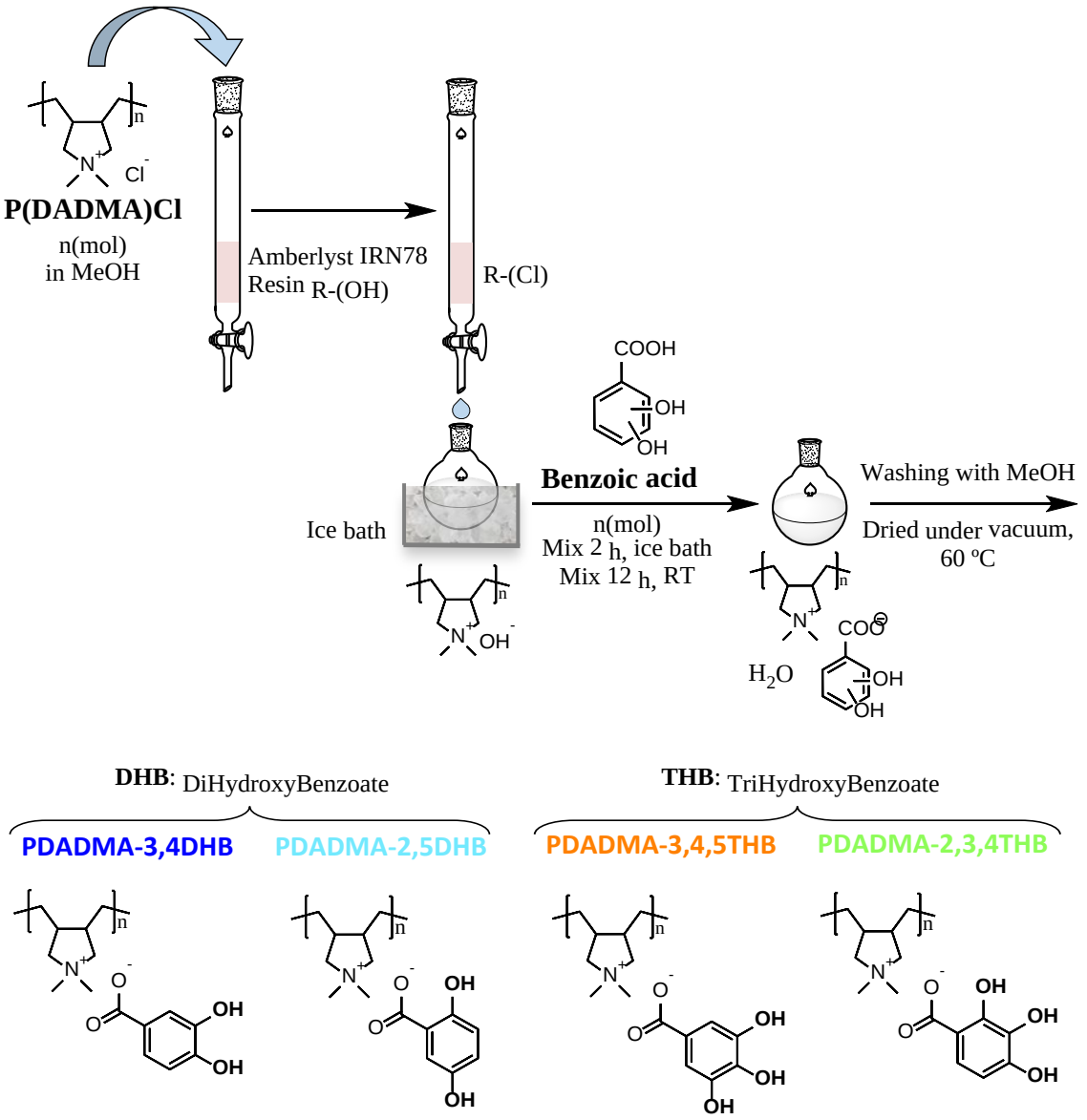

Figure 2.2. Column anion exchange reaction for the synthesis of the redox active PDADMA PILs.

The four PDADMA redox PILs were synthesized by a two-step anion exchange reaction. The first step was the preparation of poly(diallyldimethylammonium hydroxide) (PDADMA-OH) solution by passing a solution of PDADMA-Cl in methanol through a column filled with anion exchange resin (Amberlyte® IRN-78 resin hydroxide form). The PDADMA-OH collected dropwise was stabilized with an ice bath. In the second step,

the obtained PDADMA-OH was anion exchanged with the addition of equimolar amount of hydroxybenzoic acids (3,4DHB, 2,5DHB, 3,4,5THB or 2,3,4THB) depending on the desired counter anion, and stirred for 2 h at low temperature and overnight at room temperature (RT). The synthesis was carried out with methanol solvent which was chosen for its advantage of solubilizing the PDADMA-Cl and hydroxybenzoic acid reagents and of instantaneously precipitating the desired PDADMA redox PILs. Thus, the precipitates were easily washed with methanol and dried under vacuum at 60 ºC overnight.

2.3. Physicochemical characterizations of PDADMA PILs

The chemical structures of the synthesized PDADMA PILs were confirmed by ^{1}H, ^{13}C NMR and FTIR spectroscopy, and additional ^{19}F NMR were used for fluorinated PDADMA PILs family. ^{1}H, ^{13}C and ^{19}F NMR spectra of PDADMA-BETI are presented in the **Figures 2.21-2.23** with the attribution of the peaks as an example for fluorinated PDADMA PILs. **Figure 2.3** shows the ^{1}H NMR spectra for PDADMA-3,4DHB and the **Figures 2.24-2.27** show the complementary ^{1}H, and ^{13}C NMR spectra for the four PDADMA redox PILs. In the ^{1}H NMR spectra, the peaks attributed in high fields (4.0-1.0 ppm) correspond to the diallyldimethylammonium and in low fields (7.5-6.5 ppm) to the hydroxybenzoates. The peak integrals corroborate the structure and confirm the total exchange reaction with the same proportion for PDADMA and benzoate counter anion.

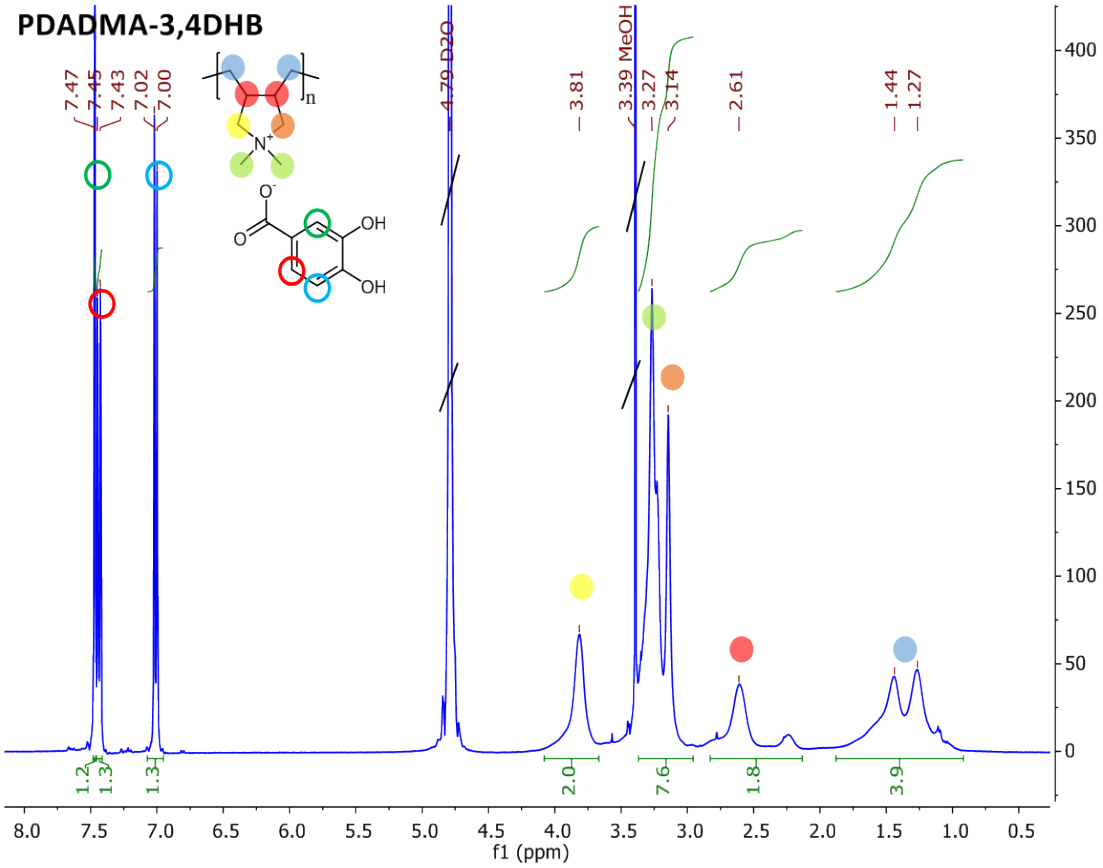

Figure 2.3. ^{1}H NMR spectra for PDADMA-3,4DHB.

FTIR spectra of the four fluorinated PDADMA PILs and PDADMA-Cl precursor are represented in **Figure 2.4a** and of the four PDADMA redox PILs in **Figure 2.4b**. Characteristics peaks of PDADMA cation were found at 2900-3100, 1640 and 1476 cm^{-1} in all PILs spectra. When compared to PDADMA-Cl precursor (**Figure 2.4a**), new peaks related to the fluorinated anions appeared at 725 and 825 cm^{-1} (attributed to S–N–S symmetric and asymmetric stretching, respectively) for all PILs except for PDADMA-CFSO; 1134 and 1346 cm^{-1} (–SO_2 asymmetric stretching) for all PILs; and 1165 cm^{-1} (C–F_3 asymmetric stretching) for all PILs. These results are consistent with previously reported fluorinated PDADMA poly(ionic liquid)s [33,36]. While the PDADMA redox PILs are characterized by bands at 3600-3300, 3100, 3000, and 1700-1500 cm^{-1} for O-H, C-H aromatics, =C-H and C=O stretches respectively (**Figure 2.4b**).

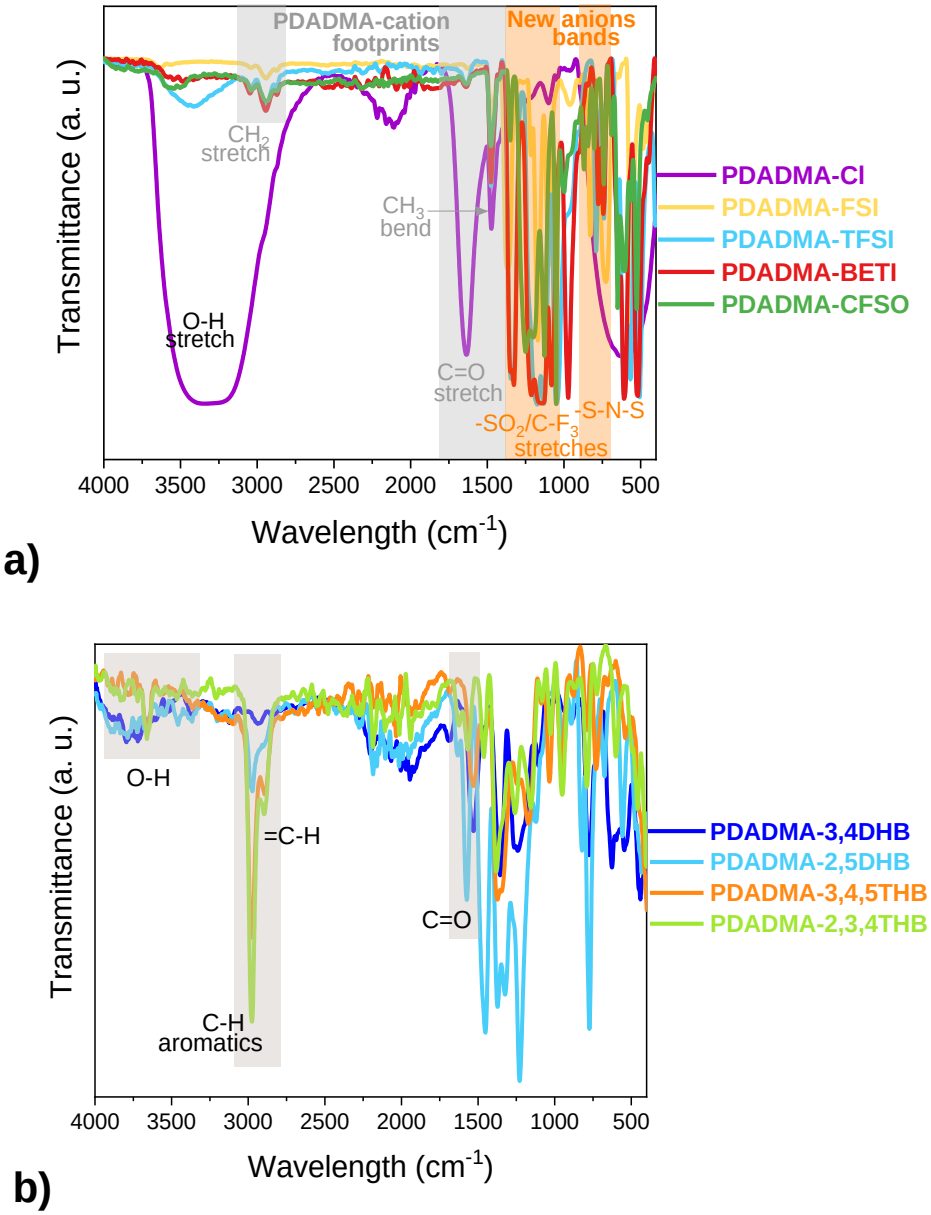

Figure 2.4. FTIR spectra a) for the fluorinated PDADMA, and b) for the PDADMA redox active PILs.

The thermal behaviour of the synthesized PDADMA PILs was investigated by thermogravimetric analysis (TGA) to determine the degradation temperature, as shown in the **Figures 2.5a** and **2.5b** for fluorinated and redox-active PDADMA PILs, respectively. PDADMA-TFSI, PDADMA-BETI and PDADMA-CFSO present high thermal stability (355, 375 and 380 ºC, respectively), while PDADMA-FSI degradation

temperature start at 230 ºC, and at 203, 274, 203 and 186 ºC for PDADMA-3,4DHB, PDADMA-2,5DHB, PDADMA-3,4,5THB, and PDADMA-2,3,4THB respectively. All of them fulfilled the requirements to be used as binders in batteries, where the expected temperature conditions could go up to 100 ºC.

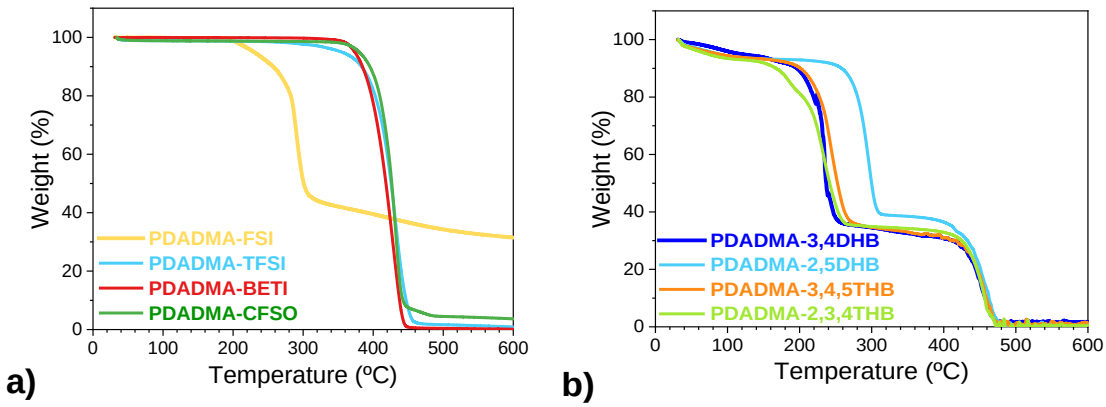

Figure 2.5. TGA curves a) of the four fluorinated PDADMA PILs, and b) of the four redox-active PDADMA PILs.

A good polymeric binder should be insoluble in the electrolyte of the battery, but soluble in adequate solvent to make a good electrode slurry and electrode film by tape casting. To verify these two conditions, the solubility of the polymers was tested in Ethyl Methyl Carbonate (EMC) and NMP which are typical solvents used for the formulation of electrolytes and preparation of slurries, respectively. The solubility of the fluorinated and redox-active PDADMA PILs is shown in **Figures 2.6a** and **2.6b** respectively, and compared to PVDF which is the most common polymeric binder in cathodes for lithium-based batteries. The four fluorinated PDADMA PILs are highly soluble (90-100%) in NMP solvent and relatively insoluble (<20%) in EMC solvent. As a comparison, we can observed that the most used polymeric binder PVDF is also 100% soluble in NMP, but presents a higher (30%) solubility in EMC compared to the fluorinated PDADMA PILs. These results confirm the promising characteristics of the fluorinated PDADMA

poly(ionic liquid)s to be used as binders. On the other hand, PDADMA redox polymers are hardly soluble in any solvent, as shown in the **Figure 2.6b** with less than 15% of solubility rate in EMC and around 20-25% only in NMP solvent. The solubility in other solvents such as isopropanol, acetone, ethanol, H_2O, Dimethylsulfoxyde (DMSO), acetonitrile, and Dimethylformamide (DMF) with sonication and heat has been tested but without success. Therefore, for the preparation of PDADMA redox PIL cathodes, a mixture of PVDF and PDADMA-DHB (1:1 wt.%) was used as binder, in order to provide a good cathode film.

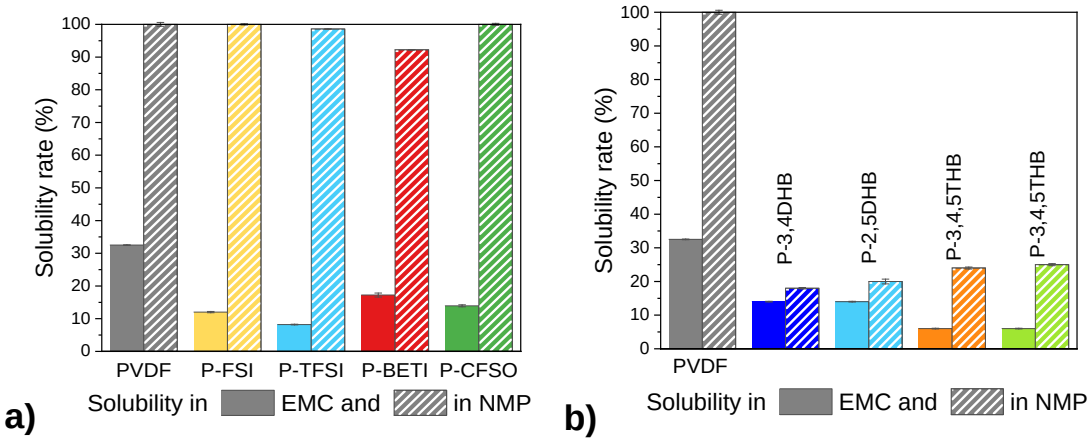

Figure 2.6. Solubility rate in EMC and NMP solvents: a) of the four fluorinated PDADMA PILs and PVDF, and b) of the four redox PDADMA PILs and PVDF.

2.4. Electrochemical characterizations of redox-active PDADMA PILs

The redox properties of PDADMA redox PILs were assessed by cyclic voltammetry (CV) measurements using the standard three-electrode configuration as shown in **Figure 2.7a**. Redox-active PILs were evaluated by coating the working electrode with a mixture of Polymer:Carbon (1:1 wt.%) and using an acidic aqueous electrolyte of 0.1 M $HClO_4$

in H_2O. **Figures 2.7b-e** show the second CV scan with the corresponding redox reaction mechanisms for each PILs.

The voltammogram in **Figure 2.7b** corresponds to PDADMA-3,4DHB electroactivity and shows well-defined peaks of oxidation at 0.72 V and reduction at 0.60 V versus Ag/AgCl, which describe a reversible redox reaction. In an acid electrolyte, the redox reaction of PDADMA-3,4DHB occurs on the catechol group which oxidizes with the loss of two electrons and two hydrogens, to form an *o*-benzoquinone . This reversible redox reaction is shown in the mechanism schema under the cyclic voltammogram (**Figure 2.7b**). The peaks are singles and reflect a simultaneous reaction on the two hydroxyl groups in positions 3 and 4. Similarly to PDADMA-3,4DHB, the two hydroxyl groups of PDADMA-2,5DHB reversibly oxidize and reduce from hydroxyquinone to *p*-benzoquinone forms (**Figure 2.7c**). Unlike PDADMA-3,4DHB, the redox reaction of PDADMA-2,5DHB occurs in two steps, showing two distinct peaks of oxidation at 0.41 and 0.63 V versus Ag/AgCl and two reductions at 0.35 and 0.60 V versus Ag/AgCl. These peaks correspond to the reaction of the two hydroxyls separately which are differentiated by distinct environments in positions 2 and 5 due to the carboxylate position. The current intensity for each couple of oxidation and reaction peaks are similar indicating a reversible process.

Regarding the PDADMA-THB PILs, the redox reaction takes place on two hydroxyl groups in *ortho* sites thanks to the geometry and electronic delocalization of benzene of the gallol function [37,38]. The oxidized forms are *o*-quinones and the reaction schemes are shown in the **Figures 2.7d** and **2.7e** for PDADMA-3,4,5THB and PDADMA-2,3,4THB respectively.

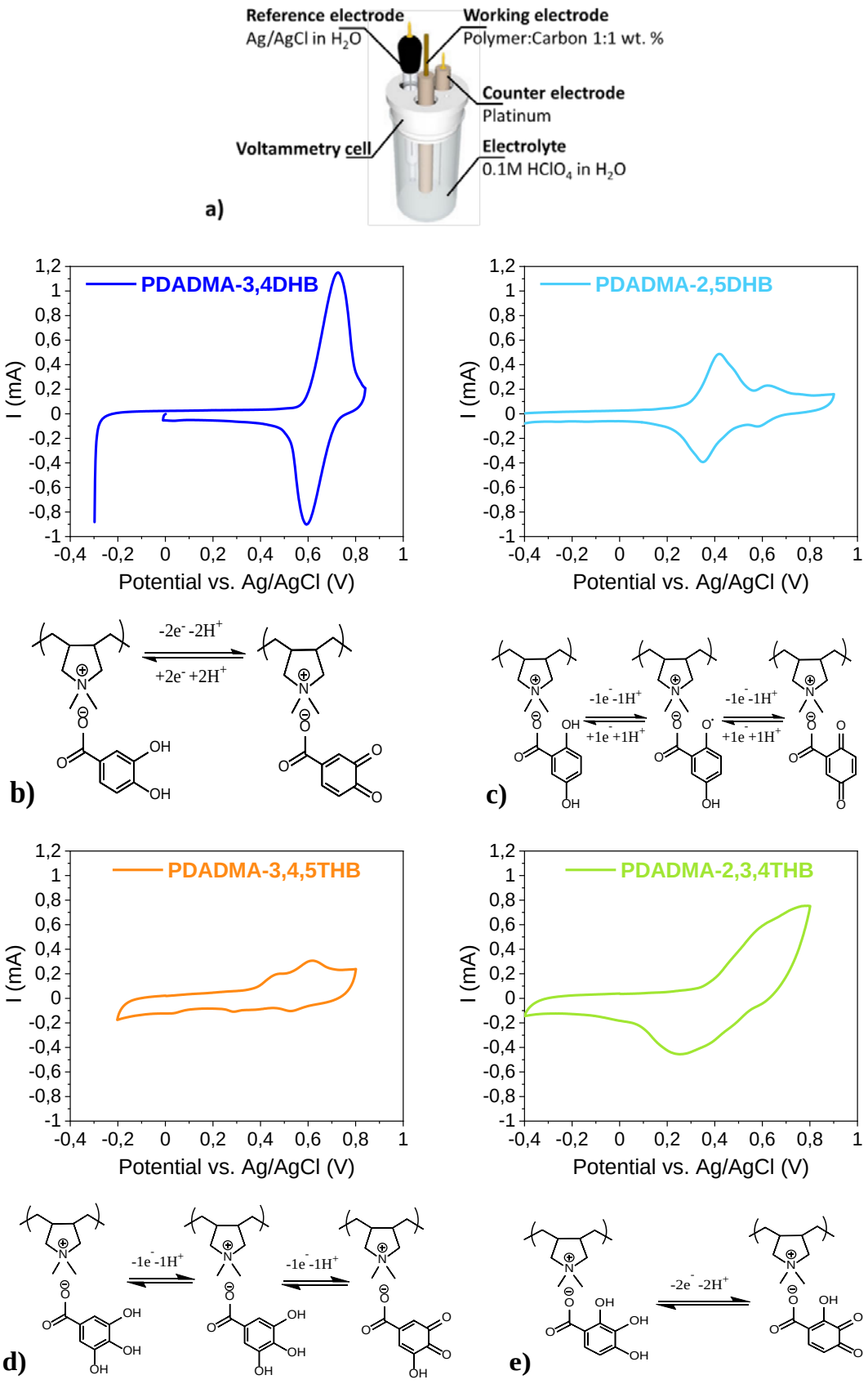

Figure 2.7. a) Schematic representation of 3 electrodes cell; The second cycle of cyclic voltammograms at 0.2 mV.s^{-1} at 25 ºC and redox mechanism for b) PDADMA-2,5-DHB; c) PDADMA-3,4DHB; d) PDADMA-3,4,5THB; and e) PDADMA-2,3,4THB.

The cyclic voltammograms of PDADMA-3,4,5THB show two oxidation peaks at 0.45 V and 0.60 V versus Ag/AgCl and two small reductions at 0.52 and 0.28 V versus Ag/AgCl, indicating low reversibility of the redox reaction. The cyclic voltammograms of PDADMA-2,3,4THB show one broad oxidation and reduction peaks at 0.70 V and 0.25 V versus Ag/AgCl, respectively. Comparing the DHB and THB PILs, we can conclude that DHB undergoes a more reversible redox reaction than THB anion, due to the similar intensity in the oxidation and reduction peaks, and the lower peak-to-peak separation between oxidation and reduction peaks. A similar behavior is reported in the literature for a comparison of PILs with catechol and pyrogallol functions [38].

Therefore, PDADMA-3,4DHB and PDADMA-2,5DHB were selected for further electrochemical characterization. Moreover, the theoretical capacity of PDADMA-3,4DHB and PDADMA-2,5DHB is 192 mA.h/g, which make them good candidates as redox active materials.

Due to the interesting redox properties of both PDADMA-DHB PILs in acidic electrolyte, they were next investigated in the presence of lithium electrolyte. LiTFSI in G4:EMC (1:2, v/v) was chosen because it is a common electrolyte for redox polymer, which showed the best results with catechol PILs in the cathode in the study of N. Patil et al. [39]. To study the redox reaction with lithium electrolyte and electrochemical stability windows (ESW) of PDADMA-DHB PILs, CV tests were performed on lithium coin cells assembled with cathodes composed of Polymer:Carbon:PVDF with a ratio of 50:30:20 wt.% as represented in **Figure 2.8a**. The voltammograms with the first two CV scans and the corresponding redox reaction mechanisms are shown in the **Figures 2.8b** and **2.8c** for PDADMA-3,4DHB and PDADMA-2,5DHB respectively.

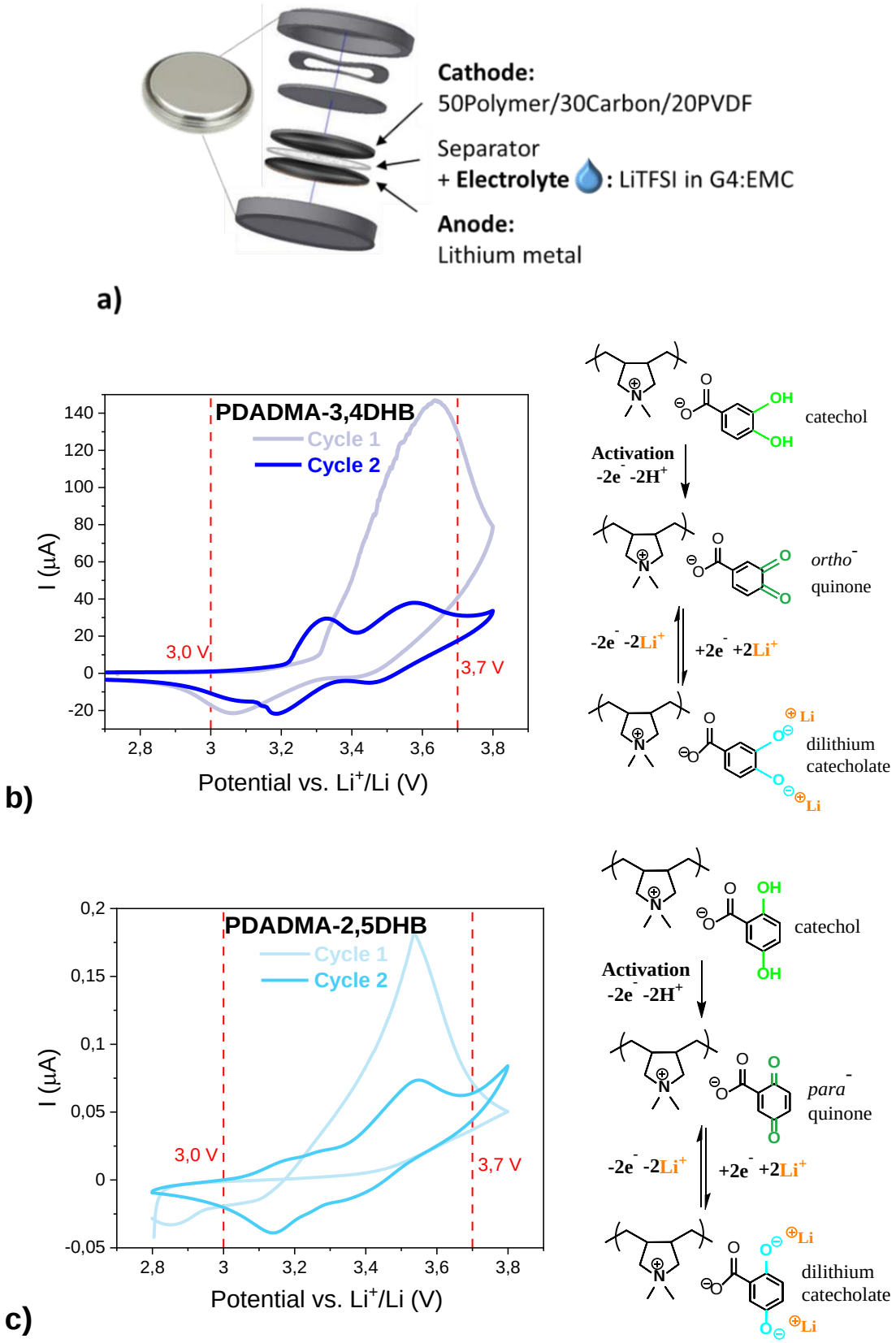

Figure 2.8. a) Schematic representation of Li || Polymer electrode battery components; Cyclic voltammograms at 0.2 mV.s^{-1} at 25 ºC (on left side) and redox mechanism (on right side) for a) PDADMA-3,4DHB; and b) PDADMA-2,5DHB.

The first cycle in the voltammogram is differentiated with an oxidation peak much higher than the others, which corresponds to the oxidation of the catechol initial to quinone stabilized by delocalization of the negative charge over the aromatic system. This reaction is called activation and takes place during the first oxidation cycle and it is also impacted by the formation of the solid electrolyte interphase (SEI) layer. In our case, the PDADMA-3,4DHB and PDADMA-2,5DHB catechols are oxidized and form *o*-quinone and *p*-quinone, respectively. Then, the second step corresponds to the reduction of (*o*- or *p*-)quinone in presence of lithium ions and provide dilithium catecholate functionalities [39]. The redox reactions between quinones and dilithium catecholates are reversible with the transfer of two-successive $1e^-/Li^+$ as it is shown in the second cycles with the two oxidation and reduction peaks. The redox peaks are well defined for PDADMA-3,4DHB at 3.32 and 3.58 V versus Li^+/Li for oxidation and at 3.19 and 3.45 V versus Li^+/Li for reduction.

2.5. Application of PDADMA PILs as binder for high voltage NMC cathodes in Li-ion batteries

The four fluorinated PDADMA (PDADMA-FSI, PDADMA-TFSI, PDADMA-BETI, PDADMA-CFSO) and the selected two redox PDADMA (PDADMA-3,4DHB and PDADMA-2,5DHB) poly(ionic liquid)s were applied as binders in high voltage NMC based cathodes and assembled in NMC || Graphite Li-ion full-cell configuration, as shown in **Figure 2.9**. The battery performances with the PDADMA-based binders were compared with the PVDF binder used as reference. The slurries were prepared by a conventional tape casting method with NMP solvent to obtain positive electrodes with 90 wt.% of NMC, 5 wt.% of carbon additive and 5 wt.% of binder. For the PDADMA-DHB

polymers, the ratio of binder was fixed to 2.5 wt.% PVDF and 2.5 wt.% PDADMA-DHB with the PVDF addition for good adhesion of the coating on the current collector.

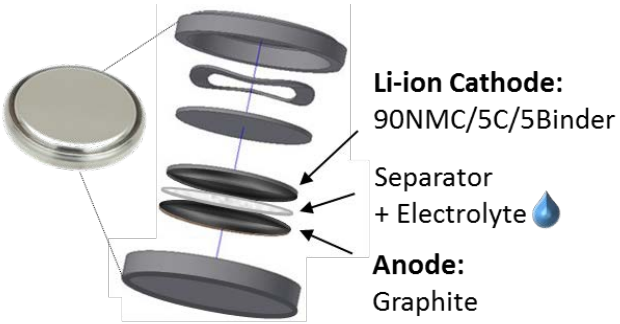

Figure 2.9. Schematic representation of components battery for application of PILs as binders in Li-ion (NMC) cathodes.

The study of the application of the PDADMA PILs as binders is presented in three parts. In the first part, the procedure of making the electrodes, the influence of the molecular weight (M_w) of the PDADMA backbone and the comparison between two electrolytes are studied in order to determine the best conditions for battery cycling. In the second part, battery performances with the four fluorinated PDADMAs as binders are discussed and compared with PVDF. And in the third part, the battery performances of PDADMA-DHB PILs as binders are reported.

2.5.1. Electrode characterization and standardization protocols

In order to validate the protocol of making electrodes, the cell performances of electrodes made in laboratory are compared to the performances obtained with a commercial electrode. The electrodes made in the laboratory respect the same thickness and density as the commercial electrode in order that these parameters do not influence performance. The comparison of cells containing PVDF binder in the cathode made in

laboratory and with commercial electrodes are shown in **Figure 2.10**. Current-voltage (IV) pulses were used to measure the internal resistance of the cells [40,41] after the first charge/discharge cycle (**Figure 2.10a**), as explained in the protocol in the experimental part (**Figures 2.28** and **2.29**). The internal resistance of the electrodes made in laboratory is slightly higher (+8%) compared to the commercial one. The rate capability of the Li-ion full-cells was assessed by galvanostatic charge-discharge experiments at increasing current densities from 0.3C to 5C at 25 ºC (**Figure 2.10b**), and the typical voltage profiles for the NMC cells was observed for cycling at 0.3C and 25 °C (**Figure 2.10c**). The capacities are slightly lower (-7% at 0.3C and 5C) for electrodes made in laboratory

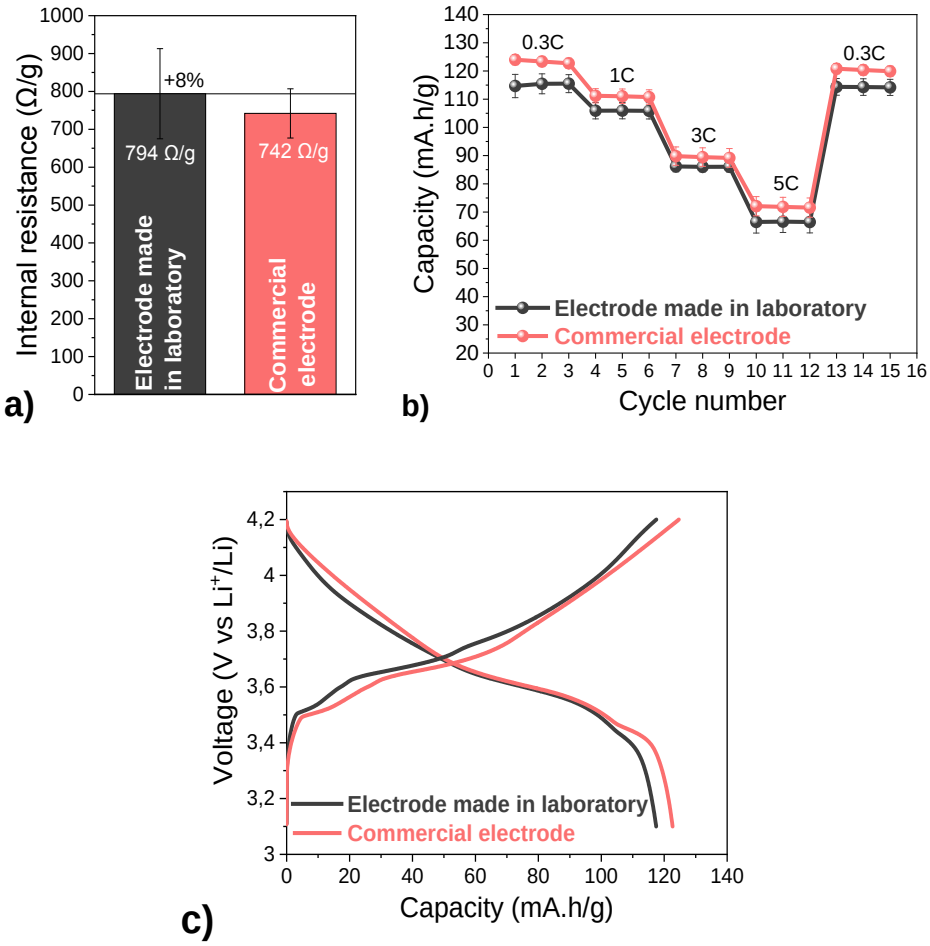

Figure 2.10. Application of PVDF as binders in Li-ion (NMC) cathodes and comparison with the commercial electrode: a) resistances of the cells measured by IV pulses; b) rate performance test at 25 °C; c) charge-discharge voltage profiles at 0.3 C rate and 25 °C.

compared to the commercial one. The cell performances with PVDF binder in the cathode are of the same order for the commercial electrodes and those making in the laboratory. The slight difference noticed can be explained by the making conditions and steps that are not automatic or in a continuous line. For example, the electrode foils were set up by hand for the drying step, or the calendaring step was made individually with the hydraulic press to obtain the similar thicknesses and densities. The importance is to compare the electrodes made in the same conditions in order to avoid variation parameters. In conclusion, the method of preparing electrodes in the laboratory is validated and this procedure will be used to make the rest of the electrodes in this chapter in order to compare electrodes making under the same conditions.

Next, the influence of the molecular weight of the polymer on the cell performances was evaluated in order to optimize the polymer binders. Usually, high molecular weight polymers have less solubility, which could possibly benefit the binder and stand better against aging. PDADMA-Cl with high (400.000-500.000 g/mol) and low (average <100.000g/mol) molecular weight were used for the synthesis of PDADMA-CFSO polymer. The cell performances with the high and low M_w PDADMA-CFSO binders in NMC || Graphite Li-ion full-cell configuration are shown in **Figure 2.11**. The measurements of current-voltage (IV) pulses after the first charge/discharge cycle (**Figure 2.11a**) show that the internal resistance was reduced to 634 Ω/g for the high M_w against 702 Ω/g for the low M_w. The impedance spectra for high and low M_w were measured and compared in Nyquist plots in **Figure 2.11b**. The resistance is 13 Ω for low M_w, and it is reduced to 10 Ω for high M_w. The rate capability test in **Figure 2.11c** shows charge capacities measured for high M_w at 0.3C rate is 125 mA.h/g and decreased by 4% for low M_w (120 mA.h/g), while at a high rate (5C) for high M_w, the capacity measured

is 83 mA.h/g and decreased by 2.5% for low M_w (81 mA.h/g). The charge-discharge voltage profile in **Figure 2.11d** shows a symmetric profile with 4% higher charge capacity for high M_w compared to low M_w. The cells with high and low M_w binders are tested with accelerating aging at 3C and 25ºC and the results are shown in **Figure 2.11e**. The capacity measurements of 1000 cycles allow for comparing the stability of binders over time. The capacity is 10% decreased for the binder with low M_w during the first 500 cycles. Then between cycles 500 and 1000, the capacity gap increases, with a larger capacity decrease for the binder with low M_w. At cycle 1000, the capacity of low M_w

binder is 22% decreased compared to high M_w.In conclusion, the high M_w PDADMA-CFSO binder exhibits improved cell stability over time as well as cell performances with 11% reduced resistance, and 4% increased capacity compared to the low M_w PDADMA-CFSO. Further in the chapter, only high M_w PDADMA based polymers are discussed.

Regarding the electrolyte, the two electrolyte salts 1.0 M $LiPF_6$ and 1.0 M LiTFSI in EC:DMC have been tested with PDADMA-TFSI binder for the cathode in NMC || Graphite Li-ion full-cell configuration. Among all conducting salt, $LiPF_6$ remains the only candidate to be used in the majority of commercial lithium-ion batteries, due to its

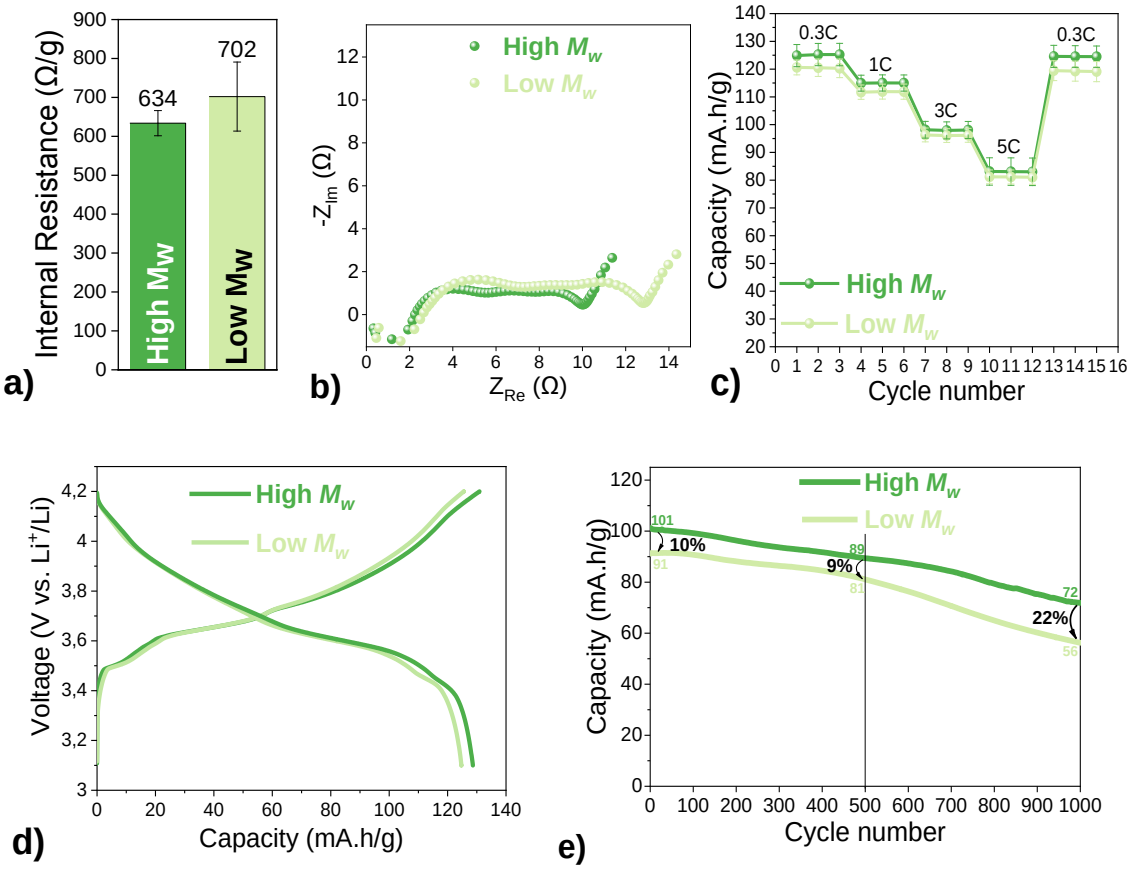

Figure 2.11. Comparison of PDADMA-CFSO with high and low M_w as binder in Li-ion cathodes: a) resistances of the cells measured by IV pulses; b) resistances of the cells measured by EIS; c) rate performance test at 25 °C; d) charge-discharge voltage profiles at 0.3C rate and 25 ºC; and e) accelerating aging at 3C and 25 °C for 1000 cycles.

well-balanced properties, such as high ionic conductivity, good electrochemical stability, effective aluminum current collector passivation, and effective SEI formation on highly graphitic anodes [42]. While LiTFSI is reported as a good alternative to $LiPF_6$ due to the improvement of the chemical and thermal stability as salt for electrolyte [43,44]. The goal is to test if the association of the same counter anion for electrolyte salt and binder, which is -TFSI in this case, can improve the battery performance as reported by An Ha et al.[45] in a study for sodium-oxygen battery.

Figure 2.12a presents the internal resistance results for the electrolyte salts $LiPF_6$ and LiTFSI with values of 484 and 740 Ω/g respectively. In other words, the internal resistance was increased by 35% with the use of a binder and an electrolyte composed of the same counter anion, i.e. TFSI. Figure 2.12b shows charge-discharge voltage profiles for the salt electrolytes $LiPF_6$ and LiTFSI with charge capacities of 123 and 114 mA.h/g, respectively. The charge capacity was reduced by 7% with the salt electrolyte LiTFSI compared to the $LiPF_6$ salt electrolyte. In addition, the charge-discharge voltage profile for LiTFSI electrolyte is asymmetrical, the discharge capacity lost 16% compared to the charge capacity. The electrodes with the PDADMA-TFSI binder were immersed in the two electrolytes and the pictures of this test are shown in Figure 2.12c and d for the salt electrolytes $LiPF_6$ and LiTFSI respectively. The coating with the PDADMA-TFSI binder was completely dissolved in salt electrolyte LiTFSI, unlike in $LiPF_6$, as clearly shown in the pictures. In conclusion, higher internal resistance and lower capacity were measured for electrolyte with LiTFSI salt, which had the same counter anion to the binder and this

is due to the electrode which dissolves in the electrolyte. Therefore, $LiPF_6$ salt electrolyte is further used in the discussion for studies with PDADMA-based binders.

2.5.2. Fluorinated PDADMA PILs

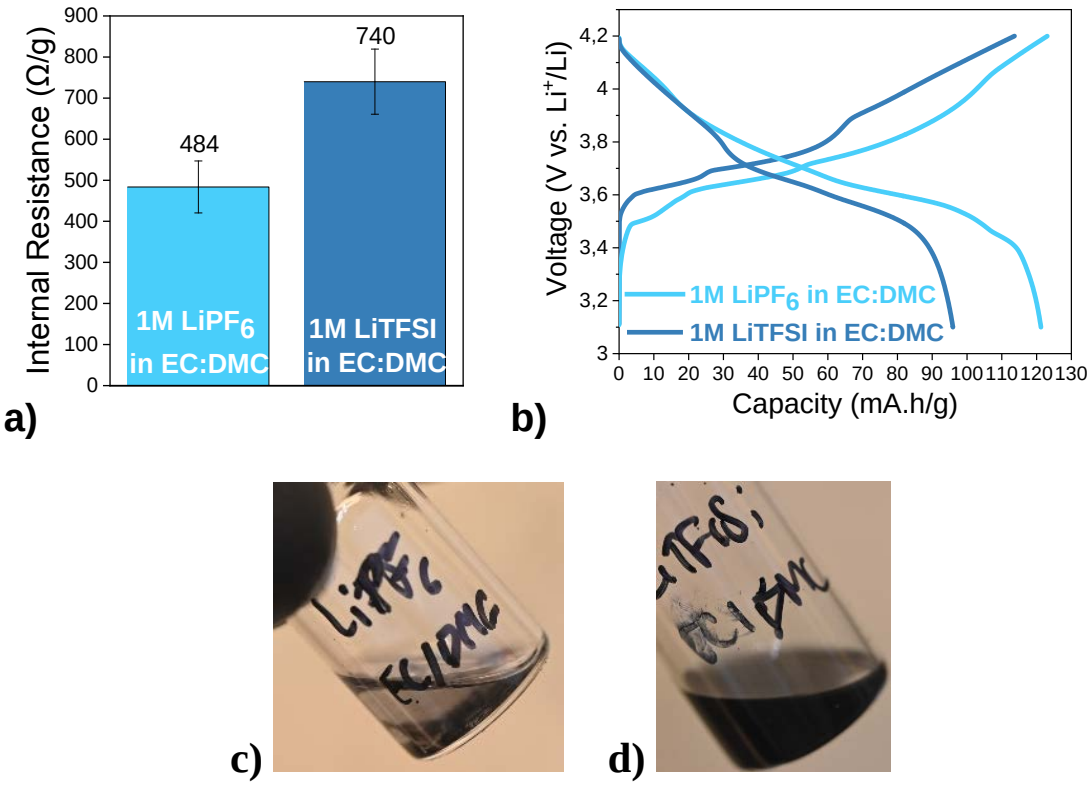

Figure 2.12. Application of PDADMA-TFSI as binder in Li-ion cathodes with different electrolyte salts: 1.0 M $LiPF_6$ and 1.0 M LiTFSI in EC:DMC: a) resistances of the cells measured by IV pulses; b) charge-discharge voltage profiles at 0.3C rate and 25 ºC. Pictures of electrodes with PDADMA-TFSI binder c) in salt electrolyte $LiPF_6$; and d) in salt electrolyte LiTFSI.

In this part, the four fluorinated PDADMA polymers are discussed as a binder in NMC || Graphite Li-ion full-cell and compared to PVDF as a reference, and the cell performances are shown in **Figure 2.13**. The internal resistance of the cells measured by IV pulses after the first charge/discharge cycle is shown in **Figure 2.13a**. It can be observed that PDADMA-based binders decreased the measured resistance values by at least 20% compared to PVDF. The lowest resistance value was measured for PDADMA-

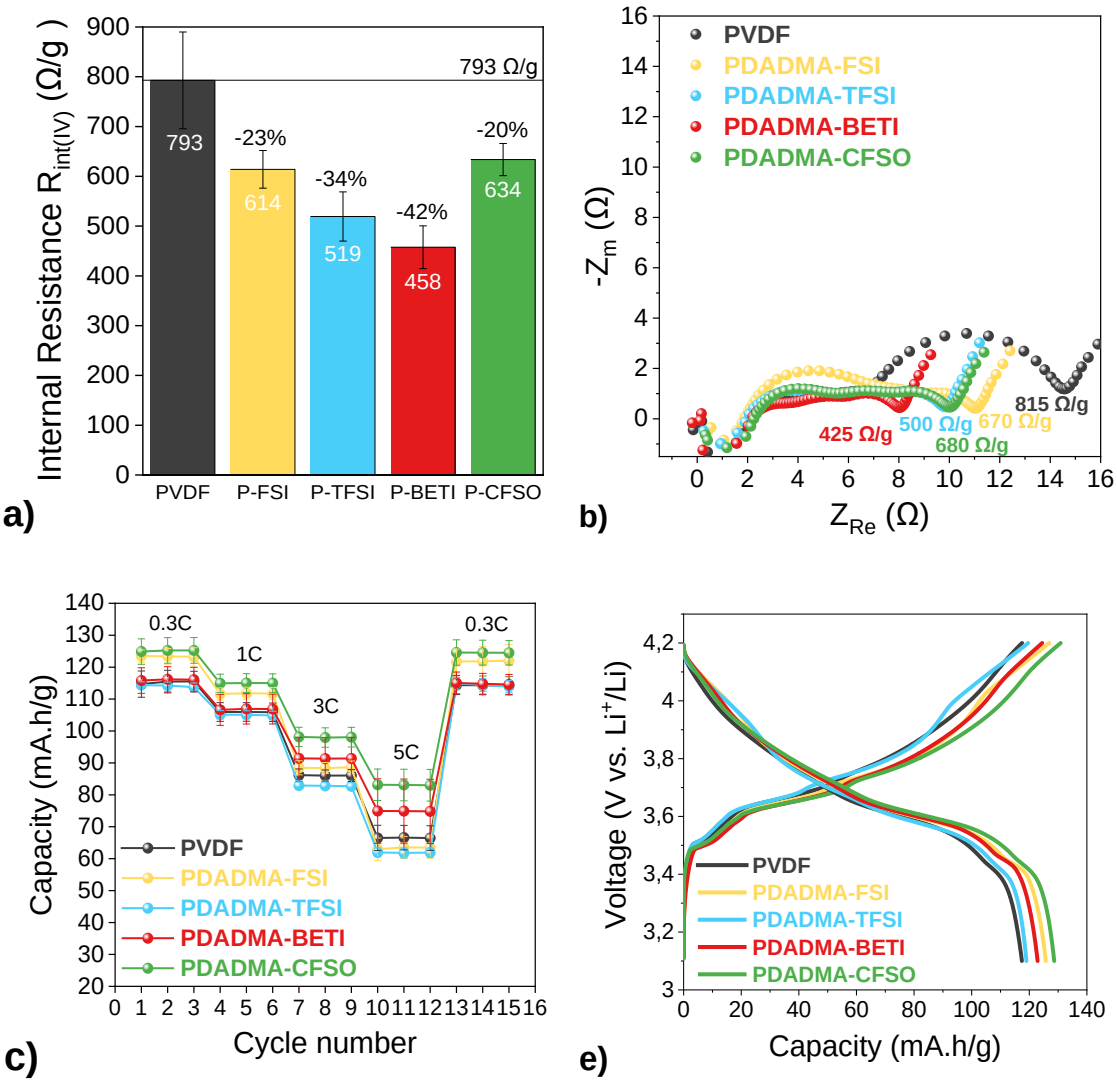

Figure 2.13. Application of PILs as binders in Li-ion (NMC) cathodes: a) resistances of the cells measured by IV pulses; b) resistances of the cells measured by EIS; c) rate performance test at 25 °C; d) charge-discharge voltage profiles at 0.3 C rate and 25 °C.

BETI with 458 Ω/g (42% less than PVDF), which could be related to a higher proportion of fluorine groups in the polymer.

Electrochemical Impedance Spectroscopy (EIS) was also implemented to elucidate the different phenomena present in the cells, as well as the magnitude of their contributions to the total cell impedance (**Figure 2.13b**). The impedance spectra were analyzed using an equivalent electrical circuit (EEC) model presented in **Figure 2.14a** which was adapted from literature [46,47]. The EEC describes the transfer function of the electrochemical process in terms of electrical circuit elements: resistance (***R***) and Constant Phase Element (***CPE***) in our case. All the impedance spectra fittings obtained with the proposed EEC are presented in **Figures 2.14b-f** and the fitting parameters are reported in detail in **Table 2.1** with the ideal capacitors ***C*** calculated from ***CPE*** values. The electrical elements model, the behavior of coupled processes, and the time constants represent the time response, relaxation, delay, or manifestation of the phenomena that are associated with resistance, charge storage, or diffusion that occur in the composite of batteries. According to the interpretation of the EEC model proposed by Suarez et al. [47] for the description of composite electrodes for LIBs, the time constants ($\boldsymbol{\tau}$) were calculated and the values are presented in **Table 2.2**. The comparison of the same parameters (***R***, ***C***, or $\boldsymbol{\tau}$) for the different binders is interesting to highlight the contributions linked to the binder influence in cathode since it is the only variable between these cells. Based on the literature, the different contributions of the existing processes in the cells were identified in the Nyquist plots, and explained according to their rate of appearance in the impedance spectra. Thus, three regions were classified: high, medium, and low-frequencies.

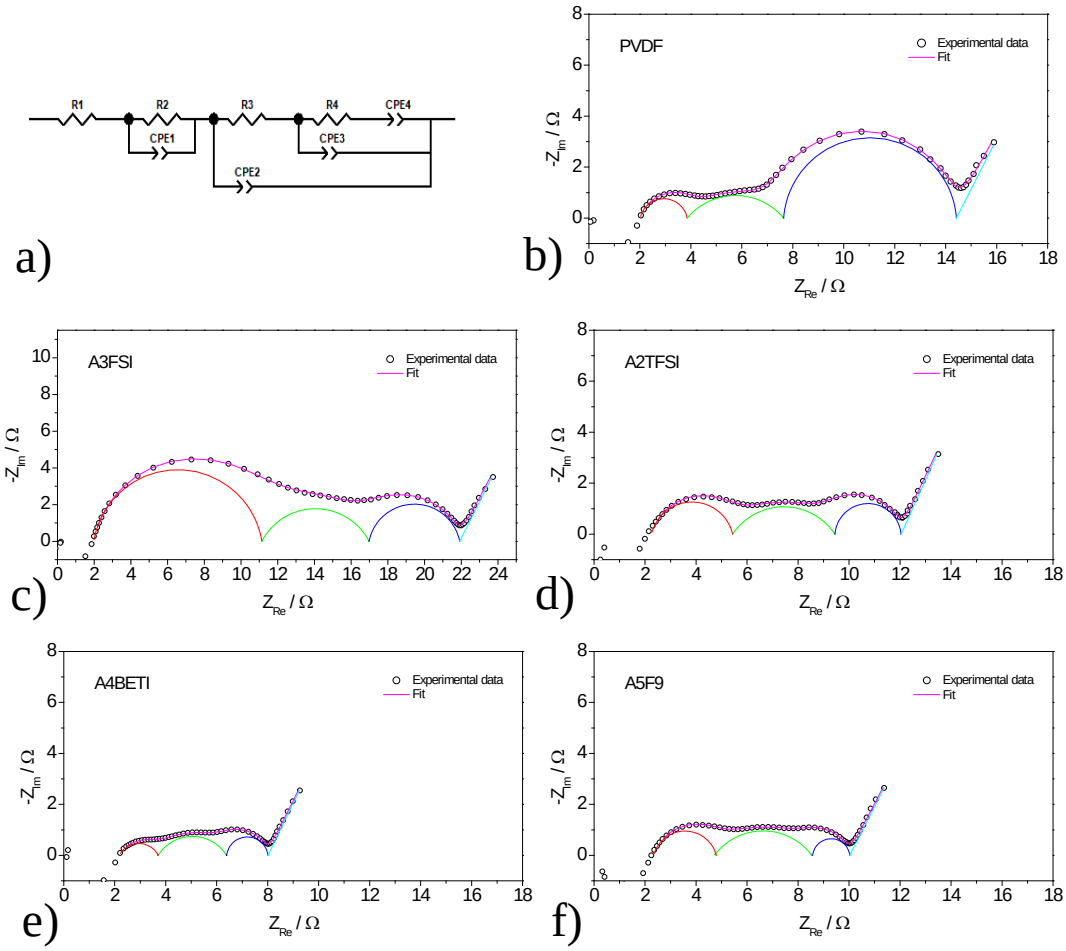

Figure 2.14. a) Equivalent circuit used for fitting; and the curves of the Nyquist plots and the fitting corresponding for b) PVDF; c) PDADMA-FSI; d) PDADMA-TFSI; e) PDADMA-BETI; and f) PDADMA-CFSO.

First, in the high-frequency region, an inductive behavior related to the instrumental artifact and the wiring between the electrodes with the measuring equipment and the electrolyte resistance $\boldsymbol{R_1} \approx 2\ \Omega$ is identified for all binders. The next elements in the EEC model are associated with the anode and cathode polarization losses for contact, SEI, and charge transfer, which correspond to the following semi-circles [48].

The $\boldsymbol{R_2}$ and $\boldsymbol{C_1}$ elements (identified as $\boldsymbol{\tau_1}$) are associated to contact resistance between particles of active material in the composite. The $\boldsymbol{R_2}$ values give an indication of the level of compactness and homogeneity of the electrodes. In our case, the values of

$\boldsymbol{R_2}$ and $\boldsymbol{C_1}$ for the different binders are maintained relatively similar, except for PDADMA-FSI binder. Indeed, the values of $\boldsymbol{R_2}$ are between 2.6 and 3.8 Ω (**Table 2.1**), but 8.01 Ω for PDADMA-FSI binder, in other words, more than double that of the others. The high $\boldsymbol{R_2}$ value for PDADMA-FSI binder reflects the binder contributions to the formation of highly compact composites as it is observed in the Scanning Electron Microscopy (SEM) images (**Figure 16d** for PDADMA-FSI) and discussed later. This compact composition can even limit the ionic transport, which is translated by high values of capacitance $\boldsymbol{C_1}$ and time constant $\boldsymbol{\tau_1}$.

Then, in the medium-frequency region, the charge transfer phenomena are predominant and described by $\boldsymbol{\tau_2}$ time constant. Between the different binders tested in our case, there is no great variation in the values of $\boldsymbol{\tau_2}$. PVDF and PDADMA-BETI binders have the fastest time constants, while PDADMA-CFSO and PDADMA-FSI have intermediate time constants, and PDADMA-TFSI showed the slower time constant.

To end, in the low-frequency region, the diffusional phenomena that control the reactivity of the active material particles are predominant and represented by the semi-circles in the Nyquist plots in **Figure 2.14b**. The resistance contribution $\boldsymbol{R_4}$ and the capacitance $\boldsymbol{C_3}$ were related to the binder influence in the cathode lithiation process, which is the transport of Li-ion from the binder to active material particles [47]. As indicated in **Table 2.1**, $\boldsymbol{R_4}$ is equal to 6.78 Ω for the cell with PVDF binder, while it was around 2 Ω for the cells with PDADMA binders. This result is corroborated with the results obtained in the IV pulse technique and highlights the improvement of the Li-ion transport through the cathodes with PDADMA-based binders with a reduction in the resistance of the cell compared to PVDF. In addition to the highest resistance value, $\boldsymbol{R_4}$, the electrodes

with PVDF present also a high value of capacitance to the lithiation process (***C₃***), which denotes the high accumulation of lithium ions on the surface of the active material particles. The consequence of this accumulation is the limitation of Li^+ amount on the surface of the active material particles, therefore the Li^+ amount available for the intercalation process within the active material particles is limited despite their high availability of energetically favorable spaces (***C₄***) for the reaction process. The time constants $\boldsymbol{\tau_3}$ and $\boldsymbol{\tau_4}$ corresponding to the diffusion and reaction processes in electrodes (**Table 2.2**), have the shortest times for PDADMA-BETI and PDADMA-CFSO binders, significantly shorter than the electrodes with PVDF.

Table 2.1. Resistances from Impedance (EIS) fitting. R(Ω) andC (F).

Binder	R_1	R_2	R_3	R_4	C_1	C_2	C_3	C_4
PVDF	2.02	3.79	1.84	6.78	5.24×10^{-4}	6.74×10^{-6}	4.02×10^{-2}	1.56×10^{-1}
PDADMA-FSI	2.25	8.01	3.18	2.59	6.14×10^{-4}	9.81×10^{-6}	2.05×10^{-2}	3.66×10^{0}
PDADMA-TFSI	2.00	3.07	3.78	2.23	2.26×10^{-4}	1.36×10^{-5}	8.02×10^{-3}	3.55×10^{0}
PDADMA-BETI	2.18	2.69	1.52	1.62	6.60×10^{-4}	$8.26.\times10^{-6}$	1.52×10^{-2}	2.43×10^{0}
PDADMA-CFSO	2.34	3,78	2.45	1.45	5.46×10^{-4}	9.57×10^{-6}	1.28×10^{-2}	1.91×10^{0}

Table 2.2. Analysis of time constants $\boldsymbol{\tau}$ ($\boldsymbol{s}$) associated with the equivalent circuit model.

Binder	$\tau_1 = R_2 \times C_1$	$\tau_2 = R_3 \times C_2$	$\tau_3 = R_4 \times C_3$	$\tau_4 = R_4 \times C_4$
PVDF	2.0×10^{-3}	1.24×10^{-5}	2.7×10^{-1}	1.1×10^{-2}
PDADMA-FSI	2.5×10^{-3}	3.12×10^{-5}	5.3×10^{-2}	9.5×10^{0}
PDADMA-TFSI	6.9×10^{-3}	5.14×10^{-5}	1.8×10^{-2}	7.9×10^{0}
PDADMA-BETI	1.8×10^{-3}	1.26×10^{-5}	2.5×10^{-2}	3.9×10^{0}
PDADMA-CFSO	2.1×10^{-3}	2.35×10^{-5}	1.9×10^{-5}	2.8×10^{0}

In general, all the PIL binders developed in this work seem to favor the ionic transport and Li^+ intercalation processes. This fact is more evident in the electrodes prepared with PDADMA-BETI and PDADMA-CFSO binders, for which the size and structural conformation of the mobile anion are known to promote the delocalization of its charge generating the resonance effect and facilitates the ionic and electronic transport in the electrode composites.

The resistance values $\boldsymbol{R_1}$, $\boldsymbol{R_2}$, $\boldsymbol{R_3}$, and $\boldsymbol{R_4}$ are added together to calculate the internal resistance [41] of the batteries called $\mathbf{R_{int(EIS)}}$. $\mathbf{R_{int(EIS)}}$ is compared in **Table 2.3** with the internal resistance values calculated by IV pulse method, called $\mathbf{R_{int(IV)}}$. For each binder, $\mathbf{R_{int(EIS)}}$ and $\mathbf{R_{int(IV)}}$ values are in the same range. This made it possible to contrast the results obtained with the IV pulse technique and to validate the correlation between the two techniques.

Table 2.3. Resistances calculated by EIS and IV methods.

Binder	EIS method: $R_{int(EIS)}$ (Ω/g)	IV method: $R_{int(IV)}$ (Ω/g)
PVDF	815	793
PDADMA-FSI	670	614
PDADMA-TFSI	500	519
PDADMA-BETI	425	458
PDADMA-CFSO	680	634

The rate capability of the Li-ion full-cells was assessed by galvanostatic charge-discharge experiments at increasing current densities and 25 ºC (**Figure 2.13c**). At low

current density of 0.3 C, full-cells were able to deliver 125, 123, 116, 114, and 115 $mA.h.g^{-1}$ with PDADMA-CFSO, PDADMA-FSI, PDADMA-BETI, PDADMA-TFSI and PVDF, respectively. A consistent capacity reduction was observed for all cells with the gradual current increase from 0.3C to 5C along with the capacity recovery upon the switch of the current back to 0.3C. It can be observed that cells with PDADMA-CFSO and PDADMA-FSI binders delivered higher capacity values than cells with PVDF. At higher currents (3C and 5C), the capacity of the cell with PDADMA-FSI dropped below the one observed with PVDF, while cells with PDADMA-CFSO and PDADMA-BETI binders performed better than the one with PVDF. It is worth mentioning, that cells with PDADMA-CFSO binder obtained higher capacity values than the ones with PVDF at all applied current densities. Remarkably, the capacity increase with PDADMA-CFSO binder was of 9% at 0.3 C and 26% at 5C when compared to standard PVDF binder.

Typical voltage profiles for the NMC cells cycling at 0.3C and 25 °C are shown in **Figure 2.13d**. The similarity in the charge/discharge profiles of the cells at a low state of charge (SoC) suggests that all cells had similar activation overpotentials; however, at high SoC values, the cells with PDADMA-based binders showed lower overpotentials as a result of the enhanced diffusion of Li-ion through them, respect to the cell with PVDF. As a consequence, the charge capacity obtained for the cell using PVDF was 117 $mA.h.g^{-1}$, while the ones for the four PDADMA-based binders showed higher capacities, 130 $mA.h.g^{-1}$ for the best performing PDADMA-CFSO.

To further study the cycling performance, accelerating aging experiments were carried out at 50 °C. The results for 500 cycles applying 3C are presented in **Figure 2.15a**. It is observed that the capacity loss was slower for the cells using PDADMA-based

binders than for PVDF-based cells, except for the one using PDADMA-FSI, which were not stable at these conditions. After 500 cycles at 3C and 50 °C, the capacity of cell with PVDF decreased by 30%, while for the ones with PDADMA-CFSO and PDADMA-BETI capacity loss was only 9% and 12%, respectively. Additional accelerating aging experiments were performed at 25 °C applying 1C and 3C, as shown in **Figures 2.15b** and **2.15c** respectively, and confirmed that PDADMA-CFSO and PDADMA-BETI binders improved the stability of the battery compared to PVDF reference binder. Note the impressive result after 1000 cycles at 3C and 25 °C (**Figure 2.15c**), the capacity of the cell with PDADMA-BETI decreased by less than 20%, while almost 40% loss was observed for the cell with PVDF binder. In conclusion, PDADMA-BETI and specially PDADMA-CFSO binders improved by 9-26% the discharge capacity values of NMC || graphite cells at different current densities and the cycling stability in accelerating aging

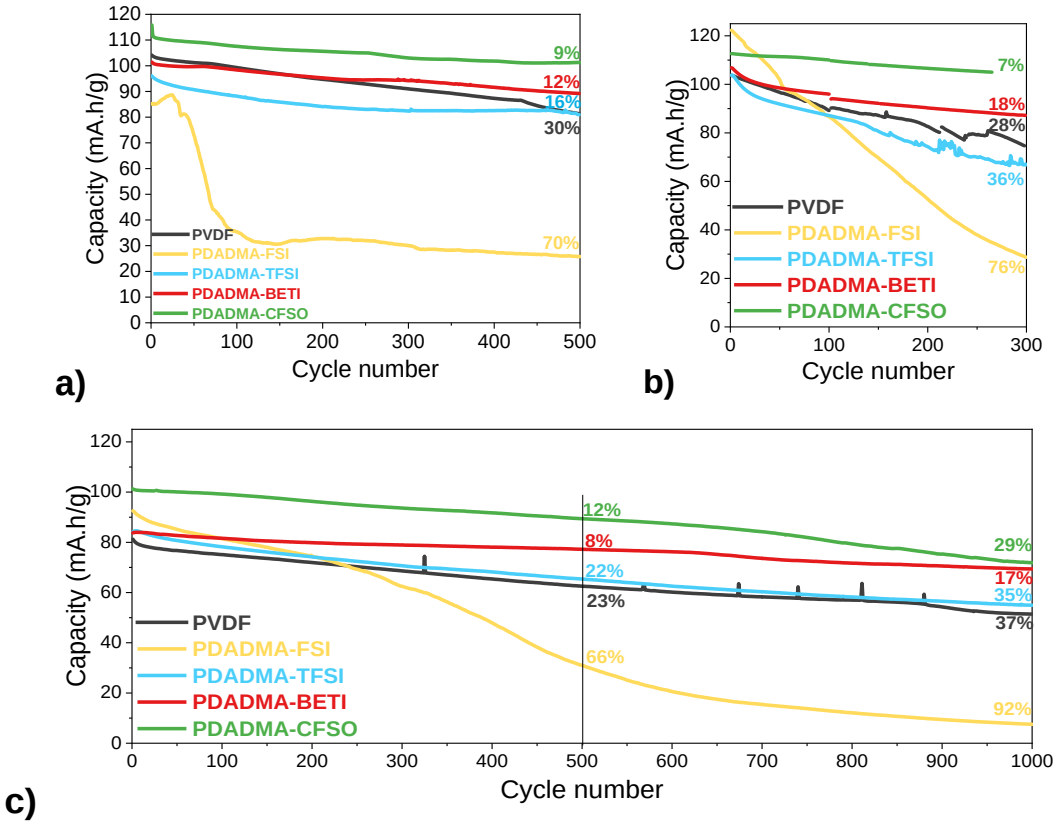

Figure 2.15. Accelerating aging: a) 500 cycles at 3C rate and 50 °C; b) 300 cycles at 1C and 25 °C; and c) 1000 cycles at 3C and 25 °C.

conditions, which demonstrate the applicability of these polymers as binder in cathodes for Li-ion batteries.

In order to assess the effect of each binder on the durability of the Li-ion batteries, impedance spectra were acquired before and after cycling at 3C rate and 25 °C (cycling data shown in **Figure 2.15c**). The impedance spectra obtained before and after cycling for the Li-ion cells containing the different binders are shown in typical Nyquist plots representation (**Figure 2.16a**). As observed, the total cell impedance increased after cycling in all the cases, especially for the cell with PDADMA-TFSI that had a larger

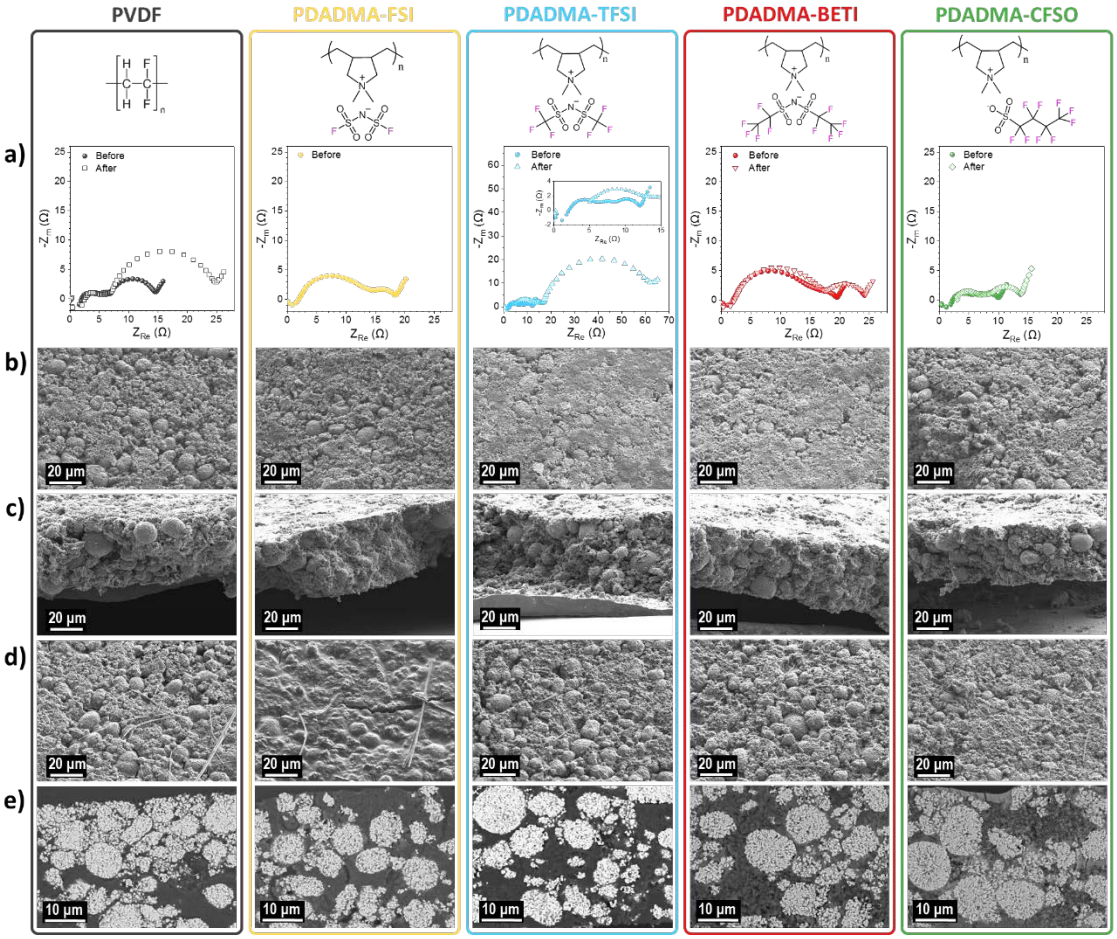

Figure 2.16. a) Nyquist plots of Li-ion cells with the different binders and their structure before and after cycling at 3C rate and 25 °C for 1000 cycles; and SEM images of b) cathode surfaces before cycling; c) cathode cross-section before cycling; d) cathode surfaces after cycling; and e) BSE images of the cross-section after cycling.

charge transfer resistance. In the case of PDADMA-BETI and PDADMA-CFSO binders that have large electronic delocalization in the anions as consequence of the increase of fluorine atoms in their anion structure, the transport of Li-ion was facilitated and thus, the charge transference resistance values after cycling were smaller than PDADMA-TFSI. On the other hand, it was not possible to obtain the impedance spectrum for cell with PDADMA-FSI because it was not stable over time in the accelerated aging tests (**Figure 2.15c**).

The distribution of relaxation times (DRT) method was also used to support the impedance study before and after cycling, and to identify which part of the battery the evolution in impedance comes from. The DRT curves for cycles 1 and 1000 are shown in **Figures 2.17a** and **b** respectively. In addition, comparisons of the DRT curves for cycles 1 and 1000 for each binder are presented in **Figures 2.17c-f** to evaluate the impedance evolution over time. Two main time regions are distinguished and discussed: between 10^{-4} and 10^{-5} s, which indicates the cell contact loss; and between 10^{-2} and 10^{-1} s, which represents the charge transfer loss [50]. In the region between 10^{-2} and 10^{-1} s, the impedance peaks of cells with PVDF and PDADMA-TFSI show a significant evolution between 1 and 1000 cycles compared to the evolution with other binders. This identifies the loss of contact as one of the major reasons for the increases in impedance for PVDF and PDADMA-TFSI (which was observed in **Figure 2.16a**). In the region between 10^{-4} and 10^{-5} s, the impedance peaks of cells with PDADMA-TFSI and PDADMA-BETI show a slightly higher evolution than for the other binders. This indicates that charge transfer loss is the main cause of the impedance increase for these polymers.These results correlate with the conclusion already observed previously, which is that the use of anions with high fluorine content favors the mobility of Li-ion in the electrodes. Thus, cells containing

PDADMA-BETI and PDADMA-CFSO binders exhibited good stability, unlike PDADMA-TFSI or PVDF.

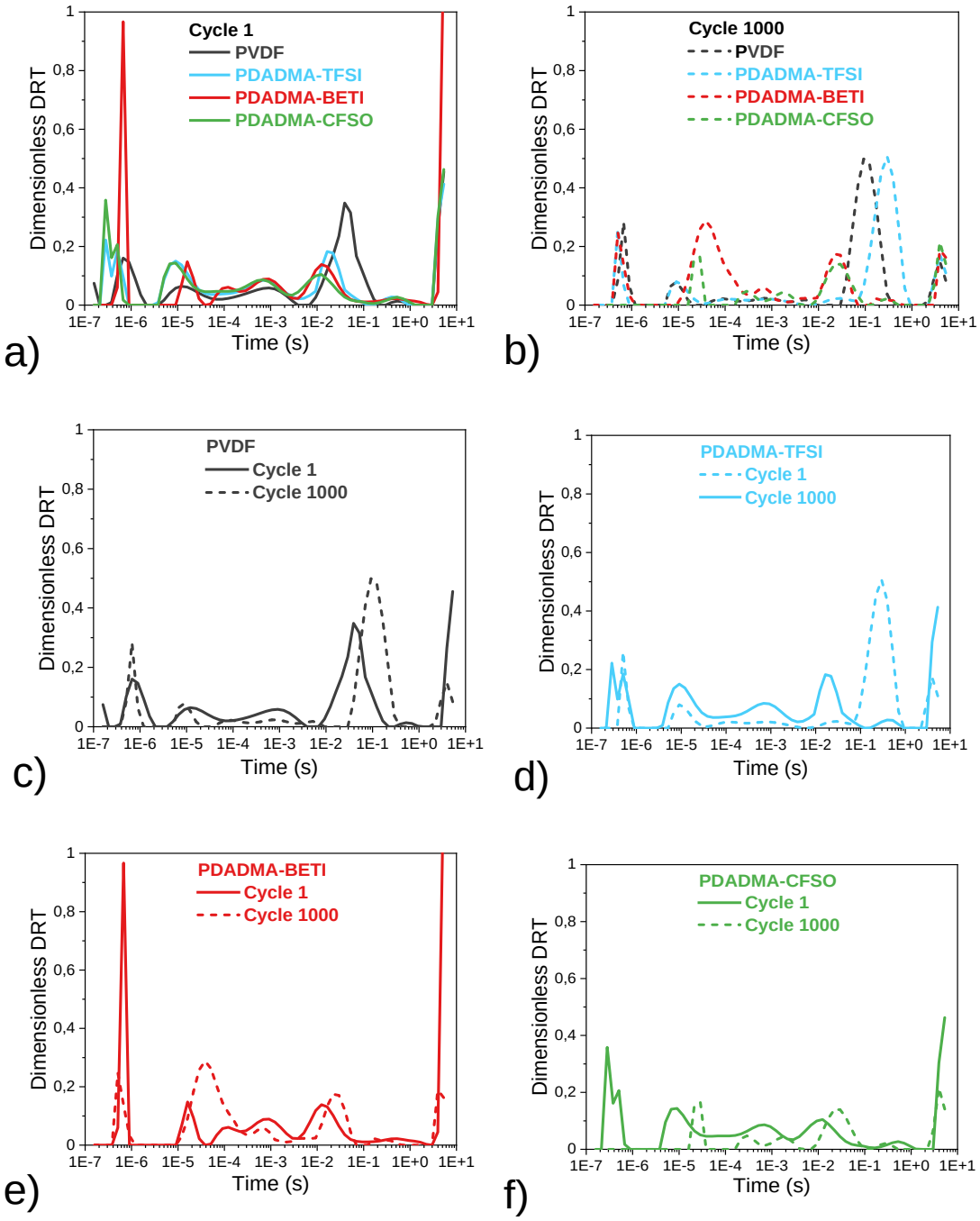

Figure 2.17. DRT results at 3C rate and 25 °C of the different binders a) at cycle 1, and b) at cycle 1000. DRT results at 3C rate and 25 °C for cycle 1 and 1000 for c) PVDF; d) PDADMA-TFSI; e) PDADMA-BETI; and f) PDADMA-CFSO.

The morphology and microenvironment of the positive electrodes before and after cycling at 3C rate and 25 °C was studied by SEM in order to understand the effect of the binder on the structure of cathodes and their cycling stability. The SEM images of the surfaces of the cathodes before cycling are shown in **Figure 2.16b** and the cross-sections in **Figure 2.16c**. As observed, the NMC particles were evenly distributed over the surface and bulk of the electrode. This distribution was confirmed by the contrast in backscattered electron (BSE) images for electrodes embedded and cross-sectioned in **Figure 2.18**. The bright particles corresponded to NMC, while the darker parts corresponded to carbon and binder additives.

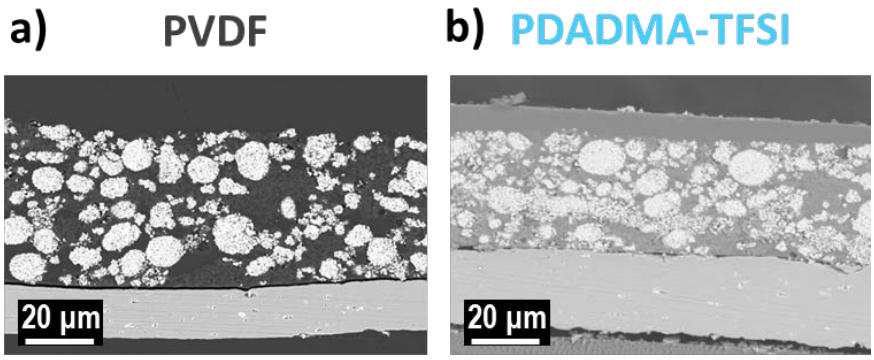

Figure 2.18. NMC electrode analysis by BSE images of samples before cycling embedded and cross-sectioned using an ultra-microtome and diamond knife.

After cycling, the SEM images showed (**Figures 2.16d-e**) coarser electrode surfaces, where the shape of NMC particles were distinguished. The visible threads corresponded to glass fiber traces after disassembling the cells. The biggest differences in the surfaces before and after cycling were observed on electrodes with PDADMA-FSI binder, indicating a less stable electrode structure, which could be the reason for the capacity fading observed in the cycling of **Figure 2.15**. On the cross-section images, no visible differences were found within PDADMA-based binders, as well as before and after cycling. However, PVDF clearly showed a difference in particle dispersion. Before

cycling (**Figure 2.18**) NMC particles were homogeneously distributed and surrounded by carbon and binder, while after cycling (**Figure 2.16e**) NMC particles were found compacted on the top of the electrode, lacking of carbon/binder covering, hindering the ion and electron conductivity. The capacity loss measured for PVDF after cycling was probably induced by this degradation of the electrode structure. It can be hypothesized that the use of a binder with ionic conductive properties, like PDADMA-based binders, contributes to the improvement of ion conduction through the electrode and thus helps in the performance of the cell and in maintaining the integrity of the electrode during cycling[45].

2.5.3. Redox-active PDADMA PILs

In this part, the two polymers PDADMA-3,4DHB and PDADMA-2,5DHB were tested as binders in cathode in NMC || Graphite Li-ion full-cell and their cell performances compared with PVDF are shown in **Figure 2.19**. The IV pulses after the first charge/discharge cycle allowed to calculate the internal resistance of the cells and the values are shown in **Figure 2.19a**. The internal resistance is 1221 and 1344 Ω/g for PDADMA-3.4DHB and PDADMA-2.5DHB respectively, while it is 745 Ω/g for PVDF binder. In other words, the internal resistance is much higher for PDADMA-DHB binders, increased by 64% and 80% for PDADMA-3.4DHB and PDADMA-2.5DHB respectively.

Figure 2.19b shows the results of the galvanostatic charge-discharge experiment at increasing current densities and 25 ºC. In the first three cycles at a low current density of 0.3C, full cells were able to deliver a stable average of 115, 110, and 108 $mAh.g^{-1}$ with PVDF, PDADMA-3.4DHB, and PDADMA-2.5DHB binders respectively. In general, the

capacity decreases with increasing applied current and the decrease of capacity was observed greater for PDADMDA-DHB and particularly for PDADMA-2.5DHB. Indeed, at the initial cycles of 0.3C rate, the capacities were reduced by 4% and 6% for PDADMA-3,4DHB, and PDADMA-2,5DHB respectively compared to PVDF; whereas at 5C rate, the capacities were reduced by 18% and 25% for PDADMA-3,4DHB, and PDADMA-2,5DHB respectively compared to PVDF at 5C rate. Moreover, the capacity for PDADMA-2,5DHB was reduced by 6.5% compared to its initial value on the switch from the current back to 0.3C after cycles at high C rate, while the capacities for PVDF and PDADMA-3,4DHB were recovered their values. In addition, the stability difficulties for PDADMA-2.5DHB binders were marked by error bars, which increased progressively, especially at high current.

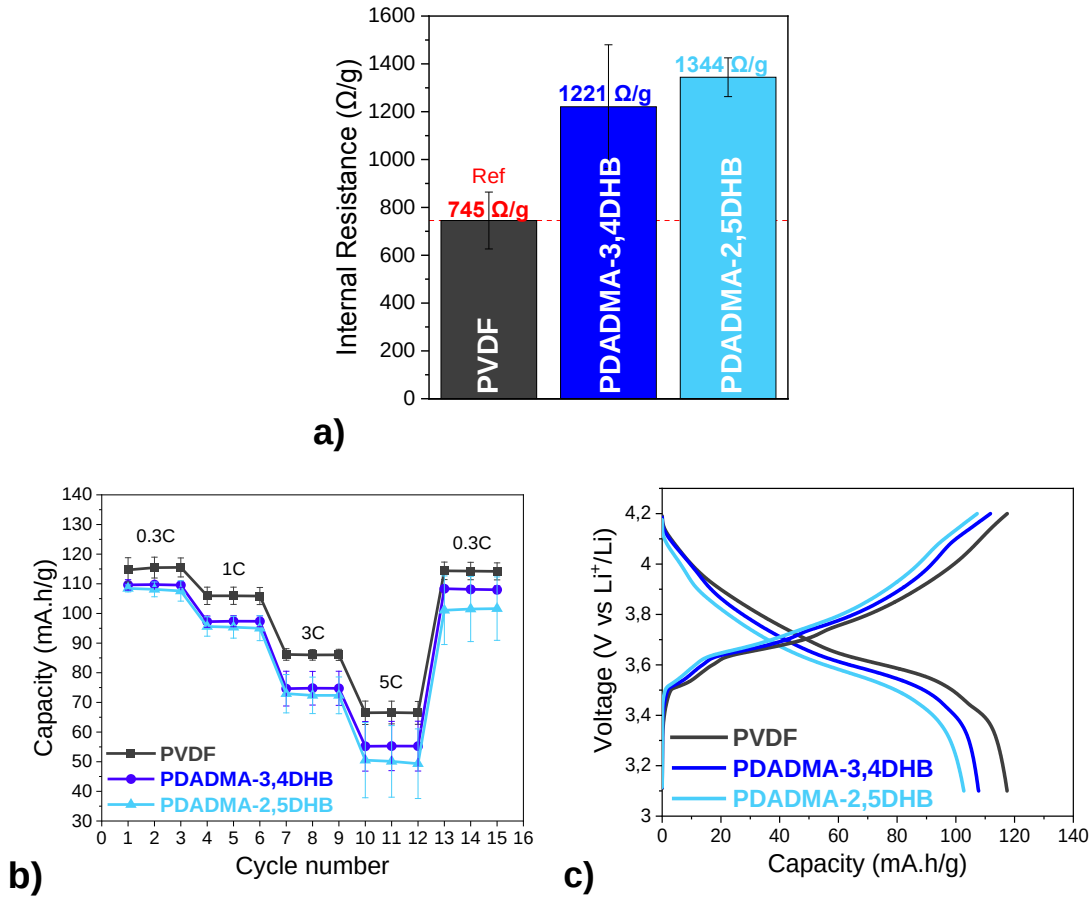

Figure 2.19. Application of PILs as binders in Li-ion (NMC) cathodes at 25 ºC: a) resistances of the cells measured by IV pulses; b) rate performance test; and c) charge-discharge voltage profiles at 0.3C rate.

The voltage profiles for the NMC cells cycling at 0.3C and 25 °C are shown in **Figure 2.19c.** The charge/discharge profiles show symmetrical capacities of 115, 110, and 108 mA.h/g for PVDF, PDADMA-3,4DH, and PDADMA-2,5DHB binders respectively. These values confirm the tendency observed previously for cell performances which can be noted PVDF > PDADMA-3,4DHB > PDADMA-2,5DHB.

The morphology of the cathode surfaces before cycling was analyzed by SEM, and the images are shown in **Figure 2.20**. As explained in the study of fluorinated PDADMA binders, the bright particles correspond to NMC and darker parts to carbon and binder additives. The electrode with PVDF as reference binder (**Figure 2.20a**) shows NMC

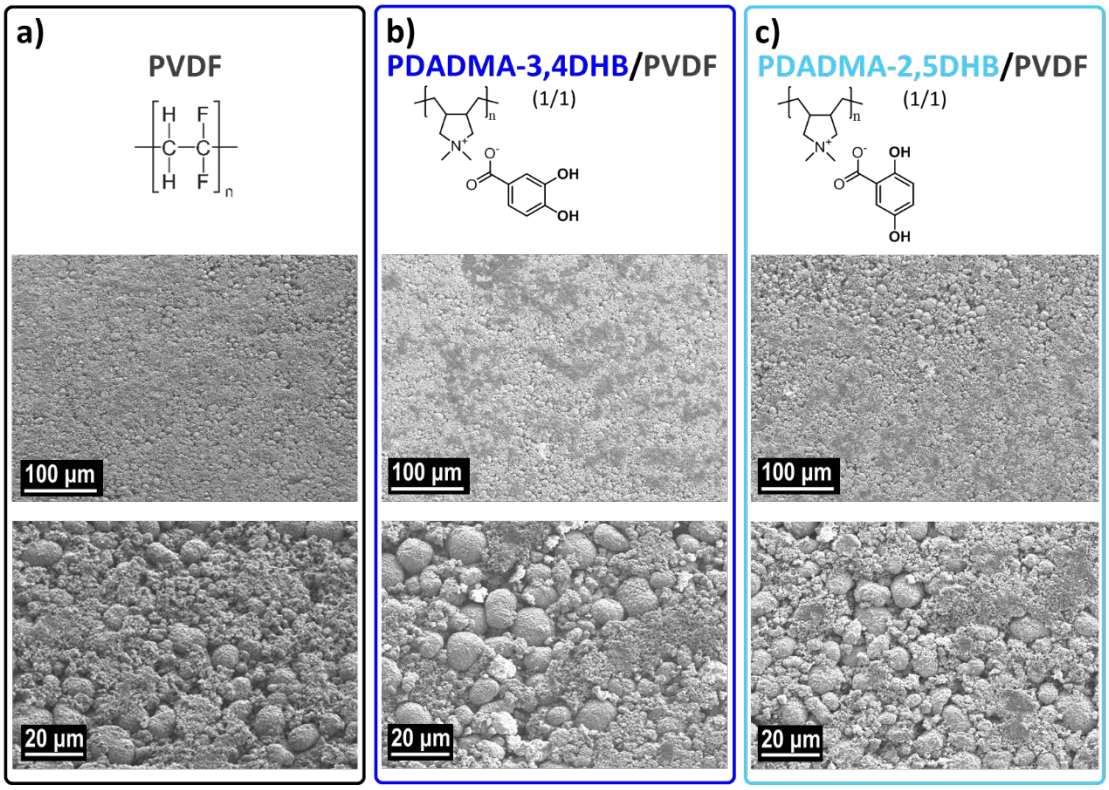

Figure 2.20. SEM images of cathode surfaces before cycling for a) PVDF; b) PDADMA-3,4DHB/PVDF; and c) PDADMA-2,5DHB/PVDF.

particles distributed homogeneously on the surface. However, electrodes with PDADMA-3.4DHB or PDADMA-2.5DHB as binders (**Figures 2.20b** and **2.20c** respectively) show darker areas that correspond to agglomerates of carbon and binder. The SEM images show that the electrodes with the PDADMA-DHB binders were not homogeneous and this is probably due to the low solubility of these polymers in NMP solvent during the preparation of the slurries. The non-uniformity of the electrodes is certainly one of the reasons why the performances of these cells are inferior to those with the PVDF binder and fluorinated PDADMAs.

2.6. Conclusion

Two families of pyrrolidinium-based poly(ionic liquid)s were synthesized to be used as cathode binders in Li-ion batteries. The poly(diallyldimethylammonium) was combined with two different kind of counter anions: the first family containing fluorine moieties with highly delocalized charge density to obtain PDADMA-TFSI, PDADMA-FSI, PDADMA-BETI, and PDADMA-CFSO polymers, and the second family, with two or three phenol groups to obtain PDADMA-3,4DHB, PDADMA-2,5DHB, PDADMA-3,4,5THB and PDADMA-2,3,4THB. The chemical structure, thermal stability and solubility of the polymers were evaluated by NMR, FTIR, and solubility tests in carbonate and NMP solvents to assess their potential application as battery binders. In addition, the synthesized PDADMA polymers were tested as binders in NMC cathodes for Li-ion batteries and compared to conventional PVDF binder.

Regarding PDADMA with fluorinated counter-anions, the current-voltage (IV) pulses and EIS results showed that the internal cell resistance decreased by 20-40% with PDADMA based binders, when compared to the PVDF-containing cell. Galvanostatic charge-discharge at different currents showed that PDADMA-BETI and PDADMA-CFSO cells obtained higher capacity values than PVDF at all the studied currents. This capacity increase with PDADMA-CFSO binder was of 9% at 0.3 C and 26% at 5C, when compared to PVDF. The cycling stability of the cells in accelerating aging conditions was also improved by PDADMA based binders, which demonstrate the applicability of these polymers as binder materials in high voltage cathodes for Li-ion batteries. In conclusion, it has been demonstrated that the presented PDADMA PILs with fluorinated anions are highly competitive alternatives to conventional binders, such as PVDF for Li-ion battery cathodes.

Concerning the PDADMA with polyphenol counter-anions, their electrochemistry properties were first studied in acidic aqueous electrolyte. PDADMA-3,4,5THB and PDADMA-2,3,4THB showed non-reversible redox behavior and were not further studied, unlike PDADMA-3,4DHB and PDADMA-2,5DHB, which shown interesting reversible redox peaks due to the catechol/benzoquinone redox pair. Then, PDADMA-3,4DHB and PDADMA-2,5DHB were investigated in lithium cells. Cyclic voltammetry analyses showed the unique activation step for the formation of quinone and a reversible electroactivity between 3.0 and 3.7V vs. Li^+/Li corresponding to the reaction of benzoquinone/dilithium catecholate redox pair. To end, PDADMA-3,4DHB and PDADMA-2,5DHB polymers were tested as binders in NMC cathodes and compared with PVDF used as reference. The results of current-voltage (IV) pulses and galvanostatic charge-discharge at different currents showed an increase in resistance and decrease in capacities compared to PVDF. The SEM images showed heterogeneity with polymer and carbon aggregates for electrodes with PDADMA-DHB binders, which may be one of the reasons for lower cell performance compared to PVDF. The problem of uniformity of the electrodes is certainly due to the NMP solvent used during the preparation of the slurries because the polymers were not soluble enough. To improve the composition of the electrodes and probably the cell performances, the solubility conditions of PDADMA-DHB polymer must be resolved. Despite the redox activity observed in cyclic voltammetry experiments, the application of PDADMA-DHB polymers as binders did not improve the performances of NMC cells compared to PVDF binders.

2.7. Experimental part

2.7.1. Materials

Poly(diallyldimethylammonium chloride) (PDADMA-Cl) with different molecular weight (M_w), namely high (average 400-500 kDa, 20 wt.% in water, Aldrich), and low (average <100 kDa, 20 wt.% in water, Aldrich), sodium bis(fluorosulfonyl)imide (NaFSI, 99.7%, Solvionic), lithium bis(trifluoro-methylsulfonyl)imide (LiTFSI, 99%, IoLiTec), lithium bis(perfluoroethylsulfonyl)imide (LiBETI, 99%, IoLiTec) and potassium nonafluoro-1-butanesulfonate ($KC_4F_9SO_3$, 95,0%, TCI), 3,4-Dihydroxybenzoic acid (3,4DHB, > 98.0%, TCI), 2,5-Dihydroxybenzoic acid (2,5DHB, > 98.0%, TCI), 3,4,5-Trihydroxybenzoic acid (3,4,5THB or Gallic acid, anhydrous, Sigma Aldrich), 2,3,4-Trihydroxybenzoic acid (2,3,4THB, > 98.0%, TCI), Amberlyte® IRN-78 ion-exchange resin OH-form (Acros Organics), 1-methyl-2-pyrrolidone (NMP, ≥99%, Sigma-Aldrich), 5wt% of poly(vinylidene fluoride) in NMP solvent (5wt% PVDF in NMP, PVDF M_w >10×10^5 g.mol^{-1}, KUREHA KF POLYMER), carbon black (acetylene, Alfa Aesar), NMC 523 (Custom Cells) were used as received. The methanol solvent from SharpLab were dried with anhydrous magnesium sulfate ($MgSO_4$) before used. All materials for electrochemical testing including Graphite electrode foil (active material content ≥95%, Custom Cells Itzehoe GmbH), NMC 532 cathode foil (active material content 90%, density 2.36 g.cm^{-3}, Custom Cells Itzehoe GmbH), and the glass fiber sheets (Whatman®, GF6 grade, Schleicher&Schüll) were previously dried at 100 ºC under vacuum for 24 h before introduced inside a glove box. The solvents used as electrolytes were used and stocked inside a glove box under argon atmosphere.

2.7.2. Synthesis of fluorinated PDADMA-PILs

Four fluorinated pyrrolidinium-based poly(ionic)liquids were synthesized by salt metathesis reactions, similarly to previously reported in literature [33,49].

Poly(diallyldimethylammonium bis(trifluoromethylsulfonyl)imide) **(PDADMA-TFSI):** 29.68 mmol of LiTFSI salt were dissolved in 10 ml of distilled water at room temperature (RT) and added dropwise to an aqueous solution of 24.74 mmol of monomeric units of PDADMA-Cl previously dissolved in 100 ml of distilled water at RT. Mixtures were stirred for at least 1 hour. After vacuum-filtration, the resulting precipitated polymer powder was washed in 300 mL of distilled water (stirring for 2 hours at RT) and vacuum-filtrated. Finally, the white polymer powder was vacuum-dried at 50 ºC for at least 48 hours before introducing it to an argon-filled glovebox.

Yield: 9.92 g (95.3%). Found: ^{1}H NMR (400 MHz, Acetone-d_6): δ (ppm) = 3.99, 3.37, 3.27, 2.85, 1.66, 1.48. Peaks in accordance to literature [33,34,49]. ^{13}C NMR (101 MHz, Acetone-d_6): δ (ppm) = 122.49 (-CH_2-N-), 119.30 (CH_3-N-), 72.06 (-CH-), 71.27 (-CH_2-CH-), 54.58 (-CH_2-CH-). Peaks in accordance to literature. ^{19}F NMR (376 MHz, Acetone-d_6): δ (ppm) = -79.73 (s, -CF_3).

Poly(diallyldimethylammonium bis(fluorolsulfonyl)imide) **(PDADMA-FSI):**

The same procedure previously described for PDADMA-TFSI was also used for the synthesis of PDADMA-FSI. NaFSI salt was used instead and a whitish fluffy powder could be obtained after drying.

Yield: 8.14 g (96.9%). Found: ^{1}H NMR (400 MHz, Acetone-d_6): δ (ppm) = 3.98, 3.38, 3.28, 2.39, 1.67, 1.46. Peaks in accordance to literature [33,34,49]. ^{13}C NMR (101 MHz,

Acetone-d_6): δ (ppm) = 71.37 (-CH_2-N-), 54.68 (CH_3-N-), 52.90 (-CH-), 39.69 (-CH_2-CH-), 39.07 (-CH_2-CH). ^{19}F NMR (376 MHz, Acetone-d_6): δ (ppm) = -51.6 (s, -F).

Poly(diallyldimethylammonium bis(perfluoroethylsulfonyl)imide **(PDADMA-BETI):**

The same procedure previously described for PDADMA-TFSI was also used for the synthesis of PDADMA-BETI. LiBETI salt was used instead and a whitish powder could be obtained after drying.

Yield: 12.39 g (95.8%). Found: ^{1}H NMR (400 MHz, Acetone-d_6, **Figure 2.21**): δ (ppm) = 4.17, 3.35, 3.24, 2.21, 1.39, 1.28. Peaks in accordance to literature [33,34,49]. ^{13}C NMR (101 MHz, DMSO-d_6, **Figure 2.22**): δ (ppm) = 122.05 (-CF_2-CF_3), 119.19 (-CF_2-CF_3), 116.33 (-CF_2-CF_3), 113.88 (-CF_2-CF_3), 110.96 (-CF_2-CF_3), 108.05 (-CF_2-CF_3), 69.43 (-CH_2-N-), 54.28 (CH_3-N-), 51.27 (-CH-), 39.52 (-CH_2-CH-), 37.25 (-CH_2-CH). ^{19}F NMR (376 MHz, Acetone-d_6, **Figure 2.23**): δ (ppm) = -79.87 (-CF_2-CF_3); -118.29 (-CF_2-CF_3).

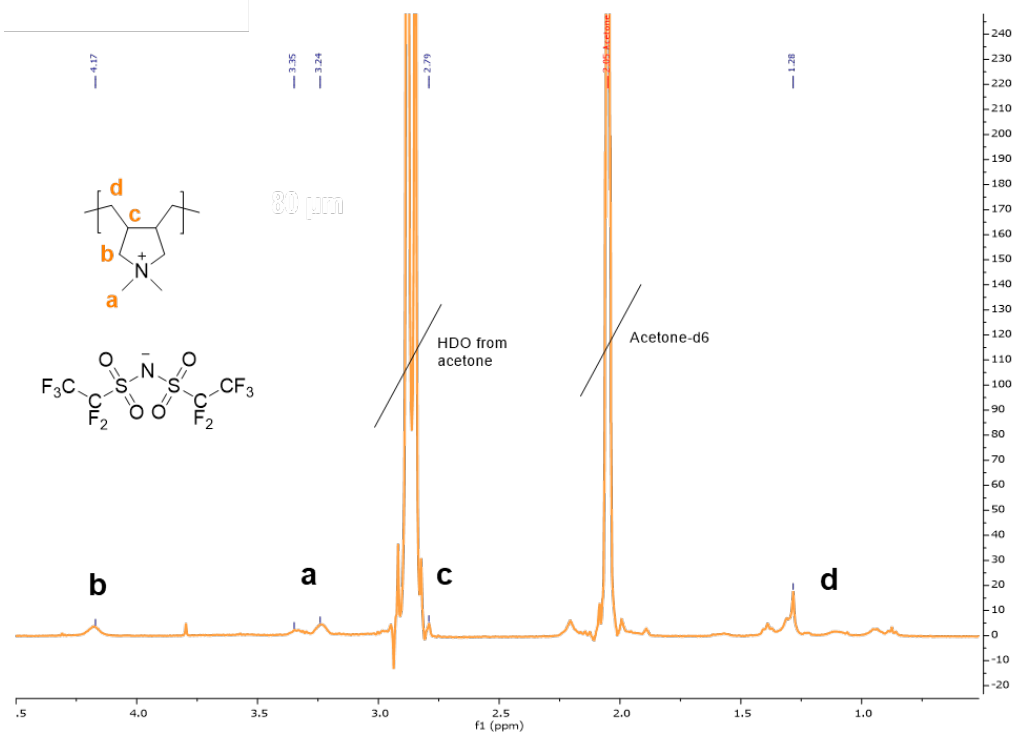

Figure 2.21. ^{1}H NMR of PDADMA-BETI PIL.

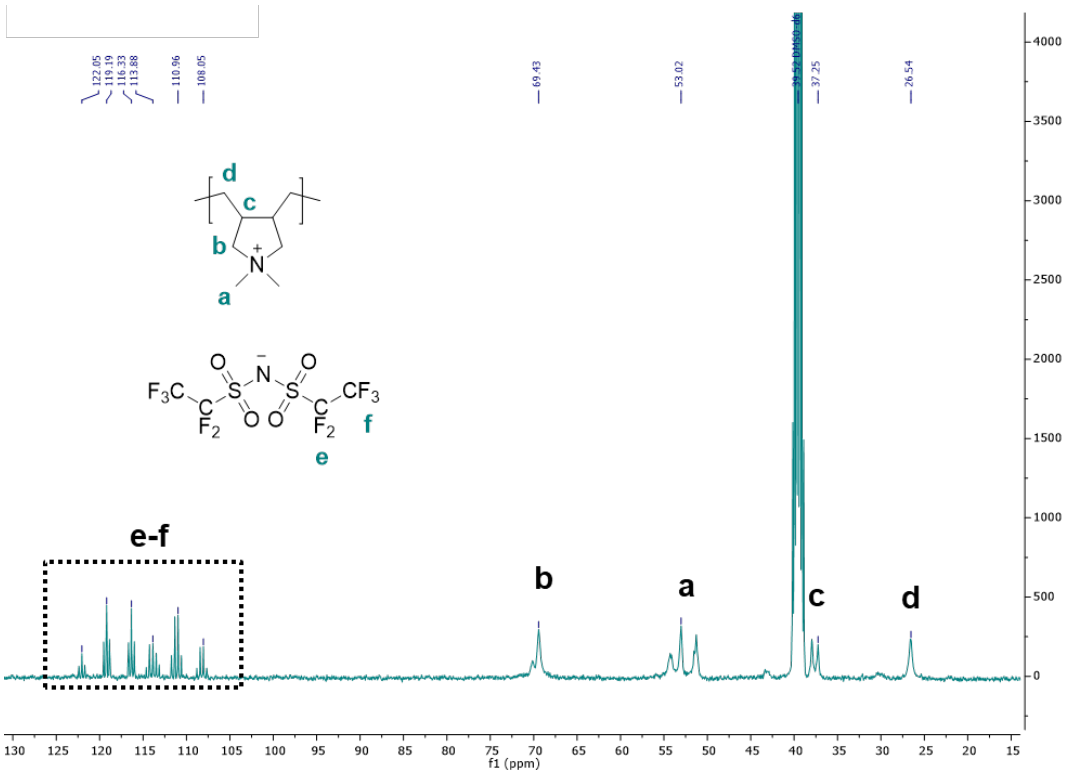

Figure 2.22. ^{13}C NMR of PDADMA-BETI PIL.

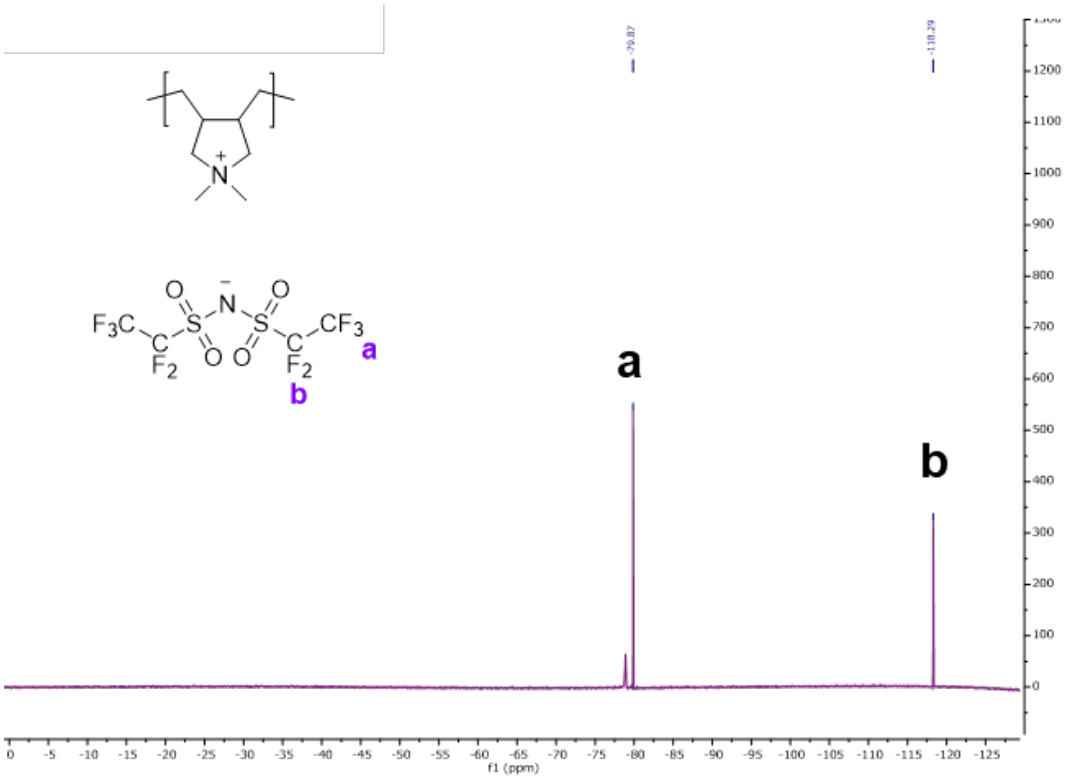

Figure 2.23. ^{19}F NMR of PDADMA-BETI PIL.

Poly(diallyldimethylammonium nonafluoro-1-butanesulfonate **(PDADMA-CFSO):** 29.68 mmol of $KC_4F_9SO_3$ were dissolved in 125 ml of distilled water at 60 ºC and added dropwise to an aqueous solution of 24.74 mmol of monomeric units of PDADMA-Cl previously dissolved in 100 ml of distilled water at 50 °C. Mixtures were stirred for at least 1 hour. After vacuum-filtration, the resulting precipitated polymer powder was washed in 300 mL of distilled water (stirring for 2 hours at RT) and vacuum-filtrated. Finally, the polymeric hard rocky powder was vacuum-dried at 50 °C for at least 48 hours. Yield: 10.01 g (93.5%); Found: ^{1}H NMR (400 MHz, Acetone-d_6): δ (ppm) = 4.06, 3.36, 3.25, 2.21, 1.62, 1.44. Peaks in accordance to literature [33,34,49]. ^{13}C NMR (101 MHz, DMSO-d_6): δ (ppm) = 121.43 (-CF_2-CF_2-CF_2-CF_3), 118.56 (-CF_2-CF_2-CF_2-CF_3), 115.70 (-CF_2-CF_2-CF_2-CF_3), 113.47 (-CF_2-CF_2-CF_2-CF_3), 110.45 (-CF_2-CF_2-CF_2-CF_3), 108.32 (-CF_2-CF_2-CF_2-CF_3), 105.65 (-CF_2-CF_2-CF_2-CF_3), 69.38 (-CH_2-N-), 52.93 (CH_3-N-), 51.17 (-CH-), 39.52 (-CH_2-CH-), 37.25 (-CH_2-CH). ^{19}F NMR (376 MHz, Acetone-d_6): δ (ppm) = -81.85 (s, -CF_2-CF_2-CF_2-CF_3), -115.34 (s, -CF_2-CF_2-CF_2-CF_3), -122.00 (s, -CF_2-CF_2-CF_2-CF_3), -126.65 (s, -CF_2-CF_2-CF_2-CF_3).

2.7.3. Synthesis of redox-active PDADMA PILs

Four redox-active pyrrolidinium-based poly(ionic)liquids were synthesized via a two-step anion exchange reaction with Amberlyte® IRN-78 resin (hydroxide form), similarly to previously reported in literature [35].

Poly(diallyldimethylammonium)-3,4-Dihydroxybenzoate **(PDADMA-3,4DHB):** Initially, 12.9 mmol of P(DADMA)Cl were dissolved in 130 mL of MeOH. The Amberlite® IRN-78 resin previously mixed in MeOH overnight at RT, was loaded for a bed volume (BV) of 8 cm into a 2 cm diameter column. The P(DADMA)Cl solution was

passed through the column at a slow flow rate with an additional 25 mL of fresh MeOH. The transparent solution of P(DADMA)OH was collected in a balloon kept at low temperature with an ice bath. Finally, 12.9 mmol of 3,4-Dihydroxybenzoic acid was added to the solution collected, and instantly, the white precipitate of PDADMA-3,4DHB was formed. The mixture was stirred for 2 h at low temperature and overnight at RT. To finish, the mixture was washed with MeOH, and dried on a rotary evaporator and under vacuum at 60 ºC overnight.

Yield: 2.3 g (66%). Found: ^{1}H NMR (400 MHz, D_2O): δ (ppm) = 7.47 (s, 1H), 7.44 (d, 1H), 7.01 (d, 1H), 3.81 (s, 2H), 3.27 (s, 6H), 3.14 (s, 2H), 2.8-2.3 (m, 2H), 1.8-1.0 (m, 4H); ^{13}C NMR (101 MHz, D_2O) δ (ppm) = 174.18, 147.55, 143.25, 127.26, 122.96, 117.06, 115.61, 70.38, 54.84, 54.17, 52.48, 49.23, 38.53, 38.24, 26.51.

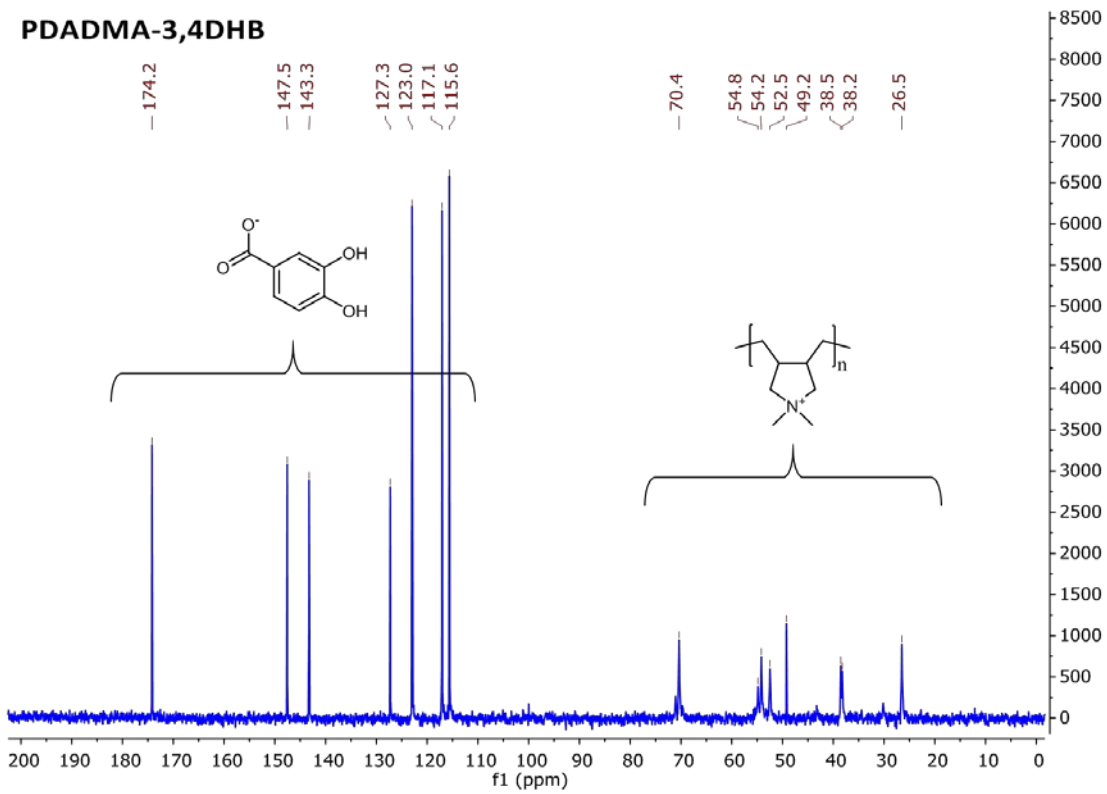

Figure 2.24. ^{13}C NMR spectra for PDADMA-3,4DHB.

Poly(diallyldimethylammonium)-2,5-Dihydroxybenzoate **(PDADMA-2,5DHB):**

The same procedure previously described for PDADMA-3,4DHB was also used for the synthesis of PDADMA-2,5DHB. 2,5-Dihydroxybenzoic acid was used instead and a white powder could be obtain after drying.

Yield: 1.9 g (51%). Found: ^{1}H NMR (400 MHz, D_2O): δ (ppm) = 7.35 (d, J = 3.0 Hz, 1H), 7.10 (dd, J_m = 3.0 Hz, J_o = 8.7 Hz, 1H), 6.92 (d, J = 8.7 Hz, 1H), 3.84 (s, 2H), 3.31 (s, 6H), 3.18 (s, 2H), 2.8-2.2 (m, 2H), 1.6-1.0 (m, 4H); ^{13}C NMR (101 MHz, D_2O) δ (ppm) = 175.02, 153.21, 147.55, 121.89, 118.37, 117.45, 116.13, 70.44, 54.95, 54.39, 52.67, 49.56, 38.58, 38.34, 26.55.

Poly(diallyldimethylammonium)-3,4,5-Dihydroxybenzoate **(PDADMA-3,4,5THB):**

The same procedure previously described for PDADMA-3,4DHB was also used for the synthesis of PDADMA-3,4,5THB. 3,4,5-trihydroxybenzoic acid was used instead and the solution instantly colored red before quickly forming the whitish precipitate.

Yield: 3.2 g (84%). Found: ^{1}H NMR (400 MHz, D_2O): δ (ppm) = 7.22 (s, 2H), 3.88 (s, 2H), 3.35 (s, 6H), 3.22 (s, 2H), 2.9-2.1 (m, 2H), 1.8-0.9 (m, 4H); ^{13}C NMR (101 MHz, D_2O) δ (ppm) = 174.70, 144.06, 135.82, 127.17, 110.13, 70.53, 55.11, 54.51, 52.80, 49.85, 38.59, 38.31, 26.59.

Poly(diallyldimethylammonium)-2,3,4-Dihydroxybenzoate **(PDADMA-2,3,4THB):**

The same procedure previously described for PDADMA-3,4DHB was also used for the synthesis of PDADMA-2,3,4THB. 2,4,5-Trihydroxybenzoic acid was used instead and the solution instantly colored yellow-green before quickly forming the whitish precipitate.

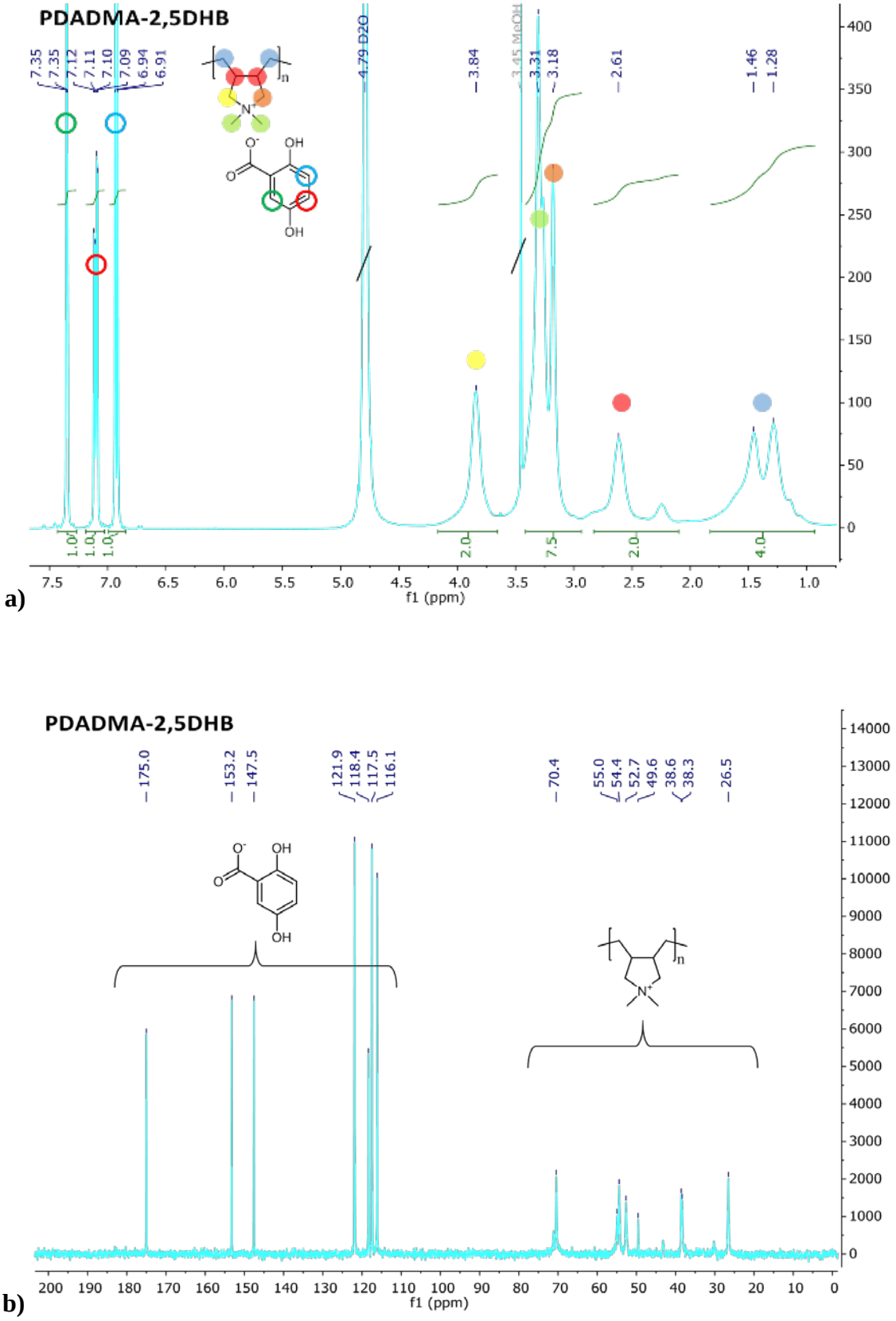

Figure 2.25. PDADMA-2,5DHB a) ^{1}H NMR spectra, b) ^{13}C NMR spectra.

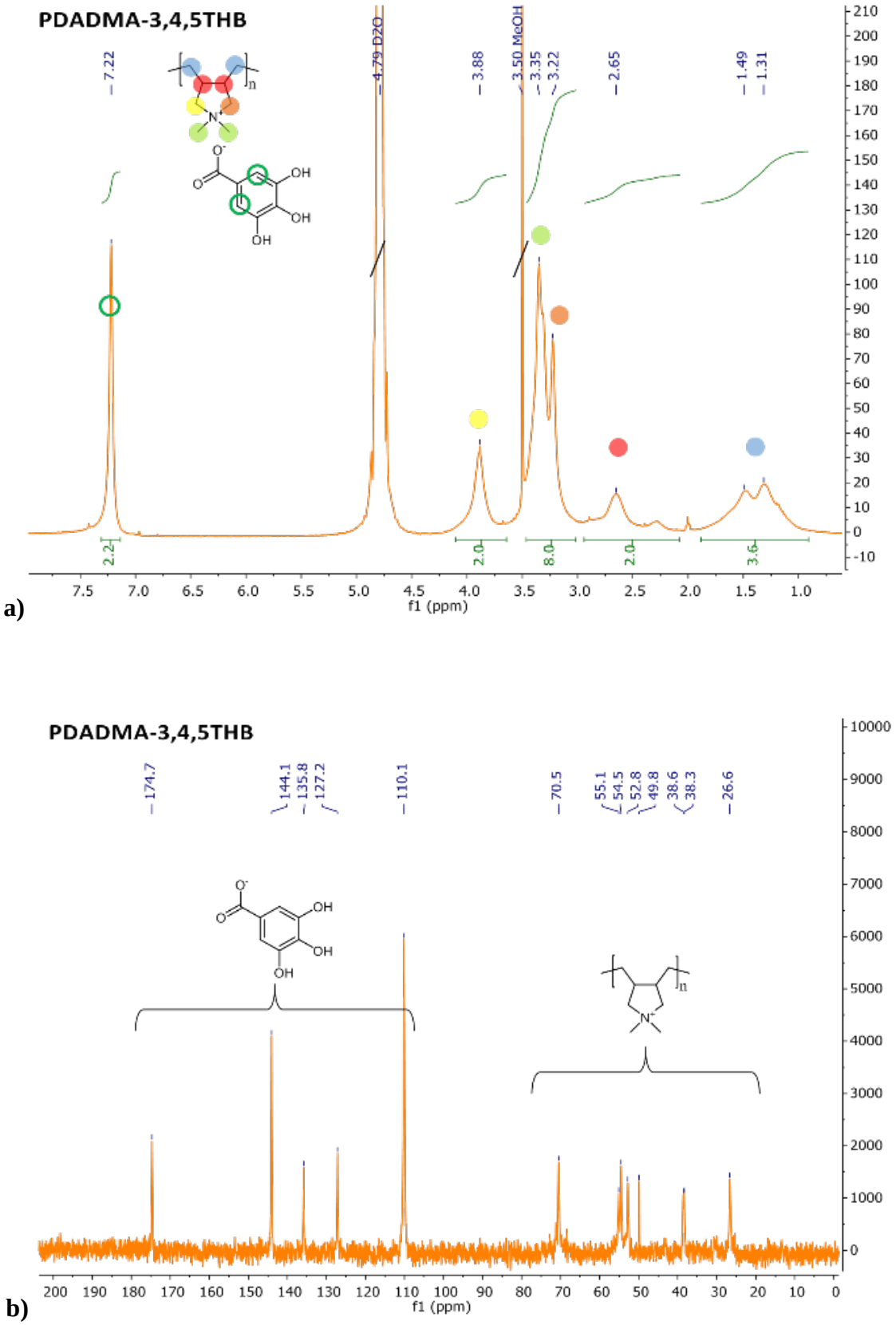

Figure 2.26. PDADMA-3,4,5THB a) ^{1}H NMR spectra, b) ^{13}C NMR spectra.

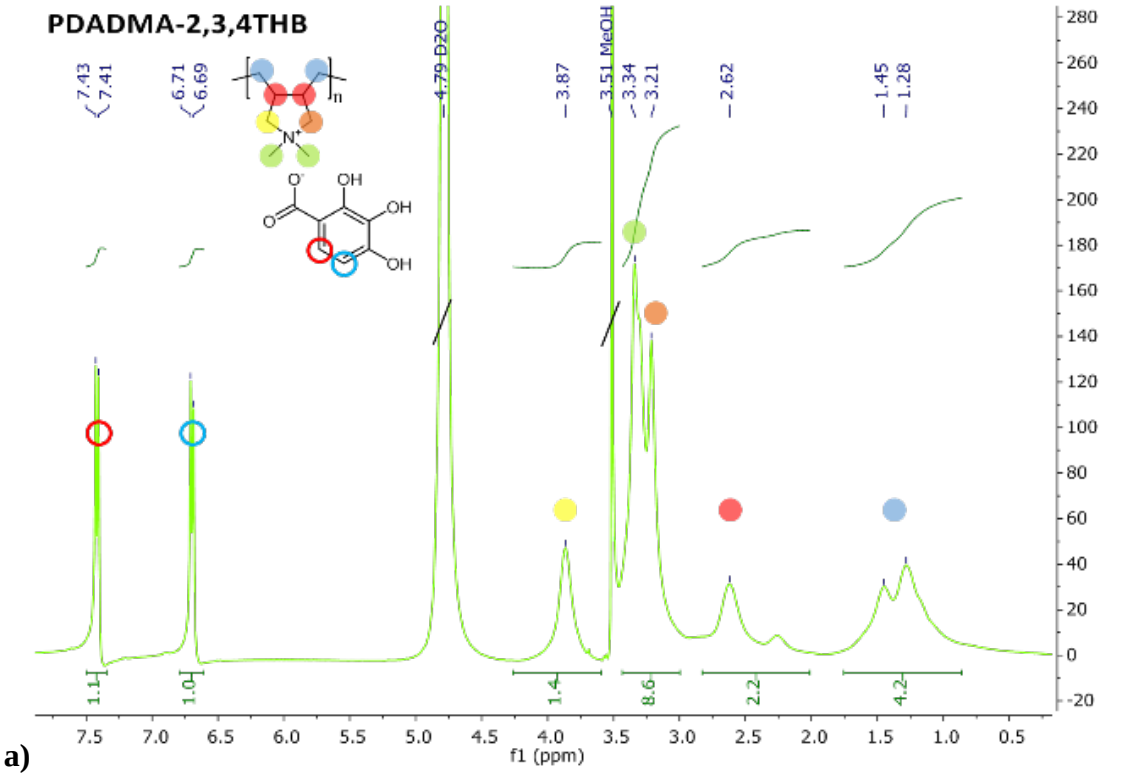

a)

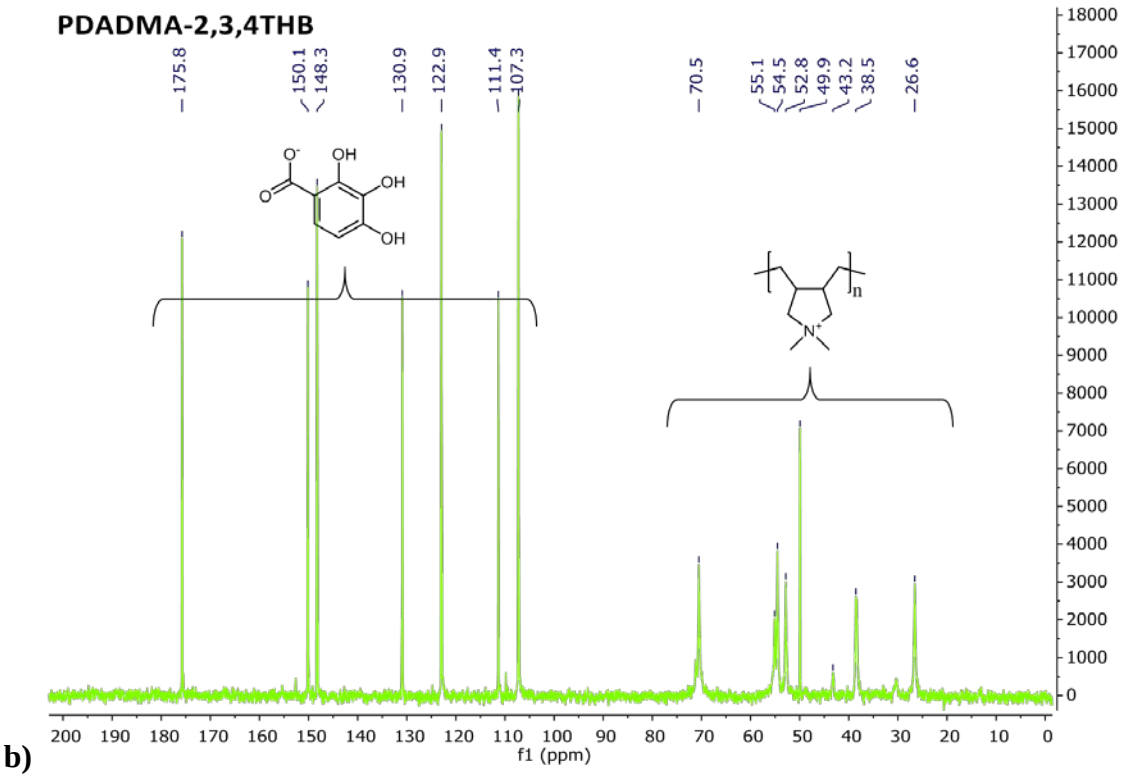

b)

Figure 2.27. PDADMA-2,3,4THB a) ^{1}H NMR spectra, b) ^{13}C NMR spectra.

Yield: 2.3 g (64%). Found: ^{1}H NMR (400 MHz, D_2O): δ (ppm) = 7.42 (d, J = 8.7 Hz, 1H), 6.70 (d, J = 8.7 Hz, 1H), 3.87 (s, 2H), 3.34 (s, 6H), 3.21 (s, 2H), 2.7-2.0 (m, 2H), 1.7-0.8 (m, 4H); ^{13}C NMR (101 MHz, D_2O) δ (ppm) = 175.75, 150.14, 148.26, 130.92, 122.93, 111.35, 107.25, 70.52, 55.12, 54.52, 52.83, 49.93, 43.21, 38.54, 26.56.

2.7.4. Polymer characterizations

The chemical structures of the synthesized pyrrolidinium-based PILs were confirmed by ^{1}H, ^{19}F and ^{13}C Nuclear Magnetic Resonance (NMR) spectroscopy (Bruker Avance III 400 MHz Digital NMR spectrometer) using acetone-d_6 or deuterium oxide (D_2O) solvent and by Fourier Transform Infrared Spectroscopy (Nicolet Magna 6700 FTIR spectrometer) at RT and under air atmosphere.

The thermal properties were evaluated by Thermal Gravimetric Analysis (TGA) employing a Q500 analyzer (TA instruments) performed under N_2 with a heating rate of 10 °C.min^{-1} from RT to 800 °C and the decomposition temperatures (T_d) were measured by the onset-temperature.

The solubility of polymers was analyzed with a solution of 5 wt.% polymer mixed for 12 h. The solution was centrifuged twice for 15 min at 3500 rpm. The supernatant was collected and weighed (m_1) in a vial. Then it was dried at 60 ºC under vacuum for 12 h or until a stable weight (m_2). The solubility of polymers was calculated using the following equation:

$$S(\%) = \frac{m_2}{m_1} \times 100$$

where m_1 and m_2 correspond respectively to the masses before and after the drying step.

Scanning Electron Microscopy (SEM) images were acquired on a JSM IT 300 series SEM at an accelerating voltage of 2kV.

2.7.5. Electrochemical analysis of redox activity of PDADMA PILs

The electrochemical characterizations of the PDADMA redox PILs were evaluated with an Autolab PGSTAT302N by using the standard three-electrode configuration as represented in **Figure 2.7a** where a platinum wire, an Ag/AgCl (KCl sat.) and glassy carbon electrode (GC, with area of 0.07 cm^2) were used as counter (CE), reference (RE) and working electrodes, respectively. 3 µL of slurries containing Polymer:Carbon with a ratio of 1:1 by wt.% in NMP solvent were drop casted onto the carbon electrode and dried at RT for 1 h, then at 60 ºC for 1 h and under vacuum for another 1 h. The electrolyte solution was a 0.1 M $HClO_4$ in H_2O purged with nitrogen for 30 minutes. The potential window of the cyclic voltammetry (CV) was cycled from -0.4 V to 1.2 V vs Ag/AgCl by applying 5 cycles at 0.2 $mV.s^{-1}$ at 25 ºC.

The theoretical capacities $Q_{théo}\ (mA.h/g)$ of PDADMA-DHB polymers were calculated using the following equation:

$$Q_{théo} = \frac{\mathrm{n} \times \mathrm{F} \times 1000}{M_w \times 3600}$$

where n, F and M_w correspond to the number of charge carrier, the Faraday constant (96 485 $C.mol^{-1}$) and the molecular weight of the active material used in the electrode ($g.mol^{-1}$) respectively.

2.7.6. Preparation of the Li-ion batteries

All NMC cathodes were prepared with slurries composed by NMC 532, acetylene black, and corresponding binder in weight ratio of 90:5:5 in NMP solvent. The slurries were prepared by mixing with a planetary mixer (twice for 5 min at 2000 rpm) and a rotor stator mixer (twice for 120 seconds at 20 $m.s^{-1}$). Then, the slurries were casted onto aluminum foil by film applicator (200 µm of thickness and 12.5 $mm.s^{-1}$ of velocity) and were dried under vacuum at 90 °C for 12h. 14 mm diameter cathodes were punched and pressed under 6 tons to obtain around 2.4 $g.cm^{-3}$ mass loading. The cathodes were dried again under vacuum at 90 °C for 24 h before cell assembling.

Lithium-ion batteries were assembled using NMC/C/binder as cathode (Φ 14), graphite electrode as anode and a glass fiber soaked with 120 µL of 1.0M $LiPF_6$ in Ethylene Carbonate: Ethyl Methyl Carbonate (1:1 vol.% EC:EMC) liquid electrolyte in CR 2032 coin cells.

2.7.7. Electrochemical characterizations in lithium-ion batteries

Li-ion cells were tested through galvanostatic discharge–charge (GDC) cycling using a Multi Potentiostat MPG2-6 and VMP3-1 (Bio-Logic). The voltage range was 3.1–4.2 V vs Li^+/Li. **Figure 2.28** describes the testing protocol for the evaluation of the assembled Li-ion cells. It was divided in 5 main steps: Activation, Capacity check, target on 56% of State of Charge (SoC), IV measurement allowing Resistance calculation and target to discharged state (SoC = 0%).

The first step was the activation of the cell which consists of a galvanostatic charge with a constant current of 0.3C (1C means the current needed to achieve full capacity in 1h) based on the theoretical capacity from open circuit voltage (OCV = SoC 0%) to 4.2V for NMC || graphite cells. Then, one discharge-charge cycle between 4.2V and 3.1V was applied still under galvanostatic current of 0.3C in order to form the SEI on the graphite electrode and not to perturb the capacity check.

In the second step, the capacity check was carried out through a galvanostatic discharge charge cycle with a constant current of 0.3C. From this step, experimental capacities were extracted and calculated to use as reference for the next steps and define more precisely the current used for the IV test on one side, and the SoC = 56% state.

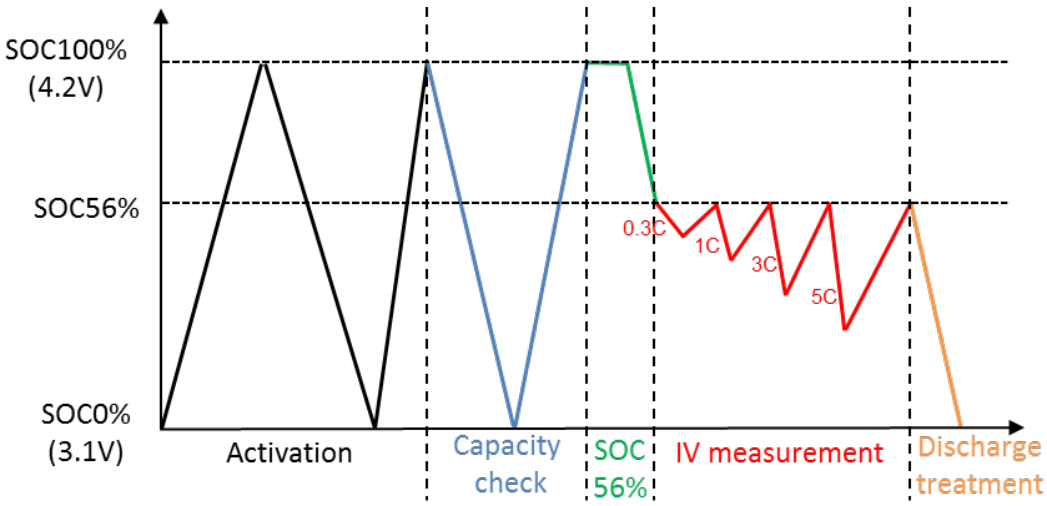

Figure 2.28. Battery test program used for Li-ion cells.

The resistance of all Li-ion prototype cells was then evaluated on the same way. The SoC = 56% test was chosen because it allowed the Li-ion cell to be in an area where small variations of current would have small impacts on the potential; hence, not perturbing the

measurement of the resistance. The next step was the IV measurement (or DC measurement). It allowed measuring the overall resistance of the coin cell based on different applied currents. It provided a reliable evaluation of the different binders, as the only modification in the different cells evaluated was the binder used in the positive electrode. Thus, this measurement allowed observing the binder effect on the performances and, more precisely, the resistance. Overall, this test consisted in applying for a short period of time (10s) a current of different magnitude (0.3C, 1C, 3C and 5C). After each current pulse, the cell was charged to the same 56% SoC level as from the start of this step. Output data from this measurement was the evaluation of the voltage drop as a function of the applied current (**Figure 2.29**). This gave a linear relationship following the Ohm's law that was used to determine the cell resistance value [41].

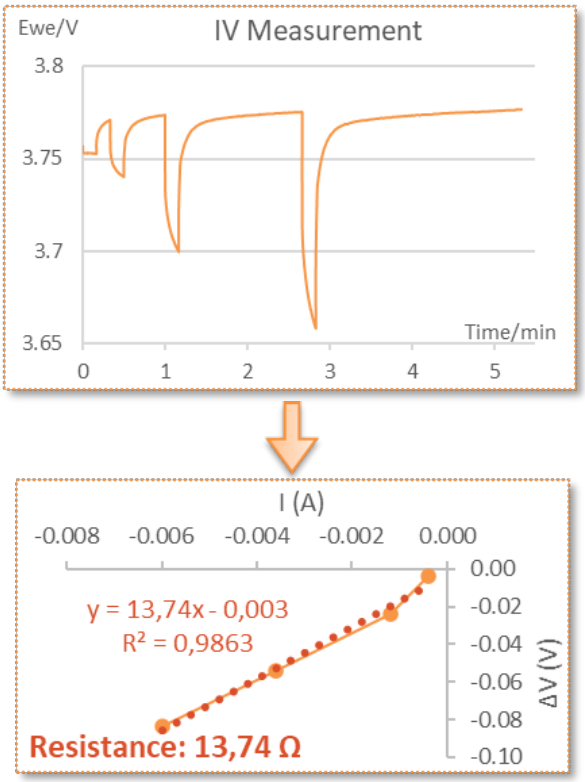

Figure 2.29. Example of Li-ion cell resistance measurement (IV test).

Electrochemical Impedance Spectroscopy (EIS) measurements were conducted at SoC56 applying a 10 mV perturbation in the frequency range of 1 MHz to 30 mHz.

Each test was repeated at least three times and the results shown are the average with the standard deviation.

2.8. References

(1) Casado, N.; Hernández, G.; Sardon, H.; Mecerreyes, D. Current Trends in Redox Polymers for Energy and Medicine. *Prog. Polym. Sci.* **2016**, *52*, 107–135.

(2) Kim, T.; Song, W.; Son, D. Y.; Ono, L. K.; Qi, Y. Lithium-Ion Batteries: Outlook on Present, Future, and Hybridized Technologies. *J. Mater. Chem. A* **2019**, *7* (7), 2942–2964.

(3) Ma, Z.; Yuan, X.; Li, L.; Ma, Z. F.; Wilkinson, D. P.; Zhang, L.; Zhang, J. A Review of Cathode Materials and Structures for Rechargeable Lithium-Air Batteries. *Energy Environ. Sci.* **2015**, *8* (8), 2144–2198.

(4) Mecerreyes, D.; Porcarelli, L.; Casado, N. Innovative Polymers for Next-Generation Batteries. *Macromol. Chem. Phys.* **2020**, *221* (4), 1–7.

(5) Spanos, I.; Neugebauer, S.; Guterman, R.; Yuan, J.; Schlögl, R.; Antonietti, M. Poly(Ionic Liquid) Binders as Ionic Conductors and Polymer Electrolyte Interfaces for Enhanced Electrochemical Performance of Water Splitting Electrodes. *Sustain. Energy Fuels* **2018**, *2* (7), 1446–1451.

(6) Chou, S.-L.; Pan, Y.; Wang, J.-Z.; Liu, H.-K.; Dou, S.-X. Small Things Make a Big Difference: Binder Effects on the Performance of Li and Na Batteries. *Phys. Chem. Chem. Phys.* **2014**, *16* (38), 20347–20359.

(7) Tsao, C.-H.; Wu, E.-T.; Lee, W.-H.; Chiu, C.; Kuo, P.-L. Fluorinated Copolymer Functionalized with Ethylene Oxide as Novel Water-Borne Binder for a High-Power Lithium Ion Battery: Synthesis, Mechanism, and Application. *ACS Appl. Energy Mater.* **2018**, *1* (8), 3999–4008.

(8) Liang, J.; Chen, D.; Adair, K.; Sun, Q.; Holmes, N. G.; Zhao, Y.; Sun, Y.; Luo, J.; Li, R.; Zhang, L.; Zhao, S.; Lu, S.; Huang, H.; Zhang, X.; Singh, C. V.; Sun, X. Insight into Prolonged Cycling Life of 4 V All-Solid-State Polymer Batteries by a

High-Voltage Stable Binder. *Adv. Energy Mater.* **2021**, *11* (1), 2002455.

(9) Loeffler, N.; Kim, G.-T.; Passerini, S.; Gutierrez, C.; Cendoya, I.; De Meatza, I.; Alessandrini, F.; Appetecchi, G. B. Performance and Ageing Robustness of Graphite/NMC Pouch Prototypes Manufactured through Eco-Friendly Materials and Processes. *ChemSusChem* **2017**, *10* (18), 3581–3587.

(10) Bresser, D.; Buchholz, D.; Moretti, A.; Varzi, A.; Passerini, S. Alternative Binders for Sustainable Electrochemical Energy Storage-the Transition to Aqueous Electrode Processing and Bio-Derived Polymers. *Energy Environ. Sci.* **2018**, *11* (11), 3096–3127.

(11) Kuenzel, M.; Choi, H.; Wu, F.; Kazzazi, A.; Axmann, P.; Wohlfahrt-Mehrens, M.; Bresser, D.; Passerini, S. Co-Crosslinked Water-Soluble Biopolymers as a Binder for High-Voltage LiNi0.5Mn1.5O4|Graphite Lithium-Ion Full Cells. *ChemSusChem* **2020**, *13* (10), 2650–2660.

(12) Li, J.; Klöpsch, R.; Nowak, S.; Kunze, M.; Winter, M.; Passerini, S. Investigations on Cellulose-Based High Voltage Composite Cathodes for Lithium Ion Batteries. *J. Power Sources* **2011**, *196* (18), 7687–7691.

(13) Carvalho, D. V.; Loeffler, N.; Hekmatfar, M.; Moretti, A.; Kim, G. T.; Passerini, S. Evaluation of Guar Gum-Based Biopolymers as Binders for Lithium-Ion Batteries Electrodes. *Electrochim. Acta* **2018**, *265*, 89–97.

(14) Li, Y.; Zeng, Q. (Ray); Gentle, I. R.; Wang, D.-W. Carboxymethyl Cellulose Binders Enable High-Rate Capability of Sulfurized Polyacrylonitrile Cathodes for Li–S Batteries. *J. Mater. Chem. A* **2017**, *5* (11), 5460–5465.

(15) Von Zamory, J.; Bedu, M.; Fantini, S.; Passerini, S.; Paillard, E. Polymeric Ionic Liquid Nanoparticles as Binder for Composite Li-Ion Electrodes. *J. Power Sources* **2013**, *240*, 745–752.

(16) Forsyth, M.; Porcarelli, L.; Wang, X.; Goujon, N.; Mecerreyes, D. Innovative Electrolytes Based on Ionic Liquids and Polymers for Next-Generation Solid-State Batteries. *Acc. Chem. Res.* **2019**, *52* (3), 686–694.

(17) Vizintin, A.; Guterman, R.; Schmidt, J.; Antonietti, M.; Dominko, R. Linear and Cross-Linked Ionic Liquid Polymers as Binders in Lithium–Sulfur Batteries. *Chem. Mater.* **2018**, *30* (15), 5444–5450.

(18) Eshetu, G. G.; Mecerreyes, D.; Forsyth, M.; Zhang, H.; Armand, M. Polymeric Ionic Liquids for Lithium-Based Rechargeable Batteries. *Molecular Systems Design and Engineering*. Royal Society of Chemistry April 1, 2019, pp 294–309.

(19) Lee, J. S.; Sakaushi, K.; Antonietti, M.; Yuan, J. Poly(Ionic Liquid) Binders as Li+ Conducting Mediators for Enhanced Electrochemical Performance. *RSC Adv.* **2015**, *5* (104), 85517–85522.

(20) Grygiel, K.; Lee, J. S.; Sakaushi, K.; Antonietti, M.; Yuan, J. Thiazolium Poly(Ionic Liquid)s: Synthesis and Application as Binder for Lithium-Ion Batteries. *ACS Macro Lett.* **2015**, *4* (12), 1312–1316.

(21) Jayakumar, T. P.; Badam, R.; Matsumi, N. Allylimidazolium-Based Poly(Ionic Liquid) Anodic Binder for Lithium-Ion Batteries with Enhanced Cyclability. *ACS Appl. Energy Mater.* **2020**, *3* (4), 3337–3346.

(22) Tomé, L. C.; Mecerreyes, D.; Freire, C. S. R.; Rebelo, L. P. N.; Marrucho, I. M. Pyrrolidinium-Based Polymeric Ionic Liquid Materials: New Perspectives for CO2 Separation Membranes. *J. Memb. Sci.* **2013**, *428*, 260–266.

(23) Wang, X.; Zhu, H.; Girard, G. M. A.; Yunis, R.; Macfarlane, D. R.; Mecerreyes, D.; Bhattacharyya, A. J.; Howlett, P. C.; Forsyth, M. Preparation and Characterization of Gel Polymer Electrolytes Using Poly(Ionic Liquids) and High Lithium Salt Concentration Ionic Liquids. *J. Mater. Chem. A* **2017**, *5* (45), 23844–

(24) Lee, J. S.; Sakaushi, K.; Antonietti, M.; Yuan, J. Poly(Ionic Liquid) Binders as Li+ Conducting Mediators for Enhanced Electrochemical Performance. *RSC Adv.* **2015**, *5* (104), 85517–85522.

(25) Patil, N.; Jérôme, C.; Detrembleur, C. Recent Advances in the Synthesis of Catechol-Derived (Bio)Polymers for Applications in Energy Storage and Environment. *Prog. Polym. Sci.* **2018**, *82*, 34–91.

(26) Goujon, N.; Casado, N.; Patil, N.; Marcilla, R.; Mecerreyes, D. Organic Batteries Based on Just Redox Polymers Abstract. *Prog. Polym. Sci.* **2021**, *122*, 101449.

(27) Hatakeyama-Sato, K.; Masui, T.; Serikawa, T.; Sasaki, Y.; Choi, W.; Doo, S. G.; Nishide, H.; Oyaizu, K. Nonconjugated Redox-Active Polymer Mediators for Rapid Electrocatalytic Charging of Lithium Metal Oxides. *ACS Appl. Energy Mater.* **2019**, *2* (9), 6375–6382.

(28) Zhang, Q.; Sha, Z.; Cui, X.; Qiu, S.; He, C.; Zhang, J.; Wang, X.; Yang, Y. Incorporation of Redox-Active Polyimide Binder into LiFePO4cathode for High-Rate Electrochemical Energy Storage. *Nanotechnol. Rev.* **2021**, *9* (1), 1350–1358.

(29) Kim, S.; Cho, M.; Chanthad, C.; Lee, Y. New Redox-Mediating Polymer Binder for Enhancing Performance of Li-S Batteries. *J. Energy Chem.* **2020**, *44*, 154–161.

(30) Pirnat, K.; Casado, N.; Porcarelli, L.; Ballard, N.; Mecerreyes, D. Synthesis of Redox Polymer Nanoparticles Based on Poly(Vinyl Catechols) and Their Electroactivity. *Macromolecules* **2019**, *52*, 8155–8166.

(31) Patil, N.; Mavrandonakis, A.; Jérôme, C.; Detrembleur, C.; Palma, J.; Marcilla, R. Polymers Bearing Catechol Pendants as Universal Hosts for Aqueous Rechargeable H+, Li-Ion, and Post-Li-Ion (Mono-, Di-, and Trivalent) Batteries. *ACS Appl. Energy Mater.* **2019**, *2* (5), 3035–3041.

(32) Patil, N.; Aqil, A.; Ouhib, F.; Admassie, S.; Inganäs, O.; Jérôme, C.; Detrembleur,

C. Bioinspired Redox-Active Catechol-Bearing Polymers as Ultrarobust Organic Cathodes for Lithium Storage. *Adv. Mater.* **2017**.

(33) Pont, A. L.; Marcilla, R.; De Meatza, I.; Grande, H.; Mecerreyes, D. Pyrrolidinium-Based Polymeric Ionic Liquids as Mechanically and Electrochemically Stable Polymer Electrolytes. *Journal of Power Sources*. 2009, pp 558–563.

(34) Del Olmo, R.; Casado, N.; Olmedo-Martínez, J. L.; Wang, X.; Forsyth, M. Mixed Ionic-Electronic Conductors Based on PEDOT : PolyDADMA and Organic Ionic Plastic Crystals. *Polymers (Basel).* **2020**, No. 12, 1981.

(35) Pothanagandhi, N.; Sivaramakrishna, A.; Vijayakrishna, K. Chiral Anion Triggered Helical Poly (Ionic Liquids). *Polym. Chem.* **2017**, *8* (5), 918–925.

(36) Tomé, L. C.; Aboudzadeh, M. A.; Rebelo, L. P. N.; Freire, C. S. R.; Mecerreyes, D.; Marrucho, I. M. Polymeric Ionic Liquids with Mixtures of Counter-Anions: A New Straightforward Strategy for Designing Pyrrolidinium-Based CO2 Separation Membranes. *J. Mater. Chem. A* **2013**, *1* (35), 10403–10411.

(37) Nady, H.; El-Rabiei, M. M.; El-Hafez, G. M. A. Electrochemical Oxidation Behavior of Some Hazardous Phenolic Compounds in Acidic Solution. *Egypt. J. Pet.* **2017**, *26* (3), 669–678.

(38) Patil, N.; Cordella, D.; Aqil, A.; Debuigne, A.; Admassie, S.; Jérôme, C.; Detrembleur, C. Surface- and Redox-Active Multifunctional Polyphenol-Derived Poly(Ionic Liquid)s: Controlled Synthesis and Characterization. *Macromolecules* **2016**, *49* (20), 7676–7691.

(39) Patil, N.; Aqil, M.; Aqil, A.; Ouhib, F.; Marcilla, R.; Minoia, A.; Lazzaroni, R.; Jérôme, C.; Detrembleur, C. Integration of Redox-Active Catechol Pendants into Poly(Ionic Liquid) for the Design of High-Performance Lithium-Ion Battery

Cathodes. *Chem. Mater.* **2018**, *30* (17), 5831–5835.

(40) Lacey, M. J. Influence of the Electrolyte on the Internal Resistance of Lithium−Sulfur Batteries Studied with an Intermittent Current Interruption Method. *ChemElectroChem* **2017**, *4* (8), 1997–2004.

(41) Waag, W.; Käbitz, S.; Sauer, D. U. Experimental Investigation of the Lithium-Ion Battery Impedance Characteristic at Various Conditions and Aging States and Its Influence on the Application. *Appl. Energy* **2013**, *102*, 885–897.

(42) Zhang, S. S.; Jow, T. R.; Amine, K.; Henriksen, G. L. LiPF6-EC-EMC Electrolyte for Li-Ion Battery. *J. Power Sources* **2002**, *107* (1), 18–23.

(43) Dahbi, M.; Ghamouss, F.; Tran-Van, F.; Lemordant, D.; Anouti, M. Comparative Study of EC/DMC LiTFSI and LiPF6 Electrolytes for Electrochemical Storage. *J. Power Sources* **2011**, *196* (22), 9743–9750.

(44) Liang, H.; Zuo, X.; Zhang, L.; Huang, W.; Chen, Q.; Zhu, T.; Liu, J.; Nan, J. Nonflammable LiTFSI-Ethylene Carbonate/1,2-Dimethoxyethane Electrolyte for High-Safety Li-Ion Batteries. *J. Electrochem. Soc.* **2020**, *167* (9), 090520.

(45) Ha, T. A.; Li, H.; Wang, X.; O'Dell, L. A.; Forsyth, M.; Pozo-Gonzalo, C.; Howlett, P. C. Functional Binders Based on Polymeric Ionic Liquids for Sodium Oxygen Batteries Using Ionic Liquid Electrolytes. *ACS Appl. Energy Mater.* **2021**, *4* (1), 434–444.

(46) Vicente, N.; Haro, M.; Cíntora-Juárez, D.; Pérez-Vicente, C.; Tirado, J. L.; Ahmad, S.; Garcia-Belmonte, G. LiFePO4 Particle Conductive Composite Strategies for Improving Cathode Rate Capability. *Electrochim. Acta* **2015**, *163*, 323–329.

(47) Suarez-Hernandez, R.; Ramos-Sánchez, G.; Santos-Mendoza, I. O.; Guzmán-González, G.; González, I. A Graphical Approach for Identifying the Limiting Processes in Lithium-Ion Battery Cathode Using Electrochemical Impedance

Spectroscopy. *J. Electrochem. Soc.* **2020**, *167* (10), 100529.

(48) Cheng, Q. Porous Graphene Sponge Additives for Lithium Ion Batteries with Excellent Rate Capability. *Sci. Rep.* **2017**, *7* (1), 1–11.

(49) Tomé, L. C.; Isik, M.; Freire, C. S. R.; Mecerreyes, D.; Marrucho, I. M. Novel Pyrrolidinium-Based Polymeric Ionic Liquids with Cyano Counter-Anions: HIGH Performance Membrane Materials for Post-Combustion CO2 Separation. *J. Memb. Sci.* **2015**, *483*, 155–165.

(50) Zhou, X.; Pan, Z.; Han, X.; Lu, L.; Ouyang, M. An Easy-to-Implement Multi-Point Impedance Technique for Monitoring Aging of Lithium Ion Batteries. *J. Power Sources* **2019**, *417* (November 2018), 188–192. 2018), 188–192.

Chapter 3. Single lithium-ion conducting polymers with high ionic conductivity based on borate pendant groups

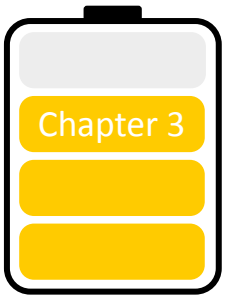

3.1. Introduction

Single lithium-ion conducting polymer electrolytes (SLICPEs) have been proposed as one promising solid electrolyte solution to overcome premature failures in solid-state lithium metal batteries [1,2]. Single-ion conductors show the limited formation of ionic concentration gradients in the electrolyte which avoids dendritic growth in the lithium anode surface [3,4]. Unlike classical solid polymeric electrolytes (SPEs) based on lithium salts dissolved in polymeric matrices such as PEO [5], in SLICPEs the anion moiety is chemically attached to the polymeric backbone and only the lithium counter-cations are fully mobile. As a consequence, single-ion conductors show typically high lithium transference numbers (LTNs) (close to unity) than those observed in dual-ion conduction SPEs (between 0.2 and 0.5) [6]. However, they typically show low ionic conductivity values vs typical dual ion polymer electrolytes due to reduced concentration of free ionic species and the limited mobility of lithium cation vs mobile anions.

To date, several polymer chemistries have been proposed and explored for the preparation of single-ion polymer electrolytes. In most cases, the anionic functional

groups attached to the polymer backbones are carboxylates, sulfonates [7], sulfonamides, or tetrahedral borates [8,9]. It has been observed that fixed anions with high charge delocalization are preferred to obtain high ionic conductivity since the ionic association with the lithium ions is weakened and the mobility of lithium cation is improved [10]. The highest ionic conductive polymers are obtained with anions like sulphonamides or tetrahedral borates which have reported ionic conductivity values less than 1×10^{-6} S.cm^{-1}, e.g. PLiMTFSI [11,12], and PSTFSI [13,14] with 1×10^{-12}, and 7.6×10^{-6} S.cm^{-1} at 25°C, respectively. Those values of ionic conductivity in homopolymers remain low for proper battery operation. For this reason, ionic transport and the ionic conductivity values are increased by formulation of the SLIPCE with plasticizers [2,15], blending with flexible polymeric matrices such as PEO [16] or block copolymerization [17,18,19].

The main objective of this work is to report the synthesis of an innovative family of anionic monomers based on a highly delocalized asymmetric borate group and their homopolymers which shows very high ionic conductivity for a single-ion polymer electrolyte. To study in-depth the effect of different substituents on ionic conductivity by changing the size and electron-withdrawing groups. The single-ion polymer electrolytes with optimized ionic conductivity are selected for lithium transference number measurements and battery tests.

In **Figure 3.1**, the general scheme of the methacrylic borate lithium salts and a picture of the polymer electrolyte membrane is presented. The chemical structures of these polymerizable lithium borate salts ware designed to integrate a poly(ethoxy methacrylate) group, a butyl group via a (B-C-) linkage, and two oxyls (B-OR) substituents; which serve

as flexible polymerizable arm, agent to stabilization-decreasing hygroscopicity [20,21], and modulation of the electron-withdrawing capacity of the borate groups [22], respectively.

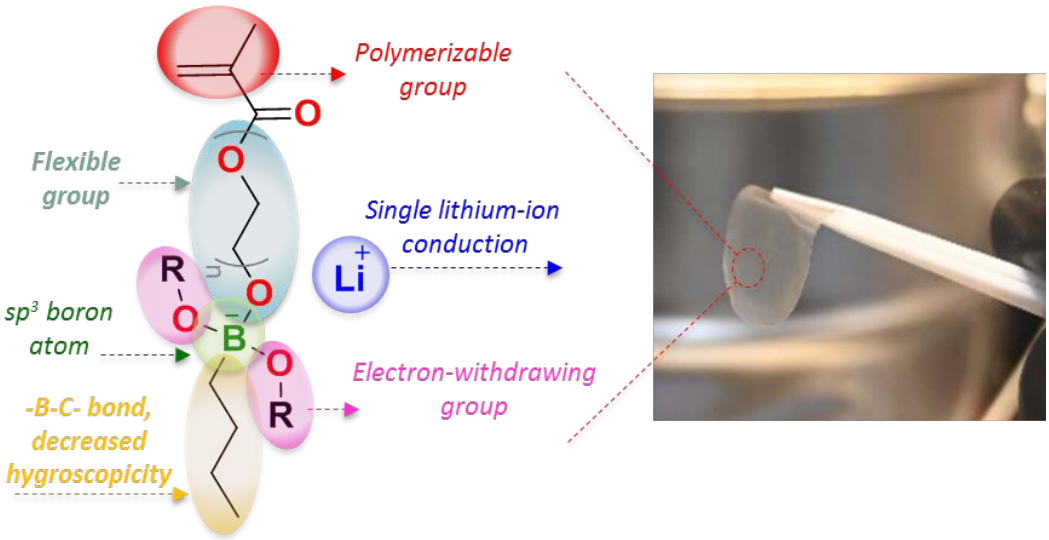

Figure 3.1. Design strategy for the borate lithium monomers and image of a homopolymer electrolyte membrane.

3.2. Polymer synthesis and characterizations

3.2.1. Synthesis of monomers and their polymerizations

The methacrylic borate SLICPEs studied in this chapter were synthesized following the three steps shown in **Figure 3.2a**. Different ethoxy methacrylate groups were chosen: 2-hydroxyethyl methacrylate (HEMA) to have one ethoxy repeating unit (n_1), and poly(ethylene glycol) methacrylate with different molecular weights to have seven and nine ethoxy repeating units (n_7, and n_9 respectively). The first step of the synthesis involves the covalent bonding of the ethoxy methacrylate group to the boron atom by a -C-O-B- bond. This step is carried out by two different methods, named A and B detailed in **Figures 3.2b** and **3.2c** respectively. Method A allows the synthesis of $BMn(OR)_2$ in one step by using Tri-R borates as reagents where the R substituents of interest are already bonded to the boron. The method A is used to synthesize the seven SLICPEs with R as aliphatic substituents (methyl, ethyl, and isopropyl): $pLBBn_1(OMe)_2$, $pLBBn_1(OEt)_2$, $pLBBn_1(OiP)_2$, $pLBBn_7(OMe)_2$, $pLBBn_7(OEt)_2$, $pLBBn_7(OiP)_2$, $pLBBn_9(OMe)_2$. Method B split the one-step of method A into two steps; it is used for reagents where the interesting R substituents are not bonded to the boron. The two steps consist of adding borane to obtain the bond with the boron atom as -C-O-BH_2, then adding the alcohol R-OH to obtain the two desired -O-R substituents in the form $BMn(OR)_2$.

In the second stage (**Figure 3.2a**), nBuLi is added to the boron atom to give rise to the formation of the boron-lithium salts of the form $LBBn(OR)_2$, generating a covalent bond (-C-B-). Finally, in the last stage, the different monomers were polymerized by a conventional free radical polymerization method adding 2,2´-Azobisisobutyronitrile (AIBN) as an initiator (3 wt.%) into a system bubbled with a flow of argon at 60 ºC and

the solution was stirred for 6 h. After the reaction, the polymers were dried on a rotary evaporator and under vacuum at 60 °C for 24 h and stored in the glove box.

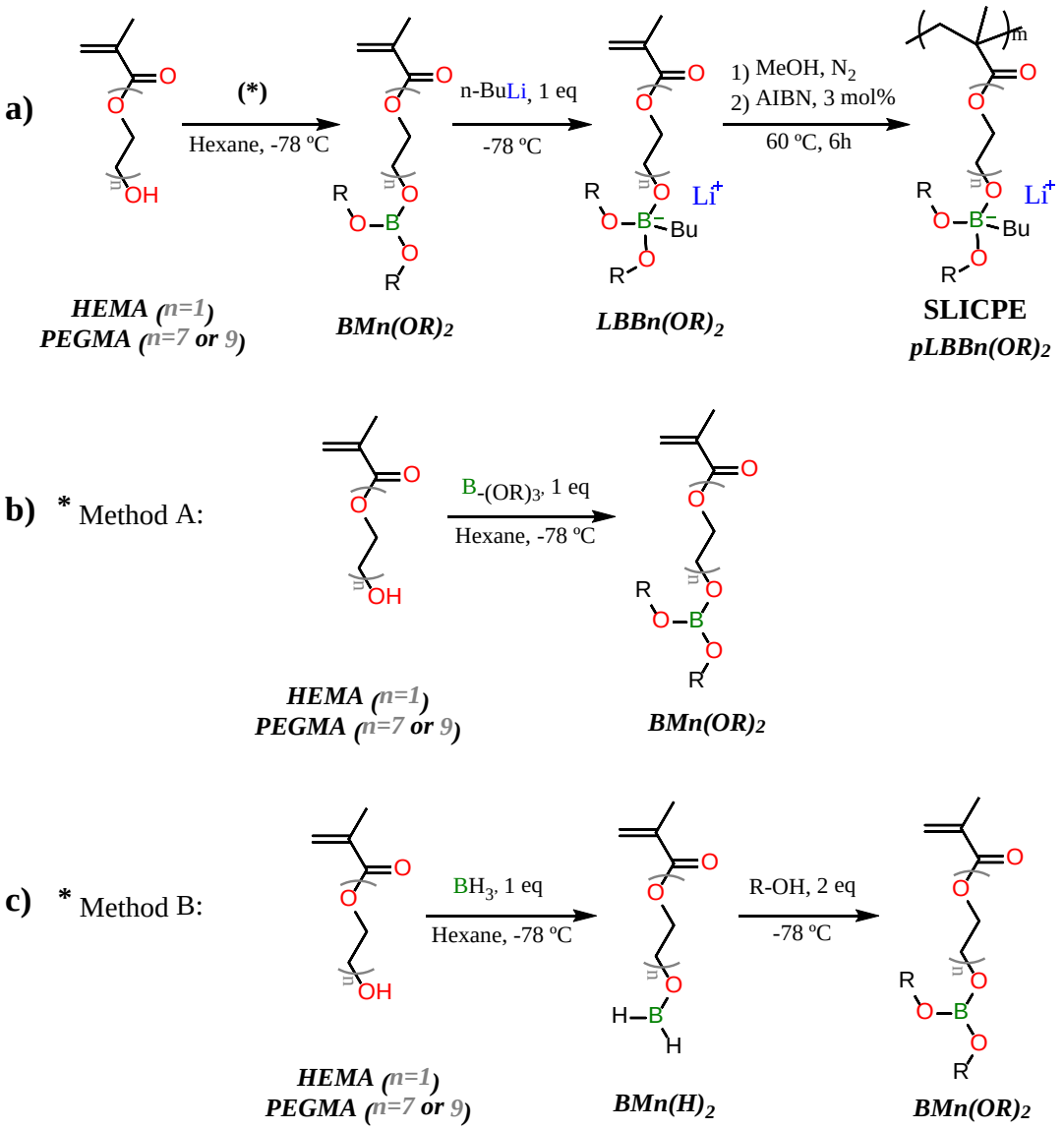

Figure 3.2. a) Synthetic routes for the general preparation of *pLBB(OR)₂*, and the two synthetic routes to prepare *BMn(OR)₂* following the b) method A, and c) method B.

All synthesized polymers are summarized in **Table 3.1** with their corresponding name. They are classified into four categories of borate polymers created according to the chemical characteristics of the substituents such as aliphatic, fluorinated, self-solvating [4,23] and the last group includes a fluorinated substituent and an ethylene glycol one as shown in **Figure 3.3**.

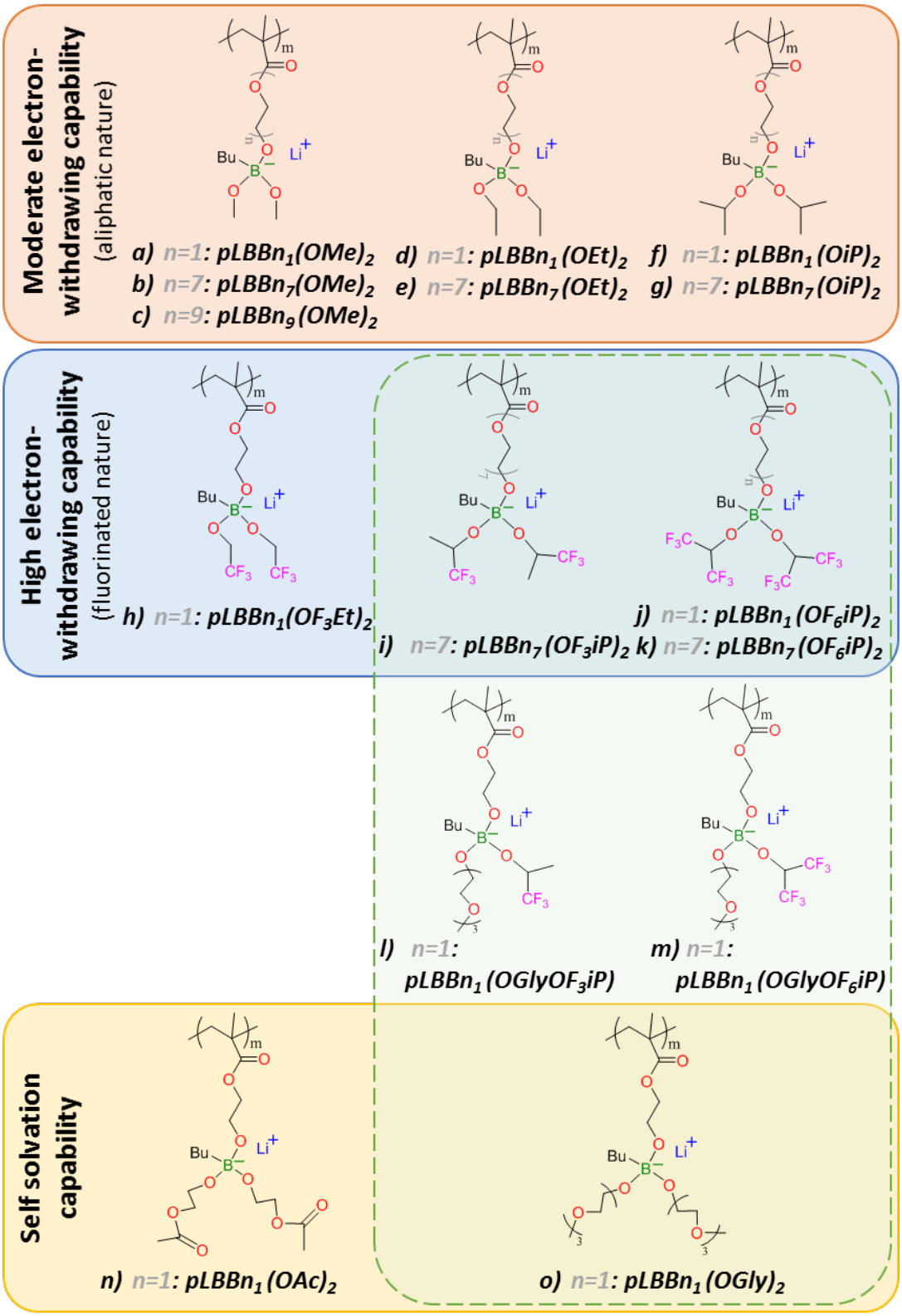

Figure 3.3. The chemical structures of synthesized SLICPEs in this chapter.

3.2.2. Structure characterizations

Each synthesized monomer and polymer was studied by NMR and FTIR to confirm their chemical structures. As an example, **Figure 3.4** shows the ^{1}H NMR and FTIR spectra with peak assignment for the monomer $LBBn_7(OMe)_2$ in blue and polymer $pLBBn_7(OMe)_2$ in red.

All monomers and polymers present similar signals in ^{1}H NMR spectra (**Figure 3.4a**) such as the butyl group bonded to the boron atom in the region of 0.5 to 1.8 ppm, the methyl and polyethylene oxide of the methacrylate group around 1.7 and 3.5-3.7 ppm respectively. Depending on the oxide substituents bound to the boron, the NMR signal is different, and in the context of our example, it is the methyl group found at 2.5 and 2.8 ppm. The typical markers of methyl methacrylate monomers are the double singlets between 5.2 and 6.2 ppm corresponding to the methylene group, which are absent for the polymers confirming the total polymerization in addition to the methyl signal around 1.2 ppm.

The FTIR spectra (**Figure 3.4b**) show similar peaks for monomers and polymers corresponding to the alkane groups between 2800 and 3000 cm^{-1} and for carbonyl groups at 1710 cm^{-1}. Besides, the peak corresponding to the alkene groups at 1635 cm^{-1}, is present for the monomers and absent for the polymers, which once again confirms the success of the total polymerization.

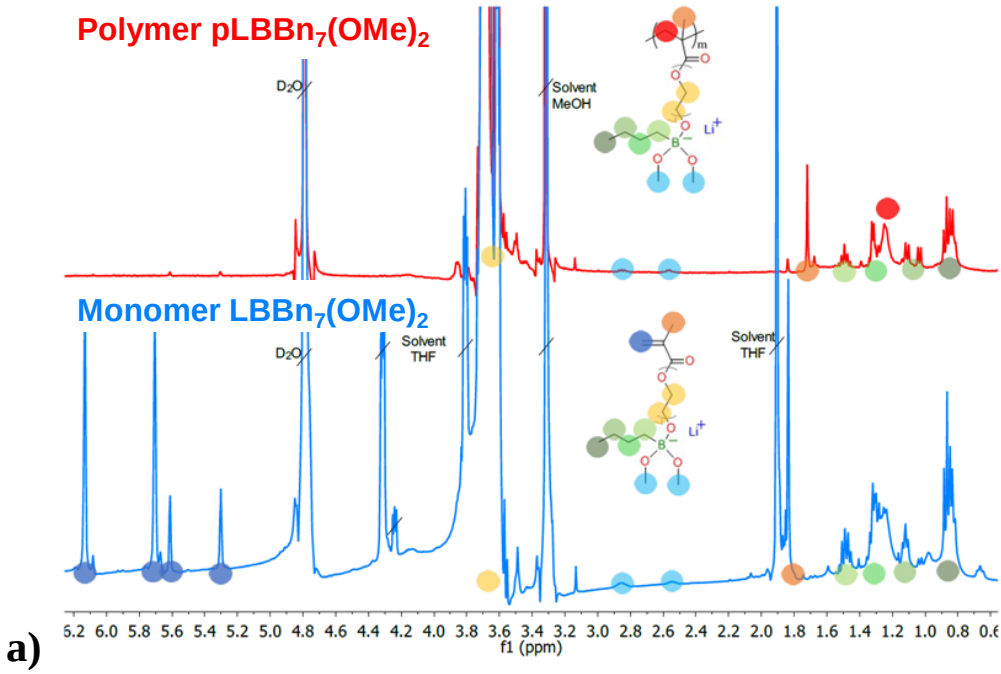

a)

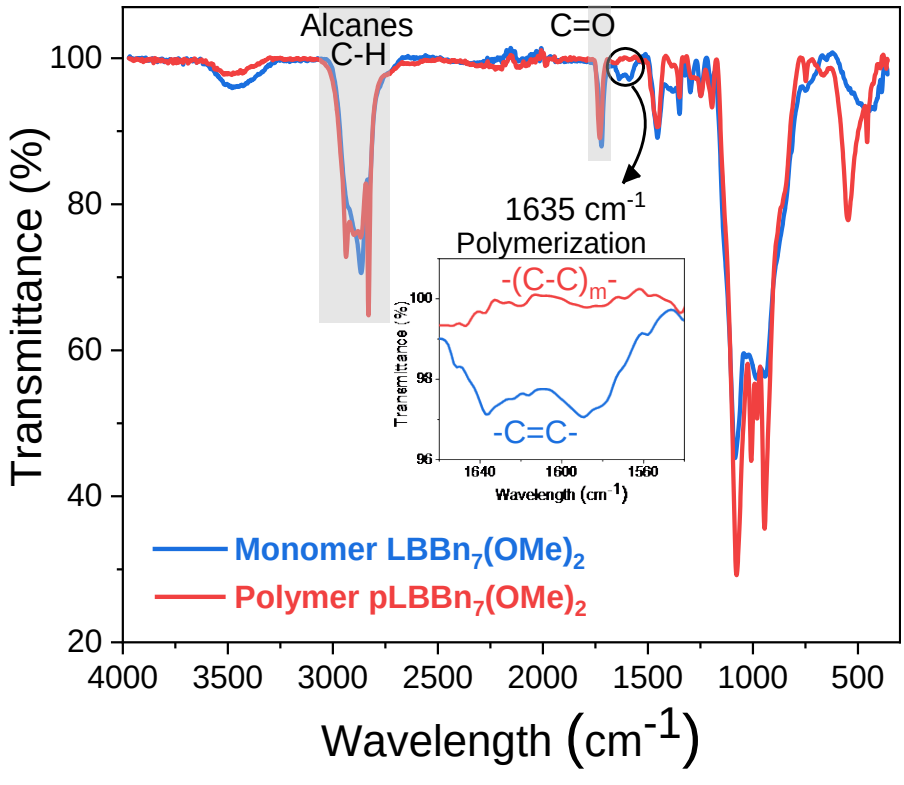

b)

Figure 3.4. a) ^{1}H NMR spectra in D_2O, and
b) FTIR spectra for monomer $LBBn_7(OMe)_2$ and polymer $pLBBn_7(OMe)_2$.

Figure 3.5a shows the NMR spectra for pLBBn$_1$(OF$_6$iP)$_2$, pLBBn$_1$(OGlyOF$_6$iP), and pLBBn$_1$(OGly)$_2$ polymers. In general, the assignment of peaks in the ^{1}H NMR spectra follows the previous explanations. The signals associated with the butyl group, the butyl group, the methylene, and the methyl product of the polymerization were noticed by the decrease of the ratio of these signals to the rest of the signals as a function of the ethoxy groups of oligomeric chains in each of the spectra. These protons are located in the region of 3.1 to 3.7 ppm and overlap with the signals of the protons of the CH_2 groups of the ethoxy ethyl methacrylate in the case of the polymers with ethylene glycol chains. The septet with a chemical shift at 4.6 ppm for pLBBn$_1$(OF$_6$iP)$_2$ is associated with the unprotected carbon-alpha proton of the (1,1,1,3,3,3-hexafluoropropan-2-yl)oxy. The septet shows a decrease in intensity and a slight shift to the high field (4.5 ppm) for the SLICPE pLBBn$_1$(OGlyOF$_6$iP) due to the effect of the addition of (methoxy tetra ethylene glycol) as a substituent.

The same effect is observed for pLBBn$_7$(OiP)$_2$, pLBBn$_7$(OF$_3$iP)$_2$, and pLBBn$_7$(OF$_6$iP)$_2$ polymers shown in spectra in **Figure 3.5b**. The septet with a chemical shift at 4.7 ppm for pLBBn$_7$(OF$_6$iP)$_2$ associated with the unprotected carbon-alpha proton of the (1,1,1,3,3,3-hexafluoropropan-2-yl)oxy, shows a decrease in intensity and a shift to the high field (4.2 ppm) due to the effect of substitution of three fluorine atoms by hydrogens as a substituent in the SLICPE pLBBn$_7$(OF$_3$iP). This behavior is even more pronounced for the SLICPE pLBBn$_7$(OiP)$_2$ which all fluorine atoms are substituted by hydrogens, the septet is shifted to 4.0 ppm.

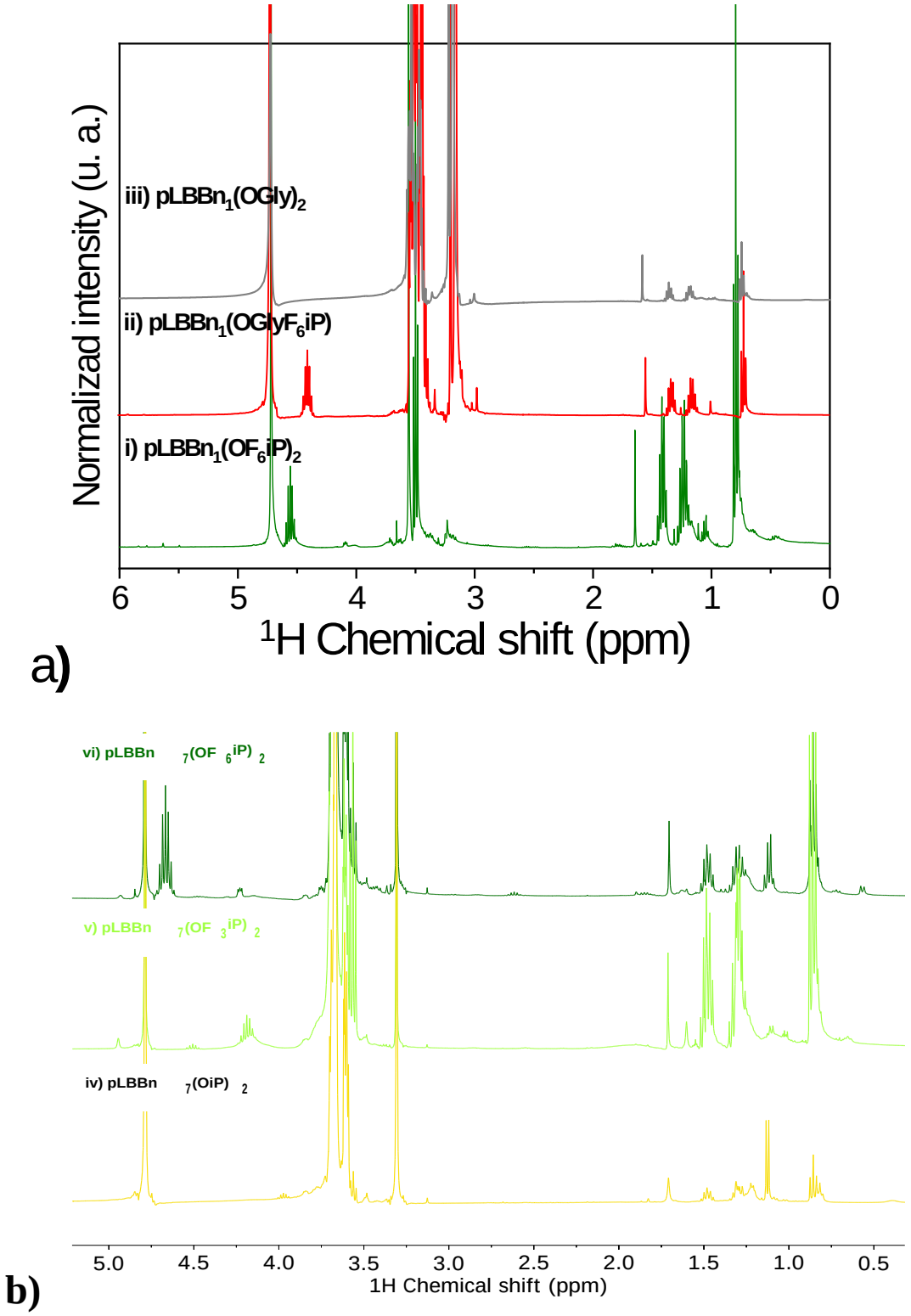

Figure 3.5. ^{1}H NMR spectra a) for synthesized n_1 SLICPEs: i) pLBBn$_1$(OF$_6$iP)$_2$, ii) pLBBn$_1$(OGlyOF$_6$iP), and iii) pLBBn$_1$(OGly)$_2$; b) for synthesized n_7 SLICPEs: iv) pLBBn$_7$(OiP)$_2$, v) pLBBn$_7$(OF$_3$iP)$_2$, and vi) pLBBn$_7$(OF$_6$iP)$_2$.

In addition to ^{1}H NMR analysis, ^{11}B, and ^{19}F NMR spectra were studied to complement the analysis of the chemical structure of polymers and to elucidate the effect of the different electron-withdrawing groups on the electron density of the borate group. The ^{11}B NMR spectra for the SLICPEs pLBBn$_1$(OF$_6$iP)$_2$, pLBBn$_1$(OGlyOF$_6$iP), and pLBBn$_1$(OGly)$_2$ (**Figure 3.6a**) present a unique signal associated with the tetra coordinated boron atoms [24], with chemical shifts of 8, 6 and 4 ppm respectively, where the high chemical shift implies a higher degree of deprotection and decrease of the electron density of the central boron atom of the anionic groups, clearly influenced by the electron-withdrawing capacity of substituent groups. In the same way, the ^{11}B NMR

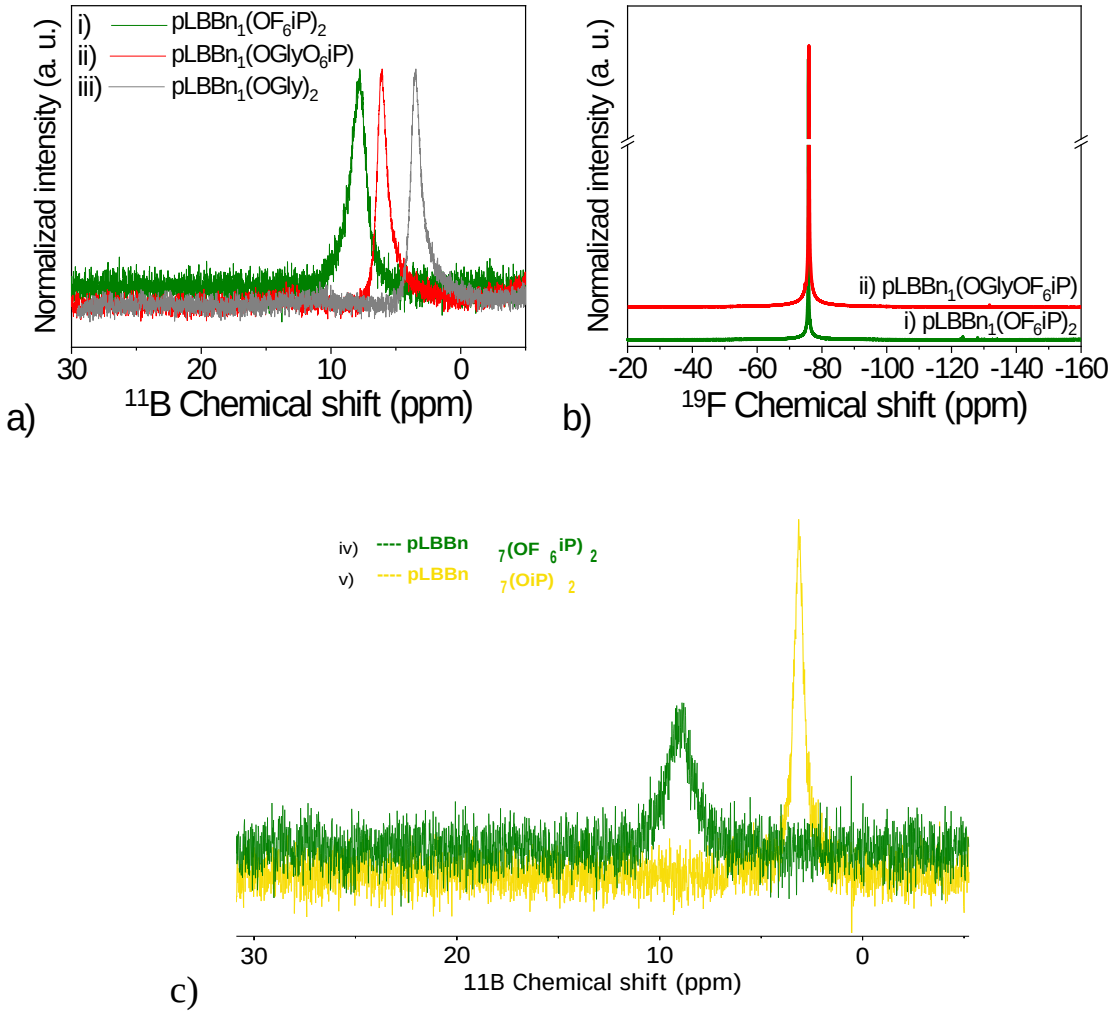

Figure 3.6. a) ^{11}B NMR spectra and b) ^{19}F NMR spectra for synthesized n$_1$ SLICPEs: i) pLBBn$_1$(OF$_6$iP)$_2$, ii) pLBBn$_1$(OGlyOF$_6$iP), and iii) pLBBn$_1$(OGly)$_2$; and c) ^{11}B NMR spectra for synthesized n$_7$ SLICPEs: iv) pLBBn$_7$(OF$_6$iP)$_2$, and v) pLBBn$_7$(OiP)$_2$.

spectra for the SLICPEs pLBBn$_7$(OF$_6$iP)$_2$, and pLBBn$_7$(OiP)$_2$ (**Figure 3.6c**) shows identical unique signal with chemical shifts of 8, and 3 ppm respectively with the same influence effect by the electron-withdrawing capacity of substituent groups as explained before. Corroborating that the incorporation of fluorinated groups as substituents promotes the delocalization of the anionic charge of the boron atom. And the ^{19}F NMR spectra show the high purity for pLBBn$_1$(OF$_6$iP)$_2$ and pLBBn$_1$(OGlyOF$_6$iP) compounds in **Figure 3.6b**.

3.2.3. Thermal analysis

TGA and DSC were used to determine the T_d and T_g of synthesized SLICPEs respectively. The values summarized in **Table 3.1** show T_d above 88 ºC confirming that SLICPEs are good candidates for solid electrolytes for batteries tested at 60 ºC. The T_g increases with the steric hindrance of the side groups as observed comparing T_g for the n$_1$ SLICPEs such as pLBBn$_1$(OGly)$_2$ and pLBBn$_1$(OGlyOF$_6$iP) of -73 and -60 ºC respectively and with higher T_g for the n$_7$ SLICPEs such as pLBBn$_7$(OMe)$_2$, pLBBn$_7$(OEt)$_2$, and pLBBn$_7$(OF$_6$iP)$_2$ of -55, -50 and -40 ºC respectively. Moreover, the T_g increases when the polarity increases as observed with T_g of pLBBn$_1$(OGlyOF$_6$iP) > pLBBn$_1$(OGly)$_2$ and with T_g of pLBBn$_7$(OF$_6$iP)$_2$ > pLBBn$_7$(OMe)$_2$ or pLBBn$_7$(OEt)$_2$.

Table 3.1. Degradation temperature (T_d) and glass transition temperature (T_g).

	T_d (ºC)	**T_g (ºC)**
pLBBn$_1$(OGly)$_2$	90	-73
pLBBn$_1$(OGlyOF$_6$iP)	130	-60
pLBBn$_7$(OMe)$_2$	100	-55
pLBBn$_7$(OEt)	88	-50
pLBBn$_7$(OF$_6$iP)$_2$	103	-40

3.3. Study of ionic conductivity

The ionic conductivity of each synthesized SLICPEs was measured and the results are shown in **Figure 3.7**. According to three comparison axes discussed in the three next parts which are the SLICPEs comparing the different oxy-substituents with one ethoxy unit *pLBBn$_1$(OR)$_2$*, the SLICPEs with increasing the number of ethoxy units for methyl-oxy substituents *pLBBn(OMe)$_2$* with n_1, n_7 or n_9, and the last part presents the SLICPEs with ethoxy repeat unit optimized at n_7 for different aliphatic and fluorinated oxy substituents *pLBBn$_7$(OR)$_2$*.

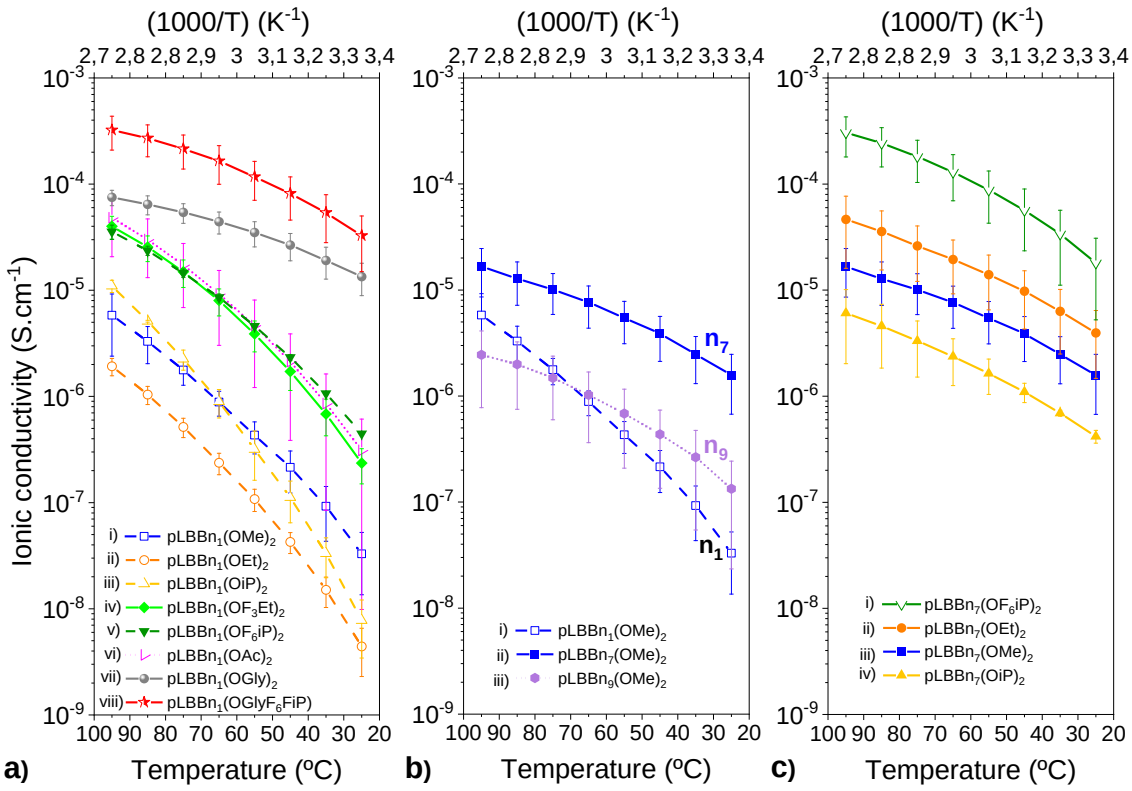

Figure 3.7. Temperature dependence of ionic conductivity for SLICPEs with a) several oxy-substituents and ethoxy unit of 1: *pLBBn$_1$(OR)$_2$*, b) OMe substituents and increasing of ethoxy unit: *pLBBn(OMe)$_2$* with n_1, n_7, and n_9, and c) several oxy-substituents and ethoxy unit of 7: *pLBBn$_7$(OR)$_2$*.

3.3.1. Effect of the different pendant groups with one ethoxy unit: n_1

The first axe of comparison targets the SLICPEs with an ethoxy unit fixed at n_1 and several oxy-substituents (*pLBBn$_1$(OR)$_2$)* (**Figure 3.7a**). To easily understand the effect of the different substituents on the ionic conduction properties, the results will be discussed in four categories of borate n_1 polymers created according to the chemical characteristics of the substituents explained in **Figure 3.7**.

First, polymers substituted with low molecular weight aliphatic groups methyl, ethyl, and isopropyl (**Figure 3.7a i-iii**): pLBBn$_1$(OMe)$_2$, pLBBn$_1$(OEt)$_2$, and pLBBn$_1$(OiP)$_2$ showed very similar and low ionic conductivity values of 3.29×10^{-8}, 4.42×10^{-9}, and 7.78×10^{-9} S.cm^{-1} at 25 °C, respectively. It is observed that ionic conductivity at low temperatures is almost not affected by the size of the substituent aliphatic groups. This behavior is maintained as a function of temperature for pLBBn$_1$(OMe)$_2$, and pLBBn$_1$(OEt)$_2$. However, pLBBn$_1$(OiP)$_2$ presents greater temperature dependence and its ionic conductivity value is slightly higher than those found for pLBBn$_1$(OMe)$_2$, probably due to the generation of conduction spaces and pathways, as a result of the movement of the larger substituent groups [25].

Second, polymers having borates with fluorinated groups as electron-withdrawing substituents show a significant increase in the ionic conductivity values (**Figure 3.7a iv-v**): pLBBn$_1$(OF$_3$Et)$_2$ and pLBBn$_1$(OF$_6$iP)$_2$. This increase in ionic conductivity was previously observed for fluorinated cross-linked polymer electrolytes due to the increased mobility of the oligomer chains in the polymeric matrix [22]. The ionic conductivity values were 4.46×10^{-7} and 2.36×10^{-7} S.cm^{-1} at 25 °C for pLBBn$_1$(OF$_3$Et)$_2$ and pLBBn$_1$(OF$_6$iP)$_2$

SLICPEs, respectively. At low temperatures, the increase in the number of fluorine atoms in the electron-withdrawing substituent groups generates a higher electronic delocalization in the anionic group, which increases the Li-ions mobility. However, at high temperatures, the sum of thermal and electronic delocalization effects that contribute to their ionic conduction processes are comparable since they present similar ionic conductivity values, 8.61×10^{-6} and 8.01×10^{-6} S.cm^{-1} at 60 °C for pLBBn$_1$(OF$_3$Et)$_2$ and pLBBn$_1$(OF$_6$iP)$_2$ polymers, respectively.

Third, the pLBBn$_1$(OAc)$_2$ polymer (**Figure 3.7a vi**), whose substituent "ethoxy acetate" groups provide self-solvating effect [23], exhibits similar characteristics of magnitude and temperature dependence that polymers with fluorinated substituents. While the SLICPE pLBBn$_1$(OGly)$_2$ (**Figure 3.7a vii**) which includes two ethoxy chains as substituent groups with an O/Li$^+$ ratio of 11, was designed and synthesized to promote the self-solvating effect of borate groups and provide pathways for ionic conduction, exhibited ionic conductivity values of 1.34×10^{-5}, and 4.42×10^{-5} S.cm^{-1} at 25, and 60 °C, respectively.

The highest ionic conductivity values were obtained for pLBBn$_1$(OGlyOF$_6$iP) homopolymer which combines a fluorinated and an ethylene glycol substituent (**Figure 3.7a viii**), with also a significant increase in thermal stability (**Table 3.1**). To our knowledge, the ionic conductivity values of 3.26×10^{-5}, and 1.64×10^{-4} S.cm^{-1} at 25, and 60 °C, respectively, are the highest reported for single Li-ion conducting homopolymers [10,14,26]. This polymer combines asymmetric substituents in its molecular structure, thus the electronic delocalization associated with the OF$_6$iP group, which allows for a decrease in the interaction energy between the Li$^+$-borate group (as explained with the **Figure**

3.6a); and the incorporation of ethylene glycol chains as ion conduction pathways, generating a synergistic effect that provides improved conditions for ionic transport.

3.3.2. Effect of increasing the ethoxy unit (n_1, n_7, and n_9)

The second axe of comparison is focused on the study of the effect of increasing the ethoxy unit (n_1, n_7, and n_9) on the ionic conduction properties. The compared SLICPEs must be composed of the same final substituents -$(OR)_2$, which are chosen by methyl-oxy substituents to have a single variable to properly assess the effect of ethoxy repeat unit length. The ionic conductivity of pLBBn$_1$(OMe)$_2$, pLBBn$_7$(OMe)$_2$, and pLBBn$_9$(OMe)$_2$ are shown in **Figure 3.7b**, and exclusively in this part for simplicity, pLBBn$_1$(OMe)$_2$, pLBBn$_7$(OMe)$_2$, and pLBBn$_9$(OMe)$_2$ will be referred to n_1, n_7, and n_9.

The highest ionic conductivity is measured for the SLICPE with intermediate ethoxy length (n_7) for all temperatures between 20 and 90 ºC. Indeed, the ionic conductivity values for n_7 were 1.58×10^{-6}, and 7.64×10^{-6} S.cm^{-1} at 25, and 60 °C respectively, whereas the values were less than 10^{-6} S.cm^{-1} for n_1 and n_9. The increase in ionic conductivity with the increase in the ethoxy repeat unit from 1 to 7 can be explained by the O/Li$^+$ ratio which increases from 5 to 11. In other words, the contribution of ethoxy groups helps the self-solvating ability of borate groups providing better ionic transport pathways with n_7 than for n_1. However, when the number of ethoxy repeat units was increased beyond 7, for example at n_9, the measured ionic conductivity was lower despite the O/Li$^+$ ratio increased to 13. In conclusion, the self-solvation capability is improved but also limited with the Li$^+$ concentration. The optimized O/Li$^+$ ratio seems to be around 11, which corresponds to a SLICPE with seven ethoxy units for the aliphatic substituents.

The activation energies (E_a) were calculated using the Arrhenius equation **(2)** and the values for the three *pLBBn(OMe)*$_2$ SLICPEs are presented in **Table 3.2**. The E_a values provide information on the strength of the Coulomb interactions and can be related to the temperature dependence of the ionic conductivity. The E_a value for n_7 and n_9 (0.136 and 0.176 respectively) are close and as shown in **Figure 3.7b**, the curves have parallel behaviors to each other in the function of the temperature, whereas E_a for n_1 (0.302 eV) is much larger and shows a very temperature dependent behavior. A reversal of the ionic conductivity trend was observed between n_1 and n_9 above 70 ºC, which shows a greater temperature dependence for n_1 with ionic conductivity values of 3.29×10^{-8} and 5.81×10^{-6} S.cm^{-1} at 25 ºC and 90 ºC respectively, whereas the ionic conductivity was more constant for n_9 with values of 1.34×10^{-7} and 2.44×10^{-6} S.cm^{-1} at 25 and 90 ºC respectively. Besides being explained by the values of E_a, this behavior is due to the same reason as that discussed with pLBBn$_1$(OiP)$_2$ and pLBBn$_1$(OMe)$_2$ previously, which is the generation of spaces and conduction pathways as a result of the movement of substituent groups compared to the proportion of the polymer. The ionic transport is through hopping between the anionic centers for n_1, whereas it is preferentially promoted by the movement of the ethoxy chains for n_7 and n_9.

Table 3.2. The activation energy for *pLBBn(OMe)*$_2$ SLICPEs with n$_1$, n$_7$, and n$_9$.

Name	$\boldsymbol{E_a}$ (eV)
pLBBn$_1$(OMe)$_2$	0.302
pLBBn$_7$(OMe)$_2$	0.136
pLBBn$_9$(OMe)$_2$	0.176

Moreover, the increase in the ethoxy repeat unit changed the appearance of the polymers such as the increase in viscosity. This effect was well observed for *pLBBn(OMe)$_2$* being a powder for n_1 to increasingly viscous solids for n_7 and n_9.

3.3.3. Effect of the different pendant groups with the ethoxy unit of n_7

Based on the previous study, where the ionic conductivity was optimized with an increase of ethoxy repeat units to 7 and 11 O/Li^+ ratios, four SLICPEs with ethoxy repeat units fixed to 7 (*pLBBn$_7$(OR)$_2$*) and different aliphatic or fluorinated substituents were compared in **Figure 3.7c**. Generally, the ionic conductivity curves are higher for the four SLICPEs n_7 with values of 1.58×10^{-6}, 3.95×10^{-6}, 4.18×10^{-7}, 1.80×10^{-5} S.cm^{-1} at 25 ºC for pLBBn$_7$(OMe)$_2$, pLBBn$_7$(OEt)$_2$, pLBBn$_7$(OiP)$_2$, pLBBn$_7$(OF$_6$iP)$_2$ respectively, compared to their n_1 homolog with values of 3.29×10^{-8}, 4.42×10^{-9}, 7.78×10^{-9}, 2.35×10^{-7} S.cm^{-1} at 25 ºC for pLBBn$_1$(OMe)$_2$, pLBBn$_1$(OEt)$_2$, pLBBn$_1$(OiP)$_2$, pLBBn$_1$(OF$_6$iP)$_2$ respectively (**Figure 3.7a iii,v**). Moreover, n_7 SLICPEs depend less on temperature than their n_1 counterpart and n_7 aliphatic SLICPEs follow a similar trend between them with increasing order pLBBn$_1$(OiP)$_2$ < pLBBn$_1$(OMe)$_2$ < pLBBn$_1$(OEt)$_2$.

Similar to the study of n_1 SLICPEs, the ionic conductivity is greatly improved with the fluorinated substituents for pLBBn$_7$(OF$_6$iP)$_2$. This is explained with the increase of the Li-ions mobility by electronic delocalization effect with the electron-withdrawing fluorinated substituent compared to the aliphatic ones (as explained with the **Figure 3.6c**). The ionic conductivity of pLBBn$_7$(OF$_6$iP)$_2$ with values of 1.80×10^{-5}, 1.29×10^{-4}, and 3.05×10^{-4} S.cm^{-1} at 25, 60, and 90 ºC respectively, follows very closely the ionic conductivity of pLBBn$_1$(OGlyOF$_6$iP) with values of 3.26×10^{-5}, 1.65×10^{-4}, and 3.28×10^{-4}

S cm^{-1} at 25, 60 and 90 °C respectively, which is reported as the highest ionic conductivity for single Li-ion conducting homopolymers.

3.3.4. Influence of the fluorine number

In this part, the evolution of ionic conductivity is discussed for two comparison cases of SLICPEs with different number of fluorine atoms and the same structures. In the first case, pLBBn$_1$(OGlyOF$_3$iP) and pLBBn$_1$(OGlyOF$_6$iP) are compared. The **Figure 3.8a** shows their structures and the **Figure 3.8c** their ionic conductivity results. For the second case, pLBBn$_7$(OiP)$_2$, pLBBn$_7$(OF$_3$iP)$_2$, and pLBBn$_7$(OF$_6$iP)$_2$ are shown in **Figures 8b** and **8d**.

In the first case (**Figures 3.8a** and **3.8c**), the compared SLICPEs have the same structure with small variation in the pendant isopropyl group (iP). Three hydrogen atoms on the isopropyl substituent (OiP) change to three fluorine atoms (OF$_3$iP). Thus the F/Li^+ ratio increases from 3 to 6 for pLBBn$_1$(OGlyOF$_3$iP) and pLBBn$_1$(OGlyOF$_6$iP), and the ionic conductivity values also increases, from 3.43×10^{-6} to 3.26×10^{-5} S.cm^{-1} at 25 ºC respectively. As previously explained, the ionic conductivity increases with the presence of electron-withdrawing substituent so the increase of the F/Li^+ ratio.

In the second case (**Figures 3.8b** and **3.8d**), the structures of SLICPEs are composed of two isopropyl substituents with increasing fluorine atoms, such are pLBBn$_7$(OiP)$_2$, pLBBn$_7$(OF$_3$iP)$_2$, and pLBBn$_7$(OF$_6$iP)$_2$. The F/Li^+ ratio increased from 0, 6, and 12 respectively, and the ionic conductivity values are 4.18×10^{-7}, 1.34×10^{-7}, and 1.80×10^{-5} S.cm^{-1} at 25 ºC respectively. It is worth mentioning that the increasing evolution of the ionic conductivity is pLBBn$_7$(OF$_3$iP)$_2$ < pLBBn$_7$(OiP) < pLBBn$_7$(OF$_6$iP), therefore the

ionic conductivity does not evolve following the F/Li^+ ratio. The ionic conductivity behavior of $pLBBn_7(OF_3iP)_2$ is the lowest, and even lower than $pLBBn_7(OiP)_2$. This can be explained through the charges of the three fluorine and three hydrogen atoms on the isopropyl substituent $(OF_3iP)_2$ which are balanced together and do not affect the boron charge so the interaction energy between Li^+-borate is stronger, compared to isopropyl substituents with six hydrogen atoms $(OiP)_2$ or fluorine atoms $(OF_6iP)_2$. A modeling study of ionic molecular orbitals could help to understand and validate this hypothesis.

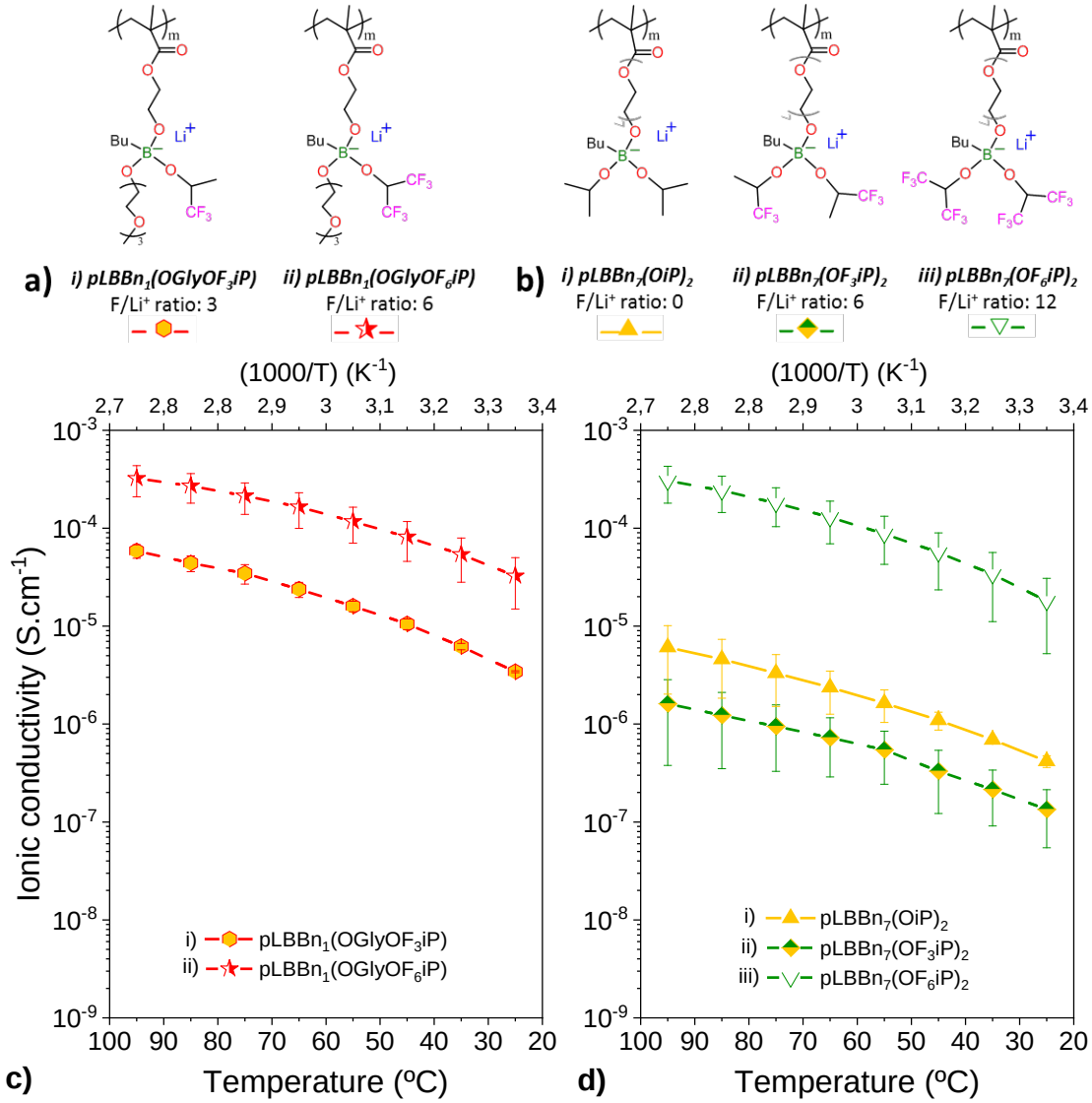

Figure 3.8. Chemical structures of SLICPEs: a) $pLBBn_1(OGlyOF_3iP)$ and $pLBBn_1(OGlyOF_6iP)$; and b) $pLBBn_7(OiP)_2$, $pLBBn_7(OF_3iP)_2$, and $pLBBn_7(OF_6iP)_2$. Temperature dependence of ionic conductivity c) for SLICPEs with 1 ethoxy group, and d) for SLICPEs with 7 ethoxy groups.

3.3.5. Other electrochemical characterizations for SLICPEs

In highly conductive SLICPEs, ionic transport is determined by the degree of super-delocalized negative charge distribution of the anionic centers, which decreases the interaction energy in the ionic pair [10]. Furthermore, generally accepted models for Li^+ transport in SPEs involving coupling to the segmental motion of the polymer backbone, a more flexible backbone is naturally beneficial for conductivity [6]. Both assumptions for the description of ionic transport in SPE are synergically combined in the molecular structure of the polymers pLBBn$_1$(OGly)$_2$, pLBBn(OGlyOF$_6$iP), pLBBn$_7$(OEt)$_2$, and pLBBn$_7$(OF$_6$iP)$_2$, resulting in high ionic conductivity values [4]. In order to verify the single lithium-ion-conducting characteristics the lithium transference number (t_{Li^+}) were measured and presented in **Figure 3.9**. The n$_1$ and n$_7$ optimized homopolymers which are pLBBn$_1$(OGly)$_2$, pLBBn$_1$(OGlyOF$_6$iP), pLBBn$_7$(OEt)$_2$, and pLBBn$_7$(OF$_6$iP)$_2$ present high t_{Li^+} values of 0.92, 0.93, 0.88, and 0.96 respectively. All t_{Li^+} values are close to 1 as expected values for single-ion polymers.

The resistance is greatly improved with viscous liquid homopolymers. Indeed, the Nyquist plots show very high resistances for the two solid SLICPEs with resistance around 75 kΩ for pLBBn$_1$(OGly)$_2$ and higher than 1000 kΩ for pLBBn$_7$(OEt)$_2$ (**inset Figures 3.9a** and **3.9c**) while the resistance is improved by a decrease of less than 3 kΩ for the two viscous liquid SLICPEs pLBBn$_1$(OGlyOF$_6$iP) and pLBBn$_7$(OF$_6$iP)$_2$ (**inset Figures 3.9b** and **3.9d**).

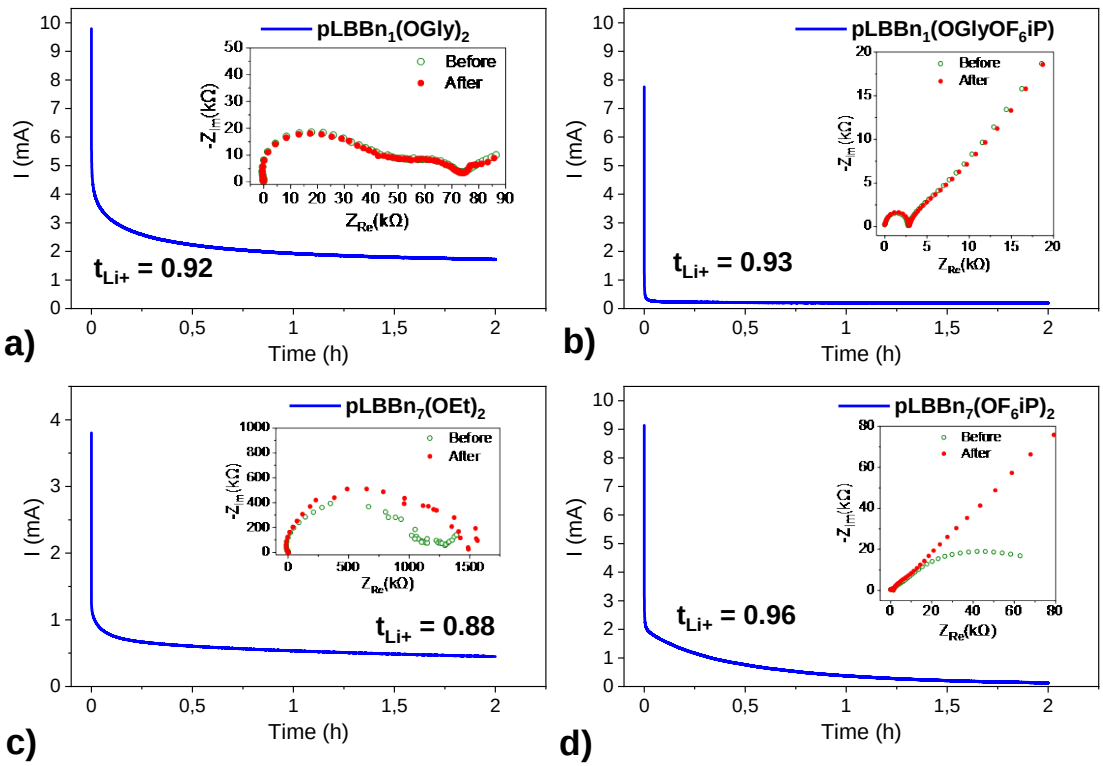

Figure 3.9. Lithium transference number (t_{Li^+}) evaluation: typical current transient obtained at the polarization of 10 mV for Li | *pLBBn(OR)*$_2$ | Li symmetrical cells at 60 °C (inset: Nyquist plot for the same cell before and after polarization) for the SLICPEs a) pLBBn$_1$(OGly)$_2$, b) pLBBn$_1$(OGlyOF$_6$iP), c) pLBBn$_7$(OEt)$_2$, and d) pLBBn$_7$(OF$_6$iP)$_2$.

Among the new proposed SLICPEs, pLBBn1(OGlyOF$_6$iP) is selected to be tested as a solid polymer electrolyte in a battery because it has the best electrochemical properties with t_{Li^+} values close to unity, resistance greatly improved, and most importantly, the highest ionic conductivity.

To evaluate the electrochemical stability of the homopolymer electrolyte pLBBn$_1$(OGlyOF$_6$iP), the cyclic voltammetry of *Li | pLBBn(OR)*$_2$ | *stainless steel* cell at 60 °C was studied and shown in **Figure 3.10**. pLBBn$_1$(OGlyOF$_6$iP) shows electrochemical stability of 4.2 V vs Li$^+$/Li confirming its excellent properties as SLIPCE for batteries.

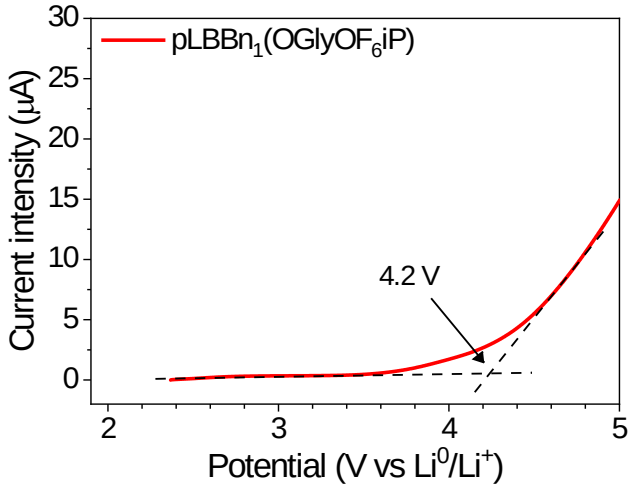

Figure 3.10. Linear sweep voltammograms (v = 0.2 mV.s^{-1}) obtained in the *Li | pLBBn$_1$(OGlyOF$_6$iP) | stainless steel* cell at 60 ºC.

3.4. Battery performances

The SLICPE pLBBn$_1$(OGlyOF$_6$iP) was tested in a full cell with $Li_4Ti_5O_{12}$ (LTO) | pLBBn$_1$(OGlyOF$_6$iP) | $LiFePO_4$ (LFP) configuration as represented in **Figure 3.11a**. The battery system is not optimized because there are no electrolytes in the anode and cathode. Therefore, the battery is first tested with a very low current as a proof of concept. The battery was charged and discharged at 60 ºC between 1.0 and 2.5 V at increasing currents of 0.04C for two cycles and 0.1C for three cycles as shown in the voltage profiles in **Figure 3.11b**. The highest capacity is 238 µA.h measured during the first charge at 0.04C and gradually decreases to 120 µA.h for the second discharge at -0.04C and finally decreases to 50-75 µA.h for the cycles at ±0.1C. The decrease capacity values is due to the charge-discharge asymmetry observed in the voltage profile by longer oxidation, well-observed at a low rate of 0.04C.

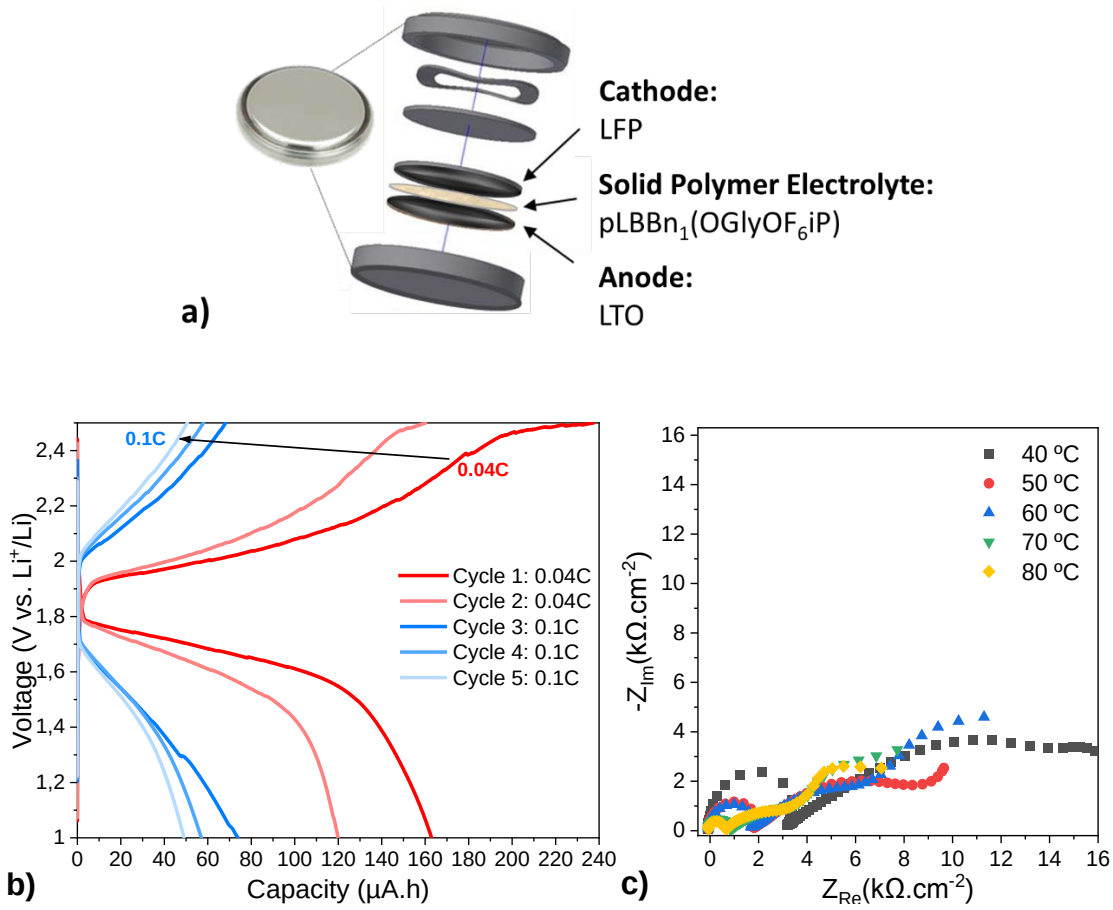

Figure 3.11. Application of SLICPEs in LTO | pLBBn$_1$(OGlyOF$_6$iP) | LFP cell: a) schematic representation of battery components; b) charge-discharge voltage profiles for several cycles at currents 0.04C, and 0.1C at 60 ºC; and c) Nyquist plots at 2.0 V for different temperatures.

The cell impedance was measured every 10 ºC, from 40 to 80 ºC, and the results are shown in **Figure 3.11c**. The impedance decreases with increasing temperature from 3.3 kΩ at 40 ºC to 0.65 kΩ at 80 ºC. However, the impedances at 50 and 60 ºC are similar with resistances of 1.8 and 1.7 kΩ respectively, likewise for the impedances at 70 and 80 ºC with resistances values of 0.7 and 0.8 kΩ, respectively.

3.5. Conclusions

In this chapter, a new family of single-ion lithium conducting polymer electrolytes based on highly delocalized borate groups is reported. Synthesis and characterizations are analyzed and thermal analysis shows good properties for battery application below 88 ºC. The effect of the nature of the substituents onto boron atoms including aliphatic, fluorinated, and self-solvating on their ionic conductivity was studied, also the effect of increasing the ethoxy repeat unit from n_1, n_7, and n_9. The optimized methacrylic borate SLIPCEs show to our knowledge the highest ionic conductivity reported for a lithium single-conduction homopolymer with 1.65×10^{-4} and 1.29×10^{-4} S cm^{-1} for $pLBBn_1(OGlyOF_6iP)$ and $pLBBn_7(OF_6iP)_2$ respectively at 60 °C. The single ion-conducting properties were confirmed by its high t_{Li^+} between 0.88 and 0.93.

The SLICPE $pLBBn_1(OGlyOF_6iP)$ was tested in battery LTO || LFP at 60 ºC and 238 µA.h of capacity was measured during the first charge at 0.04C and 1.7 kΩ of resistance. To conclude, the performance of the solid state battery is quite low due to the absence of electrolytes in the anode and cathode, but the results prove the concept and are encouraging. Indeed, this opens up many possibilities for future work, such as optimizing the battery configuration or including this monomer in co-polymer or polymer electrolyte formulations thanks to the versatility of the acrylic polymer chemistry.

3.6. Experimental part

3.6.1. Materials

All chemicals, including 2-Hydroxyethyl methacrylate (HEMA, 97%, Aldrich), Poly(ethylene glycol) methacrylate (PEGMA, molecular weight of 360 and 500 $g.mol^{-1}$, Aldrich), Borane tetrahydrofuran complex solution 1.0 M in THF (BH_3, Aldrich), n-Butyl lithium 2.5M solution in hexanes, (nBuLi, ACROS), 2,2´-Azobisisobutyronitrile (AIBN, initiator, 98%, Aldrich), Trimethyl borate (TMB, ≥98%, Aldrich), Triethyl borate (TEB, ≥95%,Aldrich), Triisopropyl borate (TiPB, ≥98%, Aldrich), 2,2,2-Trifluoroethanol (TFE, Aldrich), 1,1,1,3,3,3-Hexafluoro-2-propanol (HFiP, ≥99%, Aldrich), 1,1,1-Trifluoro-2-propanol (TFP, 97%, Aldrich), were used as received. The products 2-Hydroxyethyl Acetate (HEA, 75%, TCI), and Triethylene glycol monomethyl ether (TEG, 95%, Aldrich) were distilled at the rotary evaporator at 70°C and reduced pressure. The methanol (MeOH) and hexane solvents from SharpLab were dried with anhydrous MgSO4 before used. BH_3-THF and n-Butyl lithium are very highly moisture-sensitive reagents so they need to be handled under inert atmosphere in all steps.

3.6.2. Synthesis of the single lithium-ion monomers

The seven monomers substituted with aliphatic groups (-R) such as methyl, ethyl and isopropyl ($LBBn_1(OMe)_2$, $LBBn_7(OMe)_2$, $LBBn_9(OMe)_2$, $LBBn_1(OEt)_2$, $LBBn_7(OEt)_2$, $LBBn_1(OiP)_2$, and $LBBn_7(OiP)_2$) were synthesized following the method A as shown in **Figures 3.2a-b)**. To synthesize the three monomers $LBBn_1(OMe)_2$, $LBBn_1(OEt)_2$, and $LBBn_1(OiP)_2$, HEMA (10 mmol, 1.3 g) and dry hexane (30 ml) were charged into a flask of 100 ml. Concerning the three monomers synthesis of $LBBn_7(OMe)_2$, $LBBn_7(OEt)_2$, and $LBBn_7(OiP)_2$, PEGMA with molecular weight of 360 $g.mol^{-1}$ (10 mmol, 3.6 g) and

dry hexane (30 ml) were charged into a flask of 100 ml. And for $LBBn_9(OMe)_2$ synthesis, PEGMA with molecular weight of 500 $g.mol^{-1}$ (10 mmol, 5.0 g) and dry hexane (30 ml) were charged into a flask of 100 ml. Then the solutions were stirred with argon flow and then cooled in an acetone-liquid nitrogen bath, avoiding solidification of the system. 1 molar equivalent (1 eq.) of Tri-R borates were added dropwise according to the desired monomer. TMB (10 mmol, 1.04 ml) for $LBBn_1(OMe)_2$, $LBBn_7(OMe)_2$, and $LBBn_9(OMe)_2$ monomers synthesis. TEB (10 mmol, 1.7 ml) for $LBBn_1(OEt)_2$ and $LBBn_7(OEt)_2$ monomers synthesis. TiPB (10 mmol, 2.2 ml) for $LBBn_1(OiP)_2$ and $LBBn_7(OiP)_2$ monomers synthesis. The reaction mixtures were slowly heated to RT and stirred for 2 h. Subsequently, the systems were cooled again in an acetone-liquid nitrogen bath and 1 eq. of nBuLi 2.5 M in hexane (10 mmol, 4 ml) were added dropwise. The precipitates formed were heated to RT and stirred for another 2 h more, before being filtered and washed with cold diethyl ether. The white monomers obtained were placed in a vial and dried on a vacuum line at 40°C for 24h.

The method B shown in **Figures 3.2a** and **3.2c** was followed to synthesize the monomers $LBBn_1(OF_3Et)_2$, $LBBn_1(OF_6iP)_2$, $LBBn_7(OF_3iP)_2$, $LBBn_7(OF_6iP)_2$, $LBBn_1(OAc)_2$, $LBBn_1(OGly)_2$, $LBBn_1(OGlyOF_6iP)$, and $LBBn_1(OGlyOF_3iP)$. 30 ml of dry hexane were charged into the 100 ml two-neck flask with HEMA (10 mmol, 1.3 g) except for $LBBn_7(OF_3iP)_2$ and $LBBn_7(OF_6iP)_2$ synthesis which used PEGMA with molecular weight of 360 $g.mol^{-1}$ (10 mmol, 3.6 g). The solutions were stirred with argon flow and subsequently cooled in an acetone-liquid nitrogen bath, avoiding solidification of the system. 1 eq. of BH_3-THF complex solution of 1 M in THF (10 mmol, 10 ml) were carefully added "dropwise", while H_2 was expelled from the system with nitrogen flow. Then the reaction mixtures were slowly warmed to RT and stirred for 30 min more.

Before each addition of the next reagents, the systems were cooled in an acetone-liquid nitrogen bath, and afterward, the systems were heated to RT for 1 hour to ensure that H_2 releases were complete. 2 eq. of alcohols according to the desired monomer were added dropwise such as TFE (20 mmol, 4 ml) for $LBBn_1(OF_3Et)_2$; HFiP (20 mmol, 4 ml) for $LBBn_1(OF_6iP)_2$ and $LBBn_7(OF_6iP)_2$; TFP (20 mmol, 4 ml) for $LBBn_7(OF_3iP)_2$; HEA (20 mmol, 4 ml) for $LBBn_1(OAc)_2$; and TEG (20 mmol, 4 ml) for $LBBn_1(OGly)_2$. For $LBBn_1(OGlyOF_6iP)$ and $LBBn_1(OGlyOF_3iP)$, two different alcohols were added dropwise separately: first, 1 eq. of TEG (10 mmol, 4 ml), and secondly, 1 eq. of HFiP for $LBBn_1(OGlyOF_6iP)$ or TFP (10 mmol, 4 ml) for $LBBn_1(OGlyOF_3iP)$. Finally, for each synthesis, 1 eq. of nBuLi 2.5 M in hexane (10 mmol, 4 ml) was added dropwise following the same temperature control protocol. The reaction mixture was stirred at RT for another 2 hours. Finally, the product was precipitated and washed with cold diethyl ether. The monomers obtained were placed in a vial and dried in a vacuum line at 40°C for 24h.

3.6.3. Polymerization procedure

The synthesized boron-based monomers were used to obtain a series of SLICPEs using the random radical polymerization method. The following example describes the procedure used for the synthesis of the linear polymer $pLBBn_1(OMe)_2$: $LBBn_1(OMe)_2$ monomer (0.95 g), AIBN (0.0040 g, 3 wt%), and methanol (0.40 ml) were gently mixed in a Schlenk tube at RT. To remove as much oxygen as possible, the system was bubbled for 3 min with a flow of argon and an additional 30 min after the reagents were added. The reaction flask was then immersed in a hot oil bath at 60°C and left for 6h. After the reaction, the polymers were dried on a rotary evaporator and finally, thoroughly dried at 60 °C under a high vacuum for 24 h and stored in the glove box. The monomers *$LBBn_1(OR)_2$*, *$LBBn_7(OR)_2$* and *$LBBn_9(OR)_2$* were used for obtaining *$pLBBn_1(OR)_2$*,

pLBBn$_7$(OR)$_2$ and *pLBBn$_9$(OR)$_2$* SLICPEs following the same polymerization method described above and all polymer structures and names are summarized in **Table 3.3**.

The obtained polymers pLBBn$_1$(OMe)$_2$, pLBBn$_1$(OEt)$_2$, pLBBn$_1$(OiP)$_2$, pLBBn$_1$(OF$_3$Et)$_2$, and pLBBn$_1$(OF$_6$iP)$_2$ were white solid; pLBBn$_7$(OMe)$_2$, pLBBn$_7$(OEt)$_2$, pLBBn$_7$(OiP)$_2$, pLBBn$_9$(OMe)$_2$, pLBBn$_7$(OF$_3$iP)$_2$, pLBBn$_1$(OGly)$_2$, pLBBn$_1$(OGlyOF$_3$iP) were gels; and pLBBn$_7$(OF$_6$iP)$_2$, pLBBn$_1$(OGlyOF$_6$iP), pLBBn$_1$(OAc)$_2$ were viscous liquids.

Table 3.3. Chemical structures and names of SLICPEs.

Structure	n	Name	Full name
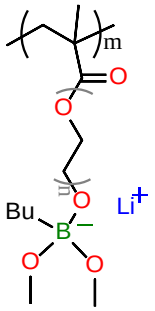	1	***pLBBn$_1$(OMe)$_2$***	*poly(lithium butyl(2-((dimethoxyboryl) oxy)ethyl methacrylate))*
	7	***pLBBn$_7$(OMe)$_2$***	*poly(lithium butyl(2-((dimethoxyboryl) (poly(ethylene glycol) methacrylate))))*
	9	***pLBBn$_9$(OMe)$_2$***	*poly(lithium butyl(2-((dimethoxyboryl) (poly(ethylene glycol) methacrylate))))*
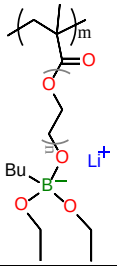	1	***pLBBn$_1$(OEt)$_2$***	*poly(lithium butyl(2-((diethoxyboryl)oxy)ethyl methacrylate))*
	7	***pLBBn$_7$(OEt)$_2$***	*poly(lithium butyl(2-((diethoxyboryl) (poly(ethylene glycol) methacrylate))))*
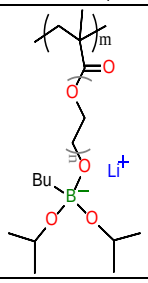	1	***pLBBn$_1$(OiP)$_2$***	*poly(lithium butyl(2-((diisopropoxyboryl) oxy)ethyl methacrylate))*
	7	***pLBBn$_7$(OiP)$_2$***	*poly(lithium butyl(2-((diisopropoxyboryl) (poly(ethylene glycol) methacrylate))))*

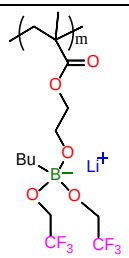	1	***pLBBn$_1$(OF$_3$Et)$_2$***	*poly(lithium butyl(2-((bis(2,2,2-trifluoroethoxy)boryl)oxy)ethyl methacrylate))*
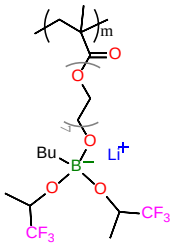	7	***pLBBn$_7$(OF$_3$iP)$_2$***	*poly(lithium butyl(2-((bis(1,1,1-trifluoropropan-2-yl)boryl)oxy)(poly(ethylene glycol)methacrylate)))*
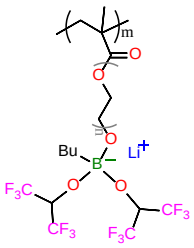	1	***pLBBn$_1$(OF$_6$iP)$_2$***	*poly(lithium butyl(2-((bis(1,1,1,3,3,3-hexafluoropropan-2-yl)boryl)oxy)ethyl methacrylate))*
	7	***pLBBn$_7$(OF$_6$iP)$_2$***	*poly(lithium butyl(2-(bis(1,1,1,3,3,3-hexafluoropropan-2-yl)boryl)(poly(ethylene glycol) methacrylate)))*
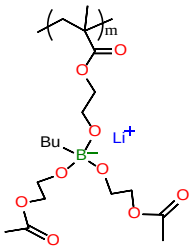	1	***pLBBn$_1$(OAc)$_2$***	*poly(lithium butyl(2-((bis(ethane-2,1-diyl)diacetate)boryl)oxy)ethyl methacrylate))*
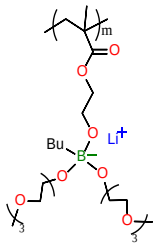	1	***pLBBn$_1$(OGly)$_2$***	*poly(lithium butyl(2-(2-(2-methoxyethoxy)ethoxy)ethyl)boryl)oxy)ethyl methacrylate))*
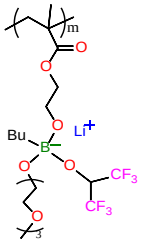	1	***pLBBn$_1$(OGlyOF$_6$iP)***	*poly(lithium butyl((2-((2-(1,1,1,3,3,3-hexafluoropropan-2-yl))(2-(2-(2-methoxyethoxy)ethoxy)ethyl))boryl)oxy)ethyl methacrylate))*
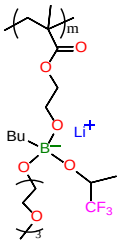	1	***pLBBn$_1$(OGlyOF$_3$iP)***	*poly(lithium butyl((2-(((1,1,1-trifluoropropan-2-yl))(2-(2-(2-methoxyethoxy)ethoxy)ethyl))boryl)oxy)ethyl methacrylate)*

3.6.4. Polymer material characterizations

Chemical structure characterizations were investigated by FTIR and NMR spectrometry for the monomers before the polymerization and for the final boron based polymers. FTIR (Nicolet 6700 FTIR spectrometer over the range of 4000-400 cm^{-1}) were used at RT and under air atmosphere. ^{1}H, ^{19}F, and ^{11}B NMR spectroscopy analysis were carried out with the Avance III 400 MHz Digital NMR spectrometer. The NMR results for the polymers is reported below:

pLBBn$_1$(OMe)$_2$, Yield: 0.9 g (97%); ^{1}H NMR (400 MHz, D_2O): δ (ppm) = 3.75-3.44 (dt, 4H, CO-O-$\underline{CH_2}$-$\underline{CH_2}$-O-B), 3.24 (s, 6H, B-O-$\underline{CH_3}$), 1.72 (s, 3H, CH_2-C($\underline{CH_3}$)-CH_2), 1.49 (q, 2H, B-$\underline{CH_2}$-CH_2-), 1.32 (sx, 4H, B-CH_2-$\underline{CH_2}$-CH_2), 1.24 (br, 2H, -($\underline{CH_2}$-C(CH_3))-), 0.87 (t, 3H, $(CH_2)_3$-$\underline{CH_3}$); ^{11}B NMR (400 MHz, D_2O): δ (ppm) = 8.2 (s, -CH_2-$\underline{B}$-$(OR)_2$).

pLBBn$_1$(OEt)$_2$, Yield: 1.25 g (91%); ^{1}H NMR (400 MHz, D_2O): δ (ppm) = 3.63-3.56 (dt, 4H, CO-O-$\underline{CH_2}$-$\underline{CH_2}$-O-B), 3.31 (c, 4H, B-O-$\underline{CH_2}$), 1.71 (s, 3H, CH_2-C($\underline{CH_3}$)-CH_2), 1.48 (q, 2H, B-$\underline{CH_2}$-CH_2-), 1.29 (sx, 2H, B-CH_2-$\underline{CH_2}$-CH_2), 1.21 (br, 2H, -($\underline{CH_2}$-C(CH_3))-), 1.14 (t, 6H, B-O-CH_2-$\underline{CH_3}$), 0.86 (q, 4H, B-$(CH_2)_3$-$\underline{CH_3}$); ^{11}B NMR (400 MHz, D_2O): δ (ppm) = 8.2 (s, -CH_2-$\underline{B}$-$(OR)_2$).

pLBBn$_1$(OiP)$_2$, Yield: 1.08 g (87%); ^{1}H NMR (400 MHz, D_2O): δ (ppm) = 3.98 (m, 2H, B-O-$\underline{CH}(CH_3)_2$), 3.67-3.56 (dt, 4H, CO-O-$\underline{CH_2}$-$\underline{CH_2}$-O-B), 1.71 (s, 3H, CH_2-C($\underline{CH_3}$)-CH_2), 1.49 (q, 2H, B-$\underline{CH_2}$-CH_2-), 1.30 (sx, 3H, B-CH_2-$\underline{CH_2}$-CH_2), 1.21 (br, 2H, -($\underline{CH_2}$-C(CH_3))-), 1.15 (d, 12H, B-O-CH($\underline{CH_3}$)$_2$), 1.01 (d, 2H, B-$(CH_2)_2$-$\underline{CH_2}$-CH_3), 0.86 (q, 4H, B-$(CH_2)_3$-$\underline{CH_3}$); ^{11}B NMR (400 MHz, D_2O): δ (ppm) = 8.2 (s, -CH_2-$\underline{B}$-$(OR)_2$).

pLBBn$_1$(OF$_3$Et)$_2$, Yield: 1.05 g (82%); ^{1}H NMR (400 MHz, D_2O): δ (ppm) = 3.95 (sp, 4H, B-O-$\underline{CH_2}CF_3$), 3.62-3.54 (dt, 4H, CO-O-$\underline{CH_2}$-$\underline{CH_2}$-O-B), 1.70 (s, 3H, CH_2-C($\underline{CH_3}$)-CH_2), 1.47 (q, 2H, B-$\underline{CH_2}$-CH_2-), 1.30 (sx, 2H, B-CH_2-$\underline{CH_2}$-CH_2), 1.24 (br, 2H, -($\underline{CH_2}$-C(CH_3))-), 1.10 (m, 2H, B-$(CH_2)_2$-$\underline{CH_2}$-CH_3), 0.85 (q, 3H, B-$(CH_2)_3$-$\underline{CH_3}$); ^{11}B NMR (400 MHz, D_2O): δ (ppm) = 8.2 (s, -CH_2-$\underline{B}$-$(OR)_2$); ^{19}F NMR (400 MHz, D_2O): δ (ppm) = -76.02 (s, CF_3).

pLBBn$_1$(OF$_6$iP)$_2$, Yield: 1.32 g (91%); ^{1}H NMR (400 MHz, D_2O): δ (ppm) = 4.63 (sp, 2H, B-O-$\underline{CH}(CF_3)_2$), 3.63-3.56 (dt, 4H, CO-O-$\underline{CH_2}$-$\underline{CH_2}$-O-B), 1.71 (s, 3H, CH_2-C($\underline{CH_3}$)-CH_2), 1.49 (q, 2H, B-$\underline{CH_2}$-CH_2-), 1.30 (sx, 2H, B-CH_2-$\underline{CH_2}$-CH_2-), 1.24 (br, 2H, -($\underline{CH_2}$-C(CH_3))-), 1.11 (c, 2H, B-$(CH_2)_2$-$\underline{CH_2}$-CH_3), 0.86 (q, 3H, B-$(CH_2)_3$-$\underline{CH_3}$); ^{11}B NMR (400 MHz, D_2O): δ (ppm) = 7.77 (s, -CH_2-$\underline{B}$-$(OR)_2$); ^{19}F NMR (400 MHz, D_2O): δ (ppm) = -75.89 (s, CF_3).

pLBBn$_1$(OAc)$_2$, Yield: 1.42 g (71%); ^{1}H NMR (400 MHz, D_2O): δ (ppm) = 3.79-3.38 (m, 12H, O-$\underline{CH_2}$-$\underline{CH_2}$-O-), 1.92 (s, 6H, CO-$\underline{CH_3}$), 1.76 (s, 3H, CH_2-C($\underline{CH_3}$)-CH_2), 1.53 (m, 2H, B-$\underline{CH_2}$-CH_2-), 1.30 (sx, 2H, B-CH_2-$\underline{CH_2}$-CH_2-), 1.29 (br, 2H, -($\underline{CH_2}$-C(CH_3))-), 1.10 (c, 2H, B-$(CH_2)_2$-$\underline{CH_2}$-CH_3), 0.90 (t, 3H, B-$(CH_2)_3$-$\underline{CH_3}$); ^{11}B NMR (400 MHz, D_2O): δ (ppm) = 8.2 (s, -CH_2-$\underline{B}$-$(OR)_2$).

pLBBn$_1$(OGly)$_2$, Yield: 3.54 g (68%); ^{1}H NMR (400 MHz, D_2O): δ (ppm) = 3.61-3.53 (m, 28H, O-$\underline{CH_2}$-$\underline{CH_2}$-O), 3.07 (s, 6H, CO-$\underline{CH_3}$), 1.65 (s, 3H, CH_2-C($\underline{CH_3}$)-CH_2), 1.43 (m, 6H, B-$\underline{CH_2}$-CH_2-), 1.25 (m, 6H, B-CH_2-$\underline{CH_2}$-CH_2-), 1.16 (br, 2H, -($\underline{CH_2}$-C(CH_3))-), 1.06 (m, 2H, B-$(CH_2)_2$-$\underline{CH_2}$-CH_3), 0.81 (m, 9H, B-$(CH_2)_3$-$\underline{CH_3}$); ^{11}B NMR (400 MHz, D_2O): δ (ppm) = 8.2 (s, -CH_2-$\underline{B}$-$(OR)_2$).

pLBBn$_1$(OGlyOF$_6$iP), Yield: 2.16 g (91%); ^{1}H NMR (400 MHz, D_2O): δ (ppm) = 4.47 (sp, 1H, B-O-CH(CF_3)$_2$), 3.62-3.46 (m, 16H, O-CH_2-CH_2-O), 3.40 (s, 3H, -O-CH_3), 1.62 (s, 3H, CH_2-C(CH_3)), 1.41 (m, B-CH_2-CH_2-), 1.24 (m, B-CH_2-CH_2-CH_2-), 1.07 (m, B-(CH_2)$_2$-CH_2-CH_3), 1.02 (br, -(CH_2-C(CH_3))-), 0.79 (m, B-(CH_2)$_3$-CH_3); ^{11}B NMR (400 MHz, D_2O): δ (ppm) = 8.2 (s, -CH_2-B-(OR)$_2$); ^{19}F NMR (400 MHz, D_2O): δ (ppm) = -78.2 (s, CF_3).

pLBBn$_7$(OGlyOF$_3$iP), Yield: 2.97 g (78%); ^{1}H NMR (400 MHz, D_2O): δ (ppm) = 4.51 (sp, 1H, B-O-CH(CF_3)(CH_3)), 3.54-3.63 (m, 28H, O-(CH_2-CH_2)$_7$-O), 3.49 (s, 3H, -O-CH_3), 1.71 (s, 3H, CH_2-C(CH_3)), 1.49 (m, B-CH_2-CH_2-), 1.30 (m, B-CH_2-CH_2-CH_2-), 1.15 (d, 12H, B-O-CH(CF_3)(CH_3)), 1.10 (m, B-(CH_2)$_2$-CH_2-CH_3), 1.01 (br, -(CH_2-C(CH_3))-), 0.86 (m, B-(CH_2)$_3$-CH_3); ^{11}B NMR (400 MHz, D_2O): δ (ppm) = 8.2 (s, -CH_2-B-(OR)$_2$); ^{19}F NMR (400 MHz, D_2O): δ (ppm) = -78.2 (s, CF_3).

pLBBn$_7$(OMe)$_2$, Yield: 0.9 g (89%); ^{1}H NMR (400 MHz, D2O): δ (ppm) = 3.59 (dt, 28H, CO-O-(CH_2-CH_2)$_7$-O-B), 2.54 (sx, 6H, B-O-CH_3), 1.70 (s, 3H, CH_2-C(CH_3)-CH_2), 1.47 (q, 2H, B-CH_2-CH_2-), 1.30 (q, 2H, B-CH_2-CH_2-CH_2-), 1.20 (br, 2H, -(CH_2-C(CH_3))-), 1.01 (m, 2H, B-(CH_2)$_2$-CH_2-CH_3), 0.83 (q, 3H, (CH_2)$_2$-CH_3); ^{11}B NMR (400 MHz, D_2O): δ (ppm) = 8.2 (s, -CH_2-B-(OR)$_2$).

pLBBn$_7$(OEt)$_2$, Yield: 4.1 g (77%); ^{1}H NMR (400 MHz, D_2O): δ (ppm) = 3.61-3.58 (dt, 28H, CO-O-(CH_2-CH_2)$_7$-O-B), 2.81 (q, 4H, B-O-CH_2), 1.69 (s, 3H, CH_2-C(CH_3)-CH_2), 1.47 (q, 2H, B-CH_2-CH_2-), 1.29 (q, 2H, B-CH_2-CH_2-CH_2-), 1.19 (br, 2H, -(CH_2-C(CH_3))-), 1.13 (t, 6H, B-O-CH_2-CH_3), 1.01 (m, 2H, B-(CH_2)$_2$-CH_2-CH_3), 0.85 (q, 6H, (CH_2)$_3$-

$\underline{CH_3}$); ^{11}B NMR (400 MHz, D_2O): δ (ppm) = 8.2 (s, -CH_2-$\underline{B}$-$(OR)_2$).

pLBBn$_7$(OiP)$_2$, Yield: 2.1 g (95%); ^{1}H NMR (400 MHz, D_2O): δ (ppm) = 3.98 (m, 2H, B-O-$\underline{CH}(CH_3)_2$), 3.63-3.49 (dt, 28H, CO-O-($\underline{CH_2}$-$\underline{CH_2}$)$_7$-O-B), 1.71 (s, 3H, CH_2-C($\underline{CH_3}$)-CH_2), 1.49 (q, 2H, B-$\underline{CH_2}$-CH_2-), 1.32 (q, 2H, B-CH_2-$\underline{CH_2}$-CH_2-), 1.23 (br, 2H, -($\underline{CH_2}$-C(CH_3))-), 1.14-1.12 (d, 12H, B-O-CH($\underline{CH_3}$)$_2$), 1.01 (m, 2H, B-$(CH_2)_2$-$\underline{CH_2}$-CH_3), 0.86 (q, 3H, $(CH_2)_3$-$\underline{CH_3}$); ^{11}B NMR (400 MHz, D_2O): δ (ppm) = 8.2 (s, -CH_2-$\underline{B}$-$(OR)_2$).

pLBBn$_9$(OMe)$_2$, Yield: 1.9 g (63%); 1H NMR (400 MHz, D2O): δ (ppm) = 3.70-3.60 (dt, CO-O-($\underline{CH_2}$-$\underline{CH_2}$)$_9$-O-B), 2.54 (s, 6H, B-O-$\underline{CH_3}$), 1.71 (s, 3H, CH_2-C($\underline{CH_3}$)-CH_2), 1.48 (q, 2H, B-$\underline{CH_2}$-CH_2-), 1.30 (q, 2H, B-CH_2-$\underline{CH_2}$-CH_2-), 1.22 (br, 2H, -($\underline{CH_2}$-C(CH_3))-), 1.01 (q, 2H, B-$(CH_2)_2$-$\underline{CH_2}$-CH_3), 0.82 (t, 3H, $(CH_2)_3$-$\underline{CH_3}$); ^{11}B NMR (400 MHz, D_2O): δ (ppm) = 8.2 (s, -CH_2-$\underline{B}$-$(OR)_2$).

pLBBn$_7$(OF$_3$iP)$_2$, Yield: 2.7 g (68%); ^{1}H NMR (400 MHz, D_2O): δ (ppm) = 4.51-4.19 (m, 2H, B-O-$\underline{CH}(CF_3)(CH_3)$), 3.70-3.55 (dt, 28H, CO-O-($\underline{CH_2}$-$\underline{CH_2}$)$_7$-O-B), 1.71 (s, 3H, CH_2-C($\underline{CH_3}$)-CH_2), 1.49 (q, 2H, B-$\underline{CH_2}$-CH_2-), 1.30 (sx, 2H, B-CH_2-$\underline{CH_2}$-CH_2-), 1.26 (br, 2H, -($\underline{CH_2}$-C(CH_3))-), 1.12 (m, 2H, B-$(CH_2)_2$-$\underline{CH_2}$-CH_3), 1.02 (d, 6H, B-O-CH(CF_3)($\underline{CH_3}$)), 0.86 (q, 3H, $(CH_2)_3$-$\underline{CH_3}$); ^{11}B NMR (400 MHz, D_2O): δ (ppm) = 8.2 (s, -CH_2-$\underline{B}$-$(OR)_2$); ^{19}F NMR (400 MHz, D_2O): δ (ppm) = -75.98 (s, CF_3).

pLBBn$_7$(OF$_6$iP)$_2$, Yield: 6.6 g (92%); ^{1}H NMR (400 MHz, D_2O): δ (ppm) = 4.67 (m, 2H, B-O-$\underline{CH}(CF_3)_2$), 3.70-3.55 (dt, 28H, CO-O-($\underline{CH_2}$-$\underline{CH_2}$)$_7$-O-B), 1.71 (s, 3H, CH_2-C($\underline{CH_3}$)-CH_2), 1.48 (q, 2H, B-$\underline{CH_2}$-CH_2-), 1.30 (sx, 2H, B-CH_2-$\underline{CH_2}$-CH_2-), 1.26 (br, 2H, -($\underline{CH_2}$-C(CH_3))-), 1.12 (m, 2H, B-$(CH_2)_2$-$\underline{CH_2}$-CH_3), 0.86 (q, 3H, $(CH_2)_2$-$\underline{CH_3}$); ^{11}B NMR (400

MHz, D_2O): δ (ppm) = 8.2 (s, -CH_2-B-$(OR)_2$); ^{19}F NMR (400 MHz, D_2O): δ (ppm) = -75.89 (s, CF_3).

The thermal properties of the polymers were evaluated by TGA (SDTQ-600 TA instruments) with a heating rate of 10 °C.min^{-1} from 30 to 650 °C under an N_2 atmosphere to measure the T_d, and by DSC (SDTQ-600 TA instruments) with a heating rate of 10 °C.min^{-1} from -70 to 100 °C under N_2 flow. The glass transition temperatures (T_g) were measured by the onset-temperature extrapolated in the second heating scan.

3.6.5. Preparation of SLICPEs

The SLICPEs made with the white solid polymers such as pLBBn$_1$(OMe)$_2$, pLBBn$_1$(OEt)$_2$, pLBBn$_1$(OiP)$_2$, pLBBn$_1$(OF$_3$Et)$_2$, and pLBBn$_1$(OF$_6$iP)$_2$ were prepared by dissolution, drop-casting and evaporation. A solution of 10 wt.% of polymer in MeOH was mixed and 200 µL was drop-casted onto an 11 mm diameter silicone mold. First, the SLICPEs were dried at RT under nitrogen flow for 6h, and then under vacuum in BUCHI glass oven at 60 °C for 2h.

The viscous liquid polymers such as pLBBn$_7$(OF$_6$iP)$_2$, pLBBn$_1$(OGlyOF$_6$iP), and pLBBn$_1$(OAc)$_2$ were used as is, without the need for any particular physical preparation for tests.

The SLICPEs made with the gel polymers such as pLBBn$_1$(OGly)$_2$, pLBBn$_7$(OMe)$_2$, pLBBn$_7$(OEt)$_2$, pLBBn$_7$(OiP)$_2$, pLBBn$_7$(OF$_3$iP)$_2$, and pLBBn$_9$(OMe)$_2$ were prepared with a hot press at 60 °C under 10 bars for 5 min. The thickness of the obtained membranes for the gel polymers were around 100 µm.

For the tests of gel SLICPEs in contact with lithium metal, the polymers were used in an Ar–filled glove box. In the first step, the polymers were placed inside sealed airtight pockets inside the glove box in order to be pressed at 60 °C under 10 bars for 5 min avoiding moisture environment contact. In a second step, the lithium metal was placed on the made SLICPE membrane and closed together inside sealed airtight pocket to be pressed following the same condition that previously.

3.6.6. Electrochemical characterizations

Ionic conductivity of SLICPEs was measured on three different samples by EIS using an Autolab 302N potentiostat/galvanostat (Metrohm AG) equipped with a temperature controller (Microcell HC station). The samples were placed between two stainless steel electrodes with a surface area of 0.5 cm^2 and a thickness of 0.1 mm. The measurements were carried out every 10 °C between 95 and 25 °C with a frequency range set from 0.1 MHz to 0.1 Hz and 10 mV amplitude. The ionic conductivity of SLICPEs were calculated following **Equation (3.1)** based on literature [27]:

$$\boldsymbol{\sigma = \frac{1}{R_b}\frac{d}{S}} \qquad \textbf{(3.1)}$$

where σ is the ionic conductivity ($S.cm^{-1}$), d is the thickness of the SLICPE (cm), S is the area (cm^2) of electrodes in contact with the SLICPE, R_b is the bulk resistance extracted from the Nyquist plot obtained in EIS.

The activation energy E_a of SLICPEs was calculated according to Arrhenius **Equation (3.2)** based on literature [28]:

$$\boldsymbol{\sigma = \sigma_0 \,.\, \exp\left(\frac{-E_a}{RT}\right)} \qquad \textbf{(3.2)}$$

where σ_0 is the exponential pre-factor related to the conductivity at infinite temperature, E_a is the activation energy for ion mobility, R is the universal gas constant (8.314 J.mol^{-1}.K^{-1}), and T is the absolute temperature.

The lithium-ion transference numbers ($\boldsymbol{t_{Li^+}}$) were evaluated in Li | SLICPE | Li symmetric coin cells employing the direct current (DC) polarization/alternating current (AC) impedance method. A potential of 10 mV (ΔV) was applied to polarize the SLICPEs during a chronoamperometry. $\boldsymbol{t_{Li^+}}$ were calculated following the **Equation (3.3)** proposed by Evans-Vincent-Bruce Method [29]:

$$\boldsymbol{t_{Li^+} = \frac{I_{ss}(\Delta V - I_0 R_0)}{I_0(\Delta V - I_{ss} R_{ss})}} \quad \textbf{(3.3)}$$

where I_{ss} is the steady-state current for the sample polarized, I_0 is the initial value of the current upon polarization, R_{ss} and R_0 are the electrode resistances obtained by EIS after and before the polarization respectively.

The electrochemical stability windows were evaluated with a Stainless-steel | SLICPE | Li coin cell using linear sweep voltammetry (LSV) in a range from 2 to 6 V vs Li^+/Li at a scan rate of 0.2 mV.s^{-1} at 25 °C.

A full cell was assembled with the SLICPE pLBBn$_7$(OF$_6$iP)$_2$ as solid polymer electrolyte (SPE), lithium iron phosphate electrode ($LiFePO_4$ or LFP) as cathode (1 mA.h/cm^2), and lithium titanate electrode ($Li_4Ti_5O_{12}$ or LTO) as an anode (150 mA.h/g) in CR 2032 coin cell. The viscous homopolymer was fixed inside a Teflon O-ring spacer with circular samples, 0.5 cm of radius, and thickness of 850 µm. The cell was tested through galvanostatic discharge–charge (GDC) cycling between a voltage range of 1.0 and 2.5 V using a Multi Potentiostat MPG2-6 and VMP3-1 (Bio-Logic). The temperature

was maintained at 60 °C with a thermostatic chamber during the tests. Impedance measurements were performed at 2.0V under open-circuit conditions by applying a voltage of 10 mV amplitude sine wave in the frequency range setting from 1.0 MHz to 30 mHz at different temperatures (40, 50, 60, 70, and 80 °C).

3.7. References

(1) Oh, K. S.; Kim, J. H.; Kim, S. H.; Oh, D.; Han, S. P.; Jung, K.; Wang, Z.; Shi, L.; Su, Y.; Yim, T.; Yuan, S.; Lee, S. Y. Single-Ion Conducting Soft Electrolytes for Semi-Solid Lithium Metal Batteries Enabling Cell Fabrication and Operation under Ambient Conditions. *Adv. Energy Mater.* **2021**, *11* (38), 1–11.

(2) Zhou, D.; Tkacheva, A.; Tang, X.; Sun, B.; Shanmukaraj, D.; Li, P.; Zhang, F.; Armand, M.; Wang, G. Stable Conversion Chemistry-Based Lithium Metal Batteries Enabled by Hierarchical Multifunctional Polymer Electrolytes with Near-Single Ion Conduction. *Angew. Chemie - Int. Ed.* **2019**, *58* (18), 6001–6006.

(3) Khan, I.; Fish, D.; Delaviz, Y.; Smid, J. ABA Triblock Comb Copolymers with Oligo(Oxyethylene) Side Chains as Matrix for Ion Transport. *Die Makromol. Chemie* **1989**, *190* (5), 1069–1078.

(4) Strauss, E.; Menkin, S.; Golodnitsky, D. On the Way to High-Conductivity Single Lithium-Ion Conductors. *J. Solid State Electrochem.* **2017**, *21* (7), 1879–1905.

(5) Zhou, D.; Shanmukaraj, D.; Tkacheva, A.; Armand, M.; Wang, G. Polymer Electrolytes for Lithium-Based Batteries: Advances and Prospects. *Chem* **2019**, *5* (9), 2326–2352.

(6) Mindemark, J.; Lacey, M. J.; Bowden, T.; Brandell, D. Beyond PEO—Alternative Host Materials for Li+-Conducting Solid Polymer Electrolytes. *Prog. Polym. Sci.* **2018**, *81*, 114–143.

(7) Porcarelli, L.; Vlasov, P. S.; Ponkratov, D. O.; Lozinskaya, E. I.; Antonov, D. Y.; Nair, J. R.; Gerbaldi, C.; Mecerreyes, D.; Shaplov, A. S. Design of Ionic Liquid like Monomers towards Easy-Accessible Single-Ion Conducting Polymer

Electrolytes. *Eur. Polym. J.* **2018**, *107* (August), 218–228.

(8) Zhu, Y. S.; Wang, X. J.; Hou, Y. Y.; Gao, X. W.; Liu, L. L.; Wu, Y. P.; Shimizu, M. A New Single-Ion Polymer Electrolyte Based on Polyvinyl Alcohol for Lithium Ion Batteries. *Electrochim. Acta* **2013**, *87*, 113–118.

(9) Dai, K.; Zheng, Y.; Wei, W. Organoboron-Containing Polymer Electrolytes for High-Performance Lithium Batteries. *Adv. Funct. Mater.* **2021**, *31* (13), 1–20.

(10) Zhang, H.; Li, C.; Piszcz, M.; Coya, E.; Rojo, T.; Rodriguez-Martinez, L. M.; Armand, M.; Zhou, Z. Single Lithium-Ion Conducting Solid Polymer Electrolytes: Advances and Perspectives. *Chem. Soc. Rev.* **2017**, *46* (3), 797–815.

(11) Porcarelli, L.; Shaplov, A. S.; Salsamendi, M.; Nair, J. R.; Vygodskii, Y. S.; Mecerreyes, D.; Gerbaldi, C. Single-Ion Block Copoly(Ionic Liquid)s as Electrolytes for All-Solid State Lithium Batteries. *ACS Appl. Mater. Interfaces* **2016**, *8* (16), 10350–10359.

(12) Shaplov, A. S.; Vlasov, P. S.; Armand, M.; Lozinskaya, E. I.; Ponkratov, D. O.; Malyshkina, I. A.; Vidal, F.; Okatova, O. V.; Pavlov, G. M.; Wandrey, C.; Godovikov, I. A.; Vygodskii, Y. S. Design and Synthesis of New Anionic "Polymeric Ionic Liquids" with High Charge Delocalization. *Polym. Chem.* **2011**, *2* (11), 2609–2618.

(13) Meziane, R.; Bonnet, J. P.; Courty, M.; Djellab, K.; Armand, M. Single-Ion Polymer Electrolytes Based on a Delocalized Polyanion for Lithium Batteries. *Electrochim. Acta* **2011**, *57* (1), 14–19.

(14) Ma, Q.; Zhang, H.; Zhou, C.; Zheng, L.; Cheng, P.; Nie, J.; Feng, W.; Hu, Y. S.; Li, H.; Huang, X.; Chen, L.; Armand, M.; Zhou, Z. Single Lithium-Ion Conducting

Polymer Electrolytes Based on a Super-Delocalized Polyanion. *Angew. Chemie - Int. Ed.* **2016**, *55* (7), 2521–2525.

(15) Lingua, G.; Grysan, P.; Vlasov, P. S.; Verge, P.; Shaplov, A. S.; Gerbaldi, C. Unique Carbonate-Based Single Ion Conducting Block Copolymers Enabling High-Voltage, All-Solid-State Lithium Metal Batteries. *Macromolecules* **2021**, *54* (14), 6911–6924.

(16) Kang, W. C.; Park, H. G.; Kim, K. C.; Ryu, S. W. Synthesis and Electrochemical Properties of Lithium Methacrylate-Based Self-Doped Gel Polymer Electrolytes. *Electrochim. Acta* **2009**, *54* (19), 4540–4544.

(17) Bouchet, R.; Maria, S.; Meziane, R.; Aboulaich, A.; Lienafa, L.; Bonnet, J. P.; Phan, T. N. T.; Bertin, D.; Gigmes, D.; Devaux, D.; Denoyel, R.; Armand, M. Single-Ion BAB Triblock Copolymers as Highly Efficient Electrolytes for Lithium-Metal Batteries. *Nat. Mater.* **2013**, *12* (5), 452–457.

(18) Villaluenga, I.; Inceoglu, S.; Jiang, X.; Chen, X. C.; Chintapalli, M.; Wang, D. R.; Devaux, D.; Balsara, N. P. Nanostructured Single-Ion-Conducting Hybrid Electrolytes Based on Salty Nanoparticles and Block Copolymers. *Macromolecules* **2017**, *50* (5), 1998–2005.

(19) Yuan, H.; Luan, J.; Yang, Z.; Zhang, J.; Wu, Y.; Lu, Z.; Liu, H. Single Lithium-Ion Conducting Solid Polymer Electrolyte with Superior Electrochemical Stability and Interfacial Compatibility for Solid-State Lithium Metal Batteries. *ACS Appl. Mater. Interfaces* **2020**, *12* (6), 7249–7256.

(20) Cakmak, G.; Verhoeven, A.; Jansen, M. Synthesis and Characterization of Solid Single Ion Conductors Based on Poly[Lithium Tetrakis(Ethyleneboryl)Borate]. *J. Mater. Chem.* **2009**, *19* (25), 4310–4318.

(21) Sun, Y.; Li, G.; Lai, Y.; Zeng, D.; Cheng, H. High Rate Lithium-Sulfur Battery Enabled by Sandwiched Single Ion Conducting Polymer Electrolyte. *Nat. Publ. Gr.* **2016**, No. September 2015, 1–9.

(22) Guzmán-González, G.; Ramos-Sánchez, G.; Camacho-Forero, L. E.; González, I. Charge Delocalization on BO 4- Centers to Improve Conductivity on Single Lithium Ion Conducting Polymer Electrolytes: A Computational/Experimental Approach. *J. Phys. Chem. C* **2019**, *123* (29), 17686–17694.

(23) Hamaide, T.; Le Deore, C. Cationic Conductivity and Relaxation Processes in Solid Polymer Electrolytes with Lithium Perfluoroalkyl Sulfonate or Sulfonato End-Capped Poly(Ethylene Oxide). *Polymer (Guildf).* **1993**, *34* (5), 1038–1046.

(24) Niitani, T.; Shimada, M.; Kawamura, K.; Dokko, K.; Rho, Y. H.; Kanamura, K. Synthesis of Li+ Ion Conductive PEO-PSt Block Copolymer Electrolyte with Microphase Separation Structure. *Electrochem. Solid-State Lett.* **2005**, *8* (8), 385–388.

(25) Nava, D. P.; Guzmán, G.; Vazquez-Arenas, J.; Cardoso, J.; Gomez, B.; Gonzalez, I. An Experimental and Theoretical Correlation to Account for the Effect of LiPF6 Concentration on the Ionic Conductivity of Poly(Poly (Ethylene Glycol) Methacrylate). *Solid State Ionics* **2016**, *290*, 98–107.

(26) Zhu, J.; Zhang, Z.; Zhao, S.; Westover, A. S.; Belharouak, I.; Cao, P. F. Single-Ion Conducting Polymer Electrolytes for Solid-State Lithium–Metal Batteries: Design, Performance, and Challenges. *Adv. Energy Mater.* **2021**, *11* (14), 1–18.

(27) Qian, X.; Gu, N.; Cheng, Z.; Yang, X.; Wang, E.; Dong, S. Methods to Study the Ionic Conductivity of Polymeric Electrolytes Using a.c. Impedance Spectroscopy. *J. Solid State Electrochem.* **2001**, *6* (1), 8–15.

(28) Menzinger, M.; Wolfgang, R. The Meaning and Use of the Arrhenius Activation Energy. *Angew. Chemie Int. Ed. English* **1969**, *8* (6), 438–444.

(29) Zugmann, S.; Fleischmann, M.; Amereller, M.; Gschwind, R. M.; Wiemhöfer, H. D.; Gores, H. J. Measurement of Transference Numbers for Lithium Ion Electrolytes via Four Different Methods, a Comparative Study. *Electrochim. Acta* **2011**, *56* (11), 3926–3933.

Chapter 4. Conclusion

This doctoral thesis was focused on the development of innovative polymers for the electrochemical energy storage systems such as lithium batteries. The first chapter introduced the overall context of the importance of the development and optimization of batteries, in particular for automotive applications. The batteries that have marked the history were presented, as well as the operating principle of a battery. Some examples from the literature of the needs of polymeric binders for cathodes and solid polymer electrolytes were presented as well as the general goal of the thesis.

In the second chapter, the objective was to improve the performance of the battery by developing new polymer binders, which could have a beneficial effect on the capacity or cyclability of the battery. The strategy developed in this chapter was the replacement of conventional PVDF binder with a functional polymer that can improve the Li-ion kinetics and transport. Two families of PDADMA-based poly(ionic liquid)s with different kinds of counter anions were synthesized to be used as cathode binders in Li-ion batteries. The first family contained four PILs with highly delocalized charge density in the counter anions by various fluorine moieties, and the second family contained four PILs with polyphenols as the counter anions. The chemical structure, thermal stability, and solubility of the polymers were evaluated and confirmed their good conditions for application as battery binders. The results demonstrated that PDADMA PILs with

fluorinated anions of the first family were highly competitive alternatives to PVDF for Li-ion battery cathodes. Indeed, the internal cell resistance decreased by 20-40%, the capacity increased by 9% at 0.3 C and 26% at 5C (for PDADMA-CFSO), and the cycling stability of the cells in accelerating aging conditions was also improved with PDADMA PILs with fluorinated anions used as binders when compared to the PVDF-containing cell. Concerning the second family of polymers, studies on electrochemical properties showed interesting reversible redox behavior for the PDADMA PILs with catechol groups (PDADMA-3,4DHB and PDADMA-2,5DHB) due to the benzoquinone redox reaction. However, the application as binders of the PDADMA PILs with catechol groups did not improve the performances of NMC cells showing decreased capacities and increased resistances compared to PVDF binders. PDADMA PILs with polyphenols showed difficulties to be dissolved in solvents and to make uniform and homogeneous electrodes. Moreover, the low performance could be related to a mismatch of redox potentials between NMC and benzoquinone redox reactions.

In conclusion, of the second chapter, the PDADMA PILs with fluorinated anions (the first family) used as binders were very promising to improve the capacity and resistance in Li-ion batteries, especially the PDADMA-CFSO that showed the best results. On the other hand, PDADMA PILs with polyphenol groups (the second family) showed interesting redox activities. However, the results in Li-ion batteries did not show any improvement in performance when used as binders, but these are materials that deserve further investigation as redox polymers, as in organic batteries for example.

The second objectives of the PhD thesis was develop an innovative family of single lithium-ion conducting polymer electrolytes (SLICPEs) based on highly delocalized

borate groups. Different polymer derivatives were synthesized and classified according to their chemical characteristics of substituents such as aliphatic, fluorinated, self-solvating, and both fluorinated and ethylene glycol substituents combined. Synthesis and characterizations were reported, and thermal analysis showed good properties for battery application below 80 ºC. The effect of different substituents on ionic conductivity by changing the size and electron-withdrawing groups were studied and explained. The highest ionic conductivities measured were 1.65×10^{-4} and 1.29×10^{-4} $S.cm^{-1}$ at 60 °C for $pLBBn_1(OGlyOF_6iP)$ and $pLBBn_7(OF_6iP)_2$ respectively. It is worth mentioning that these are the highest ionic conductivities reported for a single conductive lithium-ion homopolymer to the best of our knowledge. The lithium transference numbers were measured between 0.88 and 0.93 and confirmed the single ion-conducting properties. The SLICPE $pLBBn_1(OGlyOF_6iP)$ was tested in battery LTO || LFP at 60 ºC and 238 µA.h of capacity was measured during the first charge at 0.04C and 1.7 kΩ of resistance. The results were encouraging and concluded as a proof of concept for the use of the SLIPCE polymer as a solid electrolyte. However, the performance of the full solid state battery was quite low due to the absence of electrolytes in the anode and cathode. There are many possibilities for future work with this project, such as optimizing the battery configuration or including this monomer in co-polymer or polymer electrolyte formulations thanks to the versatility of the acrylic polymer chemistry.

Resumen

A lo largo de la historia, el ser humano ha desarrollado métodos para la conversión y almacenamiento de energía. Hoy en día, no solo nuestra sociedad depende de ella a diario, sino que la demanda energética va aumentando exponencialmente. Paralelamente al crecimiento de la demanda energética, existe el problema del cambio climático debido en parte a las emisiones de CO_2 derivadas de la actividad humana. La Agencia Europea de Medio Ambiente (AEMA) reveló que, en 2019, el 31% del consumo energético fue destinado a los medios de transporte. Asimismo, entre la energía utilizada para el transporte, en torno al 72% corresponde al transporte por carretera (pasajeros y mercancías). Es por esto que el desafío de desarrollar un almacenamiento de energía eficiente, es fundamental para apoyar la transición de los combustibles fósiles a las energías sostenibles.

En esta tesis se han investigado dos líneas de investigación, divididas en dos capítulos, con el fin de desarrollar polímeros para baterías de litio. La primera línea de investigación se centra en el aglutinante (“binder” in ingles) catódico. El aglutinante es un polímero capaz de unir el material activo con el aditivo conductor en el colector de corriente. La segunda área de investigación se refiere al desarrollo de electrolitos poliméricos sólidos. Estos tienen la ventaja de ser más seguros en comparación con los electrolitos líquidos frente al riesgo de fugas de disolventes tóxicos e inflamables.

En una primera parte, se sintetizaron y caracterizaron poli(líquidos iónicos) (PILs por sus siglas en ingles) para probarlos como aglutinantes en el cátodo como reemplazo del PVDF comúnmente utilizado en baterías comerciales. Los PILs seleccionados consisten en un esqueleto de poli(dialildimetilamonio) (PDADMA) con diferentes contra-aniones que se agrupan en dos familias. Los cuatro PILs de la primera familia se muestran en la **Figura R.1.a**, están compuestos por contra-aniones con diferentes contenidos de flúor y se llaman PDADMA-FSI, PDADMA-TFSI, PDADMA-BETI, y PDADMA-CFSO. Los cuatro PILs de la segunda familia se muestran en la **Figura R.1.b**, están compuestos por contra-aniones de benzoato que tienen dos o tres grupos hidroxilo en diferentes posiciones para las propiedades de oxidación-reducción. La estructura química, la estabilidad térmica y la solubilidad de los polímeros se evaluaron mediante pruebas de RMN, FTIR, y solubilidad en disolventes de carbonato y NMP para evaluar su potencial aplicación como aglutinante de baterías. Y, por último, todos los PILs PDADMA se probaron como

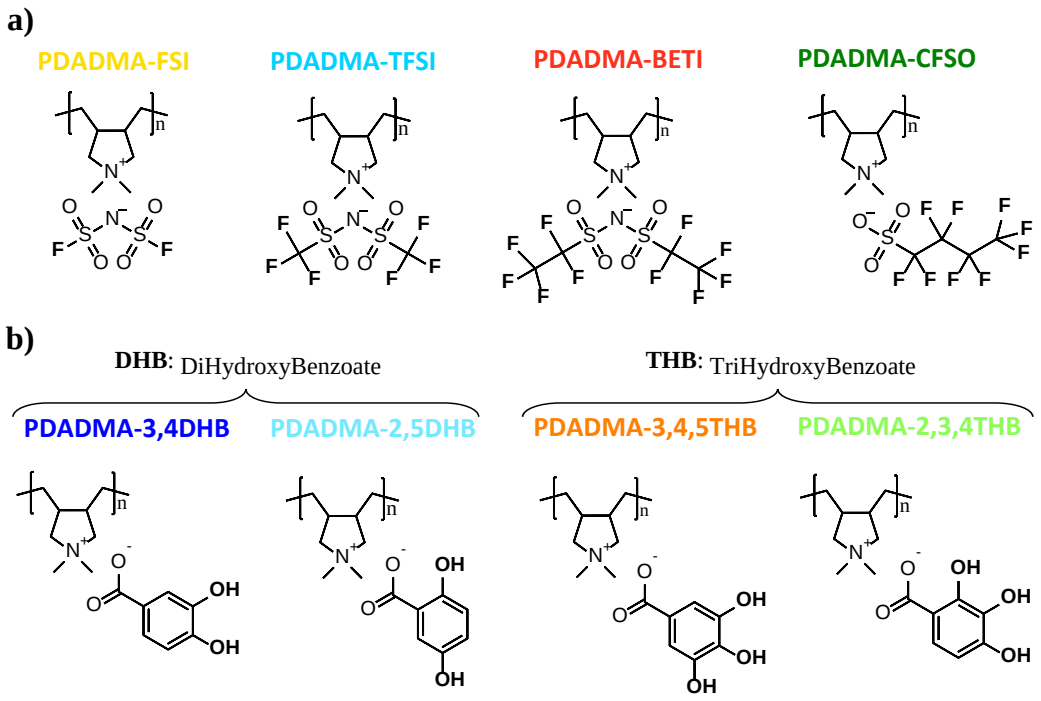

Figura R.1. PILs PDADMA a) primera familia con contra-aniones fluoradas, y b) segunda familia con contra-aniones benzoato que llevan dos o tres grupos hidroxilo.

aglutinantes en cátodos NMC para baterías de iones de litio y se compararon con el aglutinante de PVDF convencional.

Los resultados de las pruebas de la batería de litio obtenidos con las PILs fluorados (primera familia) mostraron una disminución de la resistencia interna de la celda entre un 20 y un 40%, en comparación con la celda que contenía PVDF. La carga-descarga galvanostática a diferentes corrientes mostró que las celdas PDADMA-BETI y PDADMA-CFSO obtuvieron valores de capacitancia más altos que el PVDF en todas las corrientes investigadas. Este aumento de capacidad con el aglutinante PDADMA-CFSO fue del 9% a 0,3 C y del 26% a 5 C, en comparación con el PVDF. Las pruebas de envejecimiento acelerado también mostraron la estabilidad del ciclo celular con aglutinantes basados en PDADMA fluorado. Con respecto a los PILs redox (segunda familia), las propiedades electroquímicas se estudiaron primero en electrolitos acuosos ácidos mediante voltametría cíclica. Los PILs con tres grupos hidroxilo mostraron un comportamiento redox no reversible en contraste con los PILs con dos grupos hidroxilo, que mostraron interesantes picos redox reversibles debido al par redox catecol/benzoquinona. Luego, se estudiaron los PILs con dos grupos hidroxilo en celdas de litio. Los análisis de voltamperometría cíclica mostraron un solo paso de activación para la formación de quinonas y una electroactividad reversible entre 3,0 y 3,7 V frente a Li^+/Li correspondiente a la reacción del par redox benzoquinona/catecolato de dilitio. Sin embargo, la aplicación de PILs con dos grupos hidroxilo como aglutinantes no mejoró el rendimiento de las celdas NMC, las capacidades disminuyeron y las resistencias aumentaron en comparación con los aglutinantes de PVDF. Los PILs con dos grupos hidroxilo han mostrado dificultad para ser disueltos y hacer electrodos uniformes y

homogéneos. Además, el bajo rendimiento podría estar relacionado con un desajuste de los potenciales redox entre NMC y las reacciones redox de benzoquinona.

En conclusión, los PDADMA PILs con contra-aniones fluorados (primera familia) utilizados como aglutinantes mostraron una gran promesa para mejorar la capacidad y la resistencia en las baterías de iones de litio, especialmente PDADMA-CFSO, que mostró los mejores resultados. Por otro lado, los PILs redox de PDADMA con dos grupos hidroxilo (segunda familia) mostraron actividades redox interesantes. Sin embargo, los resultados en las baterías de iones de litio no mostraron una mejora en el rendimiento cuando se usaron como aglutinantes, pero estos son materiales que vale la pena investigar más a fondo como polímeros redox, como una aplicación en baterías orgánicas, por ejemplo.

En la siguiente parte de la tesis, se propuso una nueva familia innovadora de electrolitos poliméricos conductores de iones de litio (SLICPEs por sus siglas en inglés) basados en grupos borato con densidad electrónica altamente deslocalizada. La estructura se presenta en la **Figura R.2**. Se sintetizaron y clasificaron diferentes derivados poliméricos de acuerdo con sus características químicas de sustituyentes como alifáticos, fluorados, autosolvatantes, y fluorados y etilenglicol combinados. Se reporta la síntesis y caracterizaciones, y el análisis térmico mostró buenas propiedades para la aplicación de baterías por debajo de 88 ºC. Se estudió y explicó el efecto de diferentes sustituyentes sobre la conductividad iónica al cambiar el tamaño y los grupos atractores de electrones. Las conductividades iónicas más altas medidas fueron 1.65×10^{-4} y 1.29×10^{-4} $S.cm^{-1}$ a 60 °C para $pLBBn_1(OGlyOF_6iP)$ y $pLBBn_7(OF_6iP)_2$ respectivamente. Vale la pena mencionar que estas son las conductividades iónicas más altas reportadas para un solo

homopolímero de iones de litio conductor, según nuestro conocimiento. Los números de transferencia de litio se midieron entre 0,88 y 0,93 y confirmaron las propiedades de conducción de iones individuales.

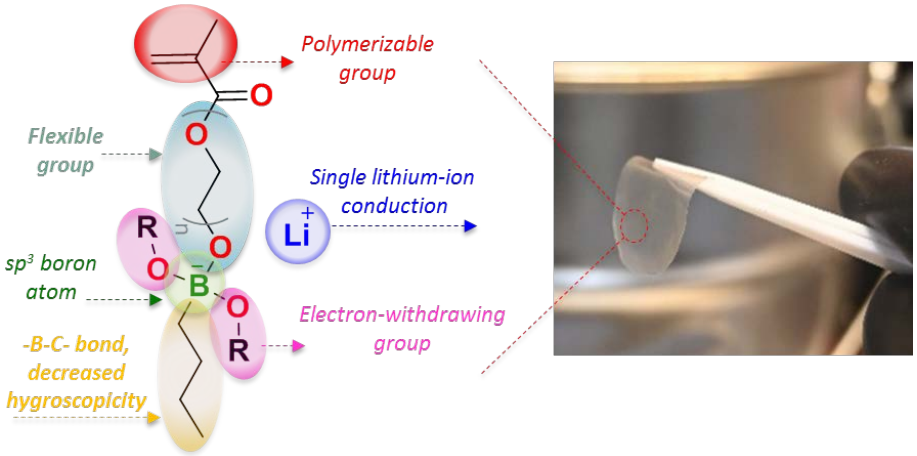

Figura R.2. Estrategia de diseño para los monómeros de borato de litio e imagen de una membrana electrolítica de homopolímero.

El SLICPE pLBBn$_1$(OGlyOF$_6$iP) fue probado en batería LTO || LFP a 60 ºC y 238 µA.h de capacidad se midió durante la primera carga a 0.04C y 1.7 kΩ de resistencia. Los resultados de la prueba de la batería fueron alentadores y concluyeron como una prueba de concepto para el uso del polímero como electrolito sólido. El rendimiento de la batería era bastante bajo debido a la ausencia de electrolitos en el ánodo y el cátodo. Hay muchas posibilidades de trabajo futuro con este proyecto, como optimizar la configuración de la batería o incluir este monómero en formulaciones de copolímero o electrolito polimérico gracias a la versatilidad de la química del polímero acrílico.

List of acronyms

2,3,4THB	2,3,4-Trihydroxybenzoic acid
2,5DHB	2,5-Dihydroxybenzoic acid
3,4DHB	3,4-Dihydroxybenzoic acid
3,4,5THB	3,4,5-Trihydroxybenzoic acid or Gallic acid
τ	Time constants
AIBN	2,2´-Azobisisobutyronitrile
BETI	Bis(perfluoroethylsulfonyl)imide
BH_3	Borane
BSE	Backscattered electron
C	Capacitors
Cd	Cadmium
CE	Counter electrode
CFSO	Nonafluoro-1-butanesulfonate
CMC	Carboxymethyl cellulose
CPE	Constant Phase Element
CV	Cyclic voltammetry
DHB	Dihydroxybenzoate
DMF	Dimethylformamide
DMSO	Dimethylsulfoxyde
DRT	Distribution of relaxation times

DSC	Differential scanning calorimetry
E_a	Activation energie
EC	Ethylene Carbonate
EEC	Equivalent electrical circuit
EIS	Electrochemical Impedance Spectroscopy
EMC	Ethyl Methyl Carbonate
ESW	Electrochemical stability window
EVs	Electric vehicles
F	Faraday constant
FSI	Bis(fluorolsulfonyl)imide
FTIR	Fourier Transform Infrared
GC	Glassy carbon electrode
GDC	Galvanostatic discharge-charge
GPE	Gel polymer electrolyte
HEA	2-Hydroxyethyl Acetate
HEMA	2-hydroxyethyl methacrylate
HFiP	1,1,1,3,3,3-Hexafluoro-2-propanol
IV	Current-voltage
$KC_4F_9SO_3$	Potassium nonafluoro-1-butanesulfonate
KOH	Potassium hydroxide
LFP	$LiFePO_4$
LIB	Lithium-ion battery
LiBETI	Lithium bis(perfluoroethylsulfonyl)imide
Li-O_2	Lithium-oxygen
LiPVAOB	Lithium polyvinyl alcohol oxalate borate

Li-S	Lithium-sulfur
LiTFSI	Lithium bis(trifluoro-methylsulfonyl)imide
LTN or t_{Li^+}	Lithium transference number
LTO	$Li_4Ti_5O_{12}$
MeOH	Methanol
M_w	Molecular weight
n	Number of charge carrier
nBuLi	n-Butyl lithium
NaFSI	Sodium bis(fluorosulfonyl)imide
Ni-Cd	Nickel-cadmium
Ni-MH	Nickel-metal hydride
NMC	$LiNi_{0.33}Co_{0.33}Mn_{0.33}O_2$
NMP	N-methyl-2-pyrrolidone
NMR	Nuclear Magnetic Resonance
OCV	Open circuit voltage
P3	Poly(1-(4-vinylbenzyl)-2,3-dimethylimidazolium TFSI)
PAN	Polyacrylonitrile
PANI	Polyaniline
PDADMA	Poly(diallyldimethylammonium)
PDADMA-3,4DHB	Poly(diallyldimethylammonium)-3,4-Dihydroxybenzoate
PDADMA-2,5DHB	Poly(diallyldimethylammonium)-2,5-Dihydroxybenzoate
PDADMA-3,4,5THB	Poly(diallyldimethylammonium)-3,4,5-Dihydroxybenzoate
PDADMA-2,3,4THB	Poly(diallyldimethylammonium)-2,3,4-Dihydroxybenzoate
PDADMA-BETI	Poly(diallyldimethylammonium bis(perfluoroethylsulfonyl) imide

PDADMA-CFSO	Poly(diallyldimethylammonium nonafluoro-1-butane sulfonate
PDADMA-Cl	Poly(diallyldimethylammonium chloride)
PDADMA-DHB	Poly(diallyldimethylammonium dihydroxybenzoate)
PDADMA-FSI	Poly(diallyldimethylammonium bis(fluorolsulfonyl)imide)
PDADMA-OH	Poly(diallyldimethylammonium hydroxide)
PDADMA-TFSI	Poly(diallyldimethylammonium)bis(trifluoro-methanesulfonyl)imide
PDADMA-THB	Poly(diallyldimethylammonium trihydroxybenzoate)
PEDOT:PSS	Poly(3,4-ethylenedioxythiphene):polystyrene
PEGMA	Poly(ethylene glycol) methacrylate
PEO	Poly(ethylene oxide)
PI	Polyimide
PILs	Poly(ionic liquid)s
PLiMTFSI	Poly(lithium 1-[3-(methacryloyloxy) propylsulfonyl]-1-(trifluoromethanesulfonyl) imide)
PMMA	Polymethylmethacrylate
PSTFSI	Lithium poly(4-styrenesulfonyl(trifluoromethylsulfonyl) imide)
PVDF	Poly(vinylidene difluoride)
PVDF-HFP	Poly(vinylidene fluoride-hexafluoro propylene)
$P(4VC)_{100}$	Poly(((4-vinyl-1,2-phenylene)bis(oxy))bis(methylene)) dibenzene or Poly(4-vinyl catechol)
$P(4VC_{86}$-*stat*-$LiSS_{14})$	Poly(4-vinyl catechol-*stat*- 4-styrenesulfonic acid lithium salt)
$Q_{théo}$	Theoretical capacities
R	Resistance
RE	Reference electrode
R_{int}	Internal resistance

RT	Room temperature
S	Solubility
SEI	Solid electrolyte interphase
SEM	Scanning Electron Microscopy
SLICPE	Single lithium-ion conducting polymer electrolyte
SoC	State of Charge
SPE	Solid polymer electrolyte
$\mathbf{T_d}$	Decomposition temperatures
TEB	Triethyl borate
TEG	Triethylene glycol
TFE	2,2,2-Trifluoroethanol
TFP	1,1,1-Trifluoro-2-propanol
TFSI	Bis(trifluoromethylsulfonyl)imide
$\mathbf{T_g}$	Glass transition temperatures
TGA	Thermogravimetric analysis
THB	Trihydroxybenzoate
THF	Tetrahydrofuran
TiPB	Triisopropyl borate
TMB	Trimethyl borate
XG	Xanthan gum
Zn-MnO_2	Zinc-manganese dioxide

List of publications and patents, conference presentations, and collaborations

PUBLICATIONS AND PATENTS

(1) Cotte, S.; Guéguen, A.; Castro, L.; Vauthier, S.; Alvarez-Tirado, M.; Casado, N.; Mecerreyes, D. Composition, Lithium-ion battery and lithium-air battery. European Patent Application No. 5 21306763.0 filed on December 13, 2021.

(2) Guzmán-González, G.; Vauthier, S.; Alvarez-Tirado, M.; Cotte, S.; Castro, L.; Guéguen, A.; Casado, N.; Mecerreyes, D. Single-Ion Lithium Conducting Polymers with High Ionic Conductivity Based on Borate Pendant Groups. Angew. Chemie - Int. Ed. 2022, 61 (7). https://doi.org/10.1002/anie.202114024.

(3) Alvarez-Tirado, M.; Guzmán-González, G.; Vauthier, S.; Cotte, S.; Guéguen, A.; Castro, L.; Mecerreyes, D. Designing Boron-Based Single-Ion Gel Polymer Electrolytes for Lithium Batteries by Photopolymerization. Macromol. Chem. Phys. 2022, 223 (8). https://doi.org/10.1002/macp.202100407.

(4) Vauthier, S.; Alvarez-Tirado, M.; Guzmán-González, G.; Tomé, L.; Cotte, S.; Castro, L.; Guéguen, A.; Mecerreyes, D.; Casado, N. High-Performance

Pyrrolidinium-Based Poly (Ionic Liquid) Binders for Li-Ion and Li-Air Batteries. 2023, *27*. https://doi.org/10.1016/j.mtchem.2022.101293.

CONFERENCE PRESENTATIONS

(1) POLYTE-EID Innovative polymers for lithium battery technologies. **S. Vauthier,** M. Alvarez, M. Lechartier, winter school ENGINE2019, Grenoble, France (poster presentation).

(2) Redox-active catechol containing poly(ionic liquid)s for organic batteries, **S. Vauthier**, N. Casado, D. Mecerreyes, L. Tome, Organic Battery Days, OBD 2021, Tokyo, Japan, 25th – 27th November 2021 (poster presentation).

COLLABORATIONS

This thesis is part of POLYTE-EID program, which is a European Industrial Doctorate project. This program puts together the expertise in automotive batteries of Toyota Motor Europe (TME, Industrial Battery Technology) in Brussels (Belgium) with the academic excellence in polymers of the University of the Basque Country (UPV/EHU, Academic Polymer Science) and POLYMAT research center in Donostia-San Sebastian (Spain).

This project has received funding from the European Union's Horizon 2020 research and innovation program under grant agreement ID 765828.